nature chemical biology

Article

https://doi.org/10.1038/s41589-026-02216-y

# Posttranslational modifications remodel proteome-wide ligandability

Received: 18 July 2025

Accepted: 30 March 2026

Published online: 05 May 2026

Check for updates

Weichao Li[1,5], Qijia Wei[1,2,5], Manuel Llanos[3], Clara Gathmann[1], Paolo Governa[3], Tzu-Yuan Chiu[1,2], Jacob M. Wozniak[1], Appaso M. Jadhav[1], Matthew Holcomb[3], Jacob Cravatt[1], Ashok Dongre[4], Mia L. Huang[1,2,3], Stefano Forli[3] & Christopher G. Parker[1,2]

Posttranslational modifications (PTMs) vastly expand the diversity of the human proteome, dynamically reshaping protein activity, interactions and localization in response to environmental, pharmacologic and disease-associated cues. However, their proteome-wide impact on small-molecule recognition—and, thus, druggability—remains largely unexplored. Here we present a chemical proteomic strategy to delineate how PTM states remodel protein ligandability in human cells. Using broad-spectrum photoaffinity probes, we identified more than 400 functionally diverse proteins whose ability to engage small molecules is impacted by phosphorylation or N-linked glycosylation status. Integrating binding site mapping with structural analyses reveals a diverse array of PTM-dependent pockets. Among these, we discovered that the phosphorylation status of common oncogenic KRAS mutants impacts the action of small molecules, including clinically approved inhibitors. These findings illuminate a previously underappreciated layer of proteome plasticity governed by PTMs and highlight opportunities to develop chemical probes that selectively target proteins in defined modification states.

Advances in genomic and transcriptomic technologies have transformed our ability to chart how biological systems respond to physiological, pathological and pharmacological perturbations. However, these methods capture only a portion of the complexity of cellular regulation, as a substaintial fraction of human biology is governed at the proteome level through PTMs, which dynamically modulate protein structure, function and interactions in ways not captured by genetic approaches. More than 680 PTMs have been identified in humans, ranging from the addition of simple functional groups (for example, methylation and acetylation) to large complex biomolecules (for example, complex glycans and small proteins)[1]. This diversity can generate hundreds of thousands of distinct proteoforms per cell, summing to millions across all human cell types[2]. In addition to their structural variety, PTMs are often highly dynamic, being added, removed or exchanged in response to diverse stimuli and environmental cues. When these regulatory processes go awry, they frequently drive pathological outcomes, underscoring the critical need to further understand how PTMs affect protein function and how this dysregulation can be therapeutically targeted[3].

To this end, extensive efforts have been directed toward global profiling of PTM dynamics using mass spectrometry (MS)-based proteomics[4]. Because many PTMs are substoichiometric and transient, enrichment techniques including immunoprecipitation, lectin-based capture, bioorthogonal labeling and metabolic incorporation are commonly employed to isolate modified proteins for MS identification and quantification[5–7]. Although these approaches have considerably

[1]Department of Chemistry, The Scripps Research Institute, La Jolla, CA, USA. [2]Skaggs Graduate School of Chemical and Biological Sciences, The Scripps Research Institute, La Jolla, CA, USA. [3]Department of Integrative Structural and Computational Biology, The Scripps Research Institute, La Jolla, CA, USA. [4]Research and Development, Bristol Myers Squibb Company, Princeton, NJ, USA. [5]These authors contributed equally: Weichao Li, Qijia Wei.
e-mail: cparker@scripps.edu

https://doi.org/10.1038/s41589-026-02216-y

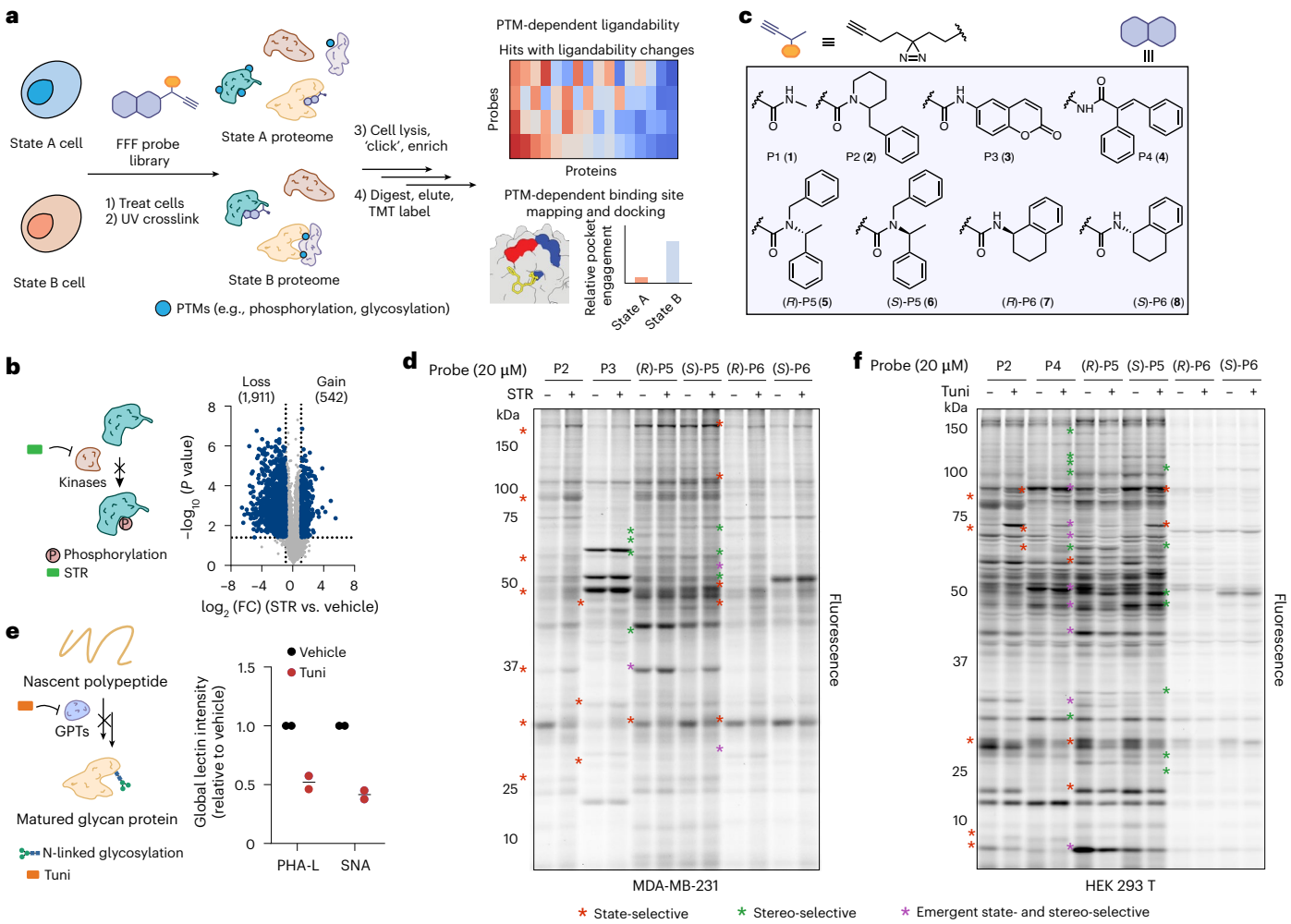



**Fig. 1 | Chemoproteomic mapping of PTM-dependent ligandability events in cells. a**, Schematic of the experimental design for identifying PTM-dependent ligandability events. **b**, Phosphorylation model system. Treatment of MDA-MB-231 cells with STR (250 nM, 3 hours) resulted in 2,453 observed phosphorylation-related changes. **c**, Structures of the FFF probe library used in this study. Each member consists of a small-molecule fragment, a diazirine photoreactive group and a clickable alkyne handle. **d**, Gel-based profiling of probe labeling under different phosphorylation states in MDA-MB-231 cells (soluble fraction). **e**, N-glycosylation model system. Treatment of HEK293T cells with Tuni (10 μg ml$^{-1}$, 24 hours) results in alterations in glycosylation as monitored with lectins PHA-L and SNA, which probe for the presence of complex-type N-linked glycans and α2,6-linked sialic acids. **f**, Gel-based profiling of N-linked glycosylation-dependent changes in HEK293T cells (soluble fraction). Red asterisks indicate representative state-selective probe–protein interactions; green asterisks denote stereo-selective enantio probe–protein interactions; and purple asterisks highlight interactions that are both state-selective and stereo-selective. Proteomic and immunoblot quantifications were derived from two independent biological replicates and are presented as mean. FC, fold change; PHA-L, *Phaseolus vulgaris* leucoagglutinin; SNA, *Sambucus nigra* agglutinin; UV, ultraviolet.

advanced knowledge of PTM prevalence and dynamics, they offer limited insight into how PTMs alter protein structure, activity or pharmacological tractability. To begin bridging this gap, powerful chemical proteomic methods, including activity-based protein profiling (ABPP), have been deployed to globally assess enzyme activity, cysteine reactivity status and covalent liganding across various biological states[8–13]. However, these approaches depend on electrophilic probes targeting nucleophilic side chains, which limit their scope to enzymes or sites with reactive residues. Moreover, observed differences are often dominated by variations in protein expression or direct modulation of side chain reactivity. Furthermore, the use of ABPP to profile proteomic states has largely been restricted to lysates[8,10], where protein interactions and compartmentalization are disrupted, potentially obscuring PTM-regulated binding events or generating artifacts due to probing of non-native conditions. To better understand how PTMs or other factors alter protein state, new strategies are needed that operate in intact systems and are agnostic to protein functional class or composition.

Among the most prevalent and functionally consequential PTMs are phosphorylation and N-linked glycosylation. Phosphorylation orchestrates signaling pathways by tuning protein activity, localization and interactions, whereas N-linked glycosylation can regulate protein folding, stability, trafficking and cell–cell recognition[14,15]. Dysregulation of these PTMs is a hallmark of diverse diseases, including cancers, autoimmune disorders and metabolic syndromes. Correspondingly, the machinery responsible for installing, removing and recognizing PTMs (for example, kinases/phosphatases, glycosyltransferases/glycosidases and acetyltransferases/deacetylases) are often drug targets[16–18]. However, pharmacological targeting of PTM-modifying enzymes often leads to pleiotropic effects, typically affecting the manifold substrates in addition to desired disease-driving pathways. An alternative strategy is to directly assess how PTMs alter the ligandability of proteins—that is, their ability to engage small molecules—across biological contexts. Such an approach could reveal disease-relevant proteoforms with differential druggability features, enabling the design of more selective therapeutic agents.

In the present study, we pursued a chemoproteomic approach that leverages broadly interactive, fragment-based photoaffinity probes to map reversible small-molecule–protein interactions as a function of phosphorylation and glycosylation status directly in cells (Fig. 1a). We uncovered hundreds of proteins, spanning diverse functional classes, that display PTM-dependent interactions with drug-like small molecules. Proteome-wide binding site mapping revealed both direct and indirect mechanisms by which PTMs reshape small-molecule accessibility. Notably, we found that phosphorylation status of KRAS impacts ligand engagement via disruption of the nucleotide exchange factor SOS1, altering binding of clinically approved inhibitors to multiple oncogenic mutants. Our findings unveil previously underappreciated layers of regulation in small-molecule–protein interactions and highlight critical implications for drug targeting.

## Results

### PTM-dependent ligandability profiling in human cells

To investigate changes in protein ligandability as a function of phosphorylation status, we aimed to broadly perturb phosphorylation while minimizing potential convoluting proteomic alterations. We found that treatment of MDA-MB-231 triple-negative breast cancer cells with staurosporine (STR), a pan-kinase inhibitor[19], at low exposures (250 nM, 3 hours), leads to broad alteration of phosphorylation levels with minimal effects on cellular viability or changes in protein abundances (Fig. 1b, Extended Data Fig. 1a–d and Supplementary Data 1). Using MS-based quantitative phosphoproteomics, we monitored more than 29,000 phosphorylation modifications on serine, tyrosine or threonine residues and identified significant (>2-fold) decreases in phosphorylation at 1,911 sites and increases at 542 sites (Fig. 1b, Extended Data Fig. 1e–h and Supplementary Data 1).

We next set out to assess the impact of phosphorylation changes on protein ligandability in cells. We chose to profile a library of eight fully functionalized fragment (FFF) probes, comprising a control probe (P1) (1); three non-chiral probes (P2) (2), P3 (3) and P4 (4); and two pairs of enantiomerically paired probes (*R*)-P5 (5) and (*S*)-P5 (6) and (*R*)-P6 (7) and (*S*)-P6 (8) (Fig. 1c). These probes were chosen for their previously reported broad proteomic interactions, utility in identifying authentic ligandable sites on proteins and demonstration that they can be progressed into selective modulators of protein function[20–24]. MDA-MB-231 cells were treated with STR or vehicle, incubated with FFF probes (20 µM) and subsequently irradiated to capture probe-bound proteins. Harvested cells were lysed, fractionated and conjugated to a rhodamine-azide tag using copper-catalyzed azide-alkyne cycloaddition (CuAAC) chemistry[25], enabling visualization of probe–protein interactions via gel-based fluorescence scanning. We observed significant alterations in probe labeling, indicative of both decreased and increased binding across numerous proteins under STR treatment (Fig. 1d and Supplementary Fig. 1a). Notably, for the enantiomerically paired probes, in addition to numerous labeling events that were stereo-selective, we also observed instances of 'emergent' stereo-selective binding events, where stereo-selectivity is apparent in one state but not the other.

To assess the impact of N-linked glycosylation on protein ligandability, we used tunicamycin (Tuni), a natural product that inhibits N-linked glycosylation through blockade of UDP-*N*-acetylglucosamine (GlcNAc) transfer to dolichol phosphate, a key step of N-linked protein glycosylation[26,27]. Using HEK293T cells, which have been extensively characterized in previous glycosylation studies[27], we screened conditions to maximize alterations in N-linked glycosylation while minimizing effects on cell viability (Fig. 1e and Extended Data Fig. 1i,j). We performed similar gel-based profiling studies with the FFF probes as described above, and, analogous to our phosphorylation perturbation, we observed numerous Tuni-dependent, stereo-selective and emergent stereo-selective probe–protein interactions across all the probes (Fig. 1f and Supplementary Fig. 1b), suggesting that these conditions would be suitable to identify glycosylation-dependent ligandability events.

Next, we sought to identify and quantify phosphorylation-dependent ligandability events through MS-based proteomics. MDA-MB-231 cells were treated with STR followed by the FFF probes (100 µM) as described above. Probe-labeled proteins were then conjugated to an azide-biotin tag, isolated and comparatively quantified by streptavidin enrichment and tandem mass tag (TMT)-based quantitative proteomics[21,22]. Proteins were considered probe targets if they exhibited >5-fold enrichment relative to control probe (P1). Probe targets that display >2-fold change ($P < 0.05$) between conditions were classified as PTM-dependent ligandability events. Among 5,056 protein targets identified across all probes, 235 (5%) exhibited altered ligandability after STR treatment with at least one probe (Extended Data Fig. 2a, Supplementary Fig. 2a and Supplementary Data 1), with 107 (46%) possessing increased probe binding and 128 (54%) possessing decreased probe binding. Similarly, we mapped N-linked glycosylation-dependent ligandability events in HEK293T cells. Using the filtering criteria established for phosphorylation, we identified a total of 4,421 probe targets, 225 of which exhibited significant ligandability changes (Extended Data Fig. 2b, Supplementary Fig. 2b and Supplementary Data 1), with 142 (63%) increased and 83 (37%) decreased in probe binding. By clustering the identified proteins based on their functional and clinical classifications[23], we found that targets exhibiting PTM dependency span a wide range of protein families (Fig. 2a,b and Supplementary Data 1). State-dependent targets were generally identified by one or two probes (Fig. 2c), and ligandability changes were largely independent of changes in protein abundance (Extended Data Fig. 2c–e), indicating molecular recognition as a major driver.

PTM-dependent targets include druggable protein classes such as enzymes and ion channels but also historically more challenging targets, including epigenetic regulators and transcription factors (Fig. 2d)[28]. Gene Ontology analysis revealed that proteins displaying PTM-dependent ligandability are enriched in cellular processes distinct from those that do not. Although non-targets (probe-enriched proteins that do not display PTM dependency) were largely associated with translation and metabolism, phosphorylation-dependent targets were enriched in pathways linked to protein localization, lysosome organization, ion homeostasis and mRNA transport, whereas saccharide metabolic processes and the ERAD pathway were prominently enriched among N-glycosylation-dependent targets (Extended Data Fig. 2f,g,i,j). Critically, PTM-dependent targets were enriched (74% in phosphorylation and 62% in N-linked glycosylation) with proteins annotated to possess the corresponding PTMs (Extended Data Fig. 2h,k), suggesting that PTM status directly impacts ligandability. Finally, PTM-dependent targets include therapeutically relevant proteins (29, classified as Tclin), such as KRAS and HMGCR, and highly liganded proteins (68, classified as Tchem); however, the vast majority (approximately 78%) were found to lack well-annotated ligands (Fig. 2e).

### Features of proteins displaying PTM-dependent ligandability

We next sought to orthogonally validate the state-dependent interactions for 10 representative targets through probe pull-down and immunoblotting. Among the STR-dependent targets, we confirmed broad reduced ligandability of the tyrosine kinase JAK1 across multiple chemotypes (P2, (*R*)-P6 and (*S*)-P6) (Fig. 3a,b). By contrast, the E1 subunit of the V-ATPase proton pump, ATP6V1E1, despite being enriched by all probes, displayed increased ligandability exclusively with (*R*/*S*)-P6, suggesting that P6 may possess a distinct binding mode that is affected by STR (Fig. 3c,d). Additional examples include the major protein kinase C substrate MARCKS (Extended Data Fig. 3a) and the transmembrane glycoprotein CD44 (Extended Data Fig. 3b), which displayed increased and decreased ligandability with P2, respectively, as well as the E3 ubiquitin-protein ligase WWP2, which exhibited decreased binding ability with (*R*/*S*)-P6 after STR treatment

https://doi.org/10.1038/s41589-026-02216-y

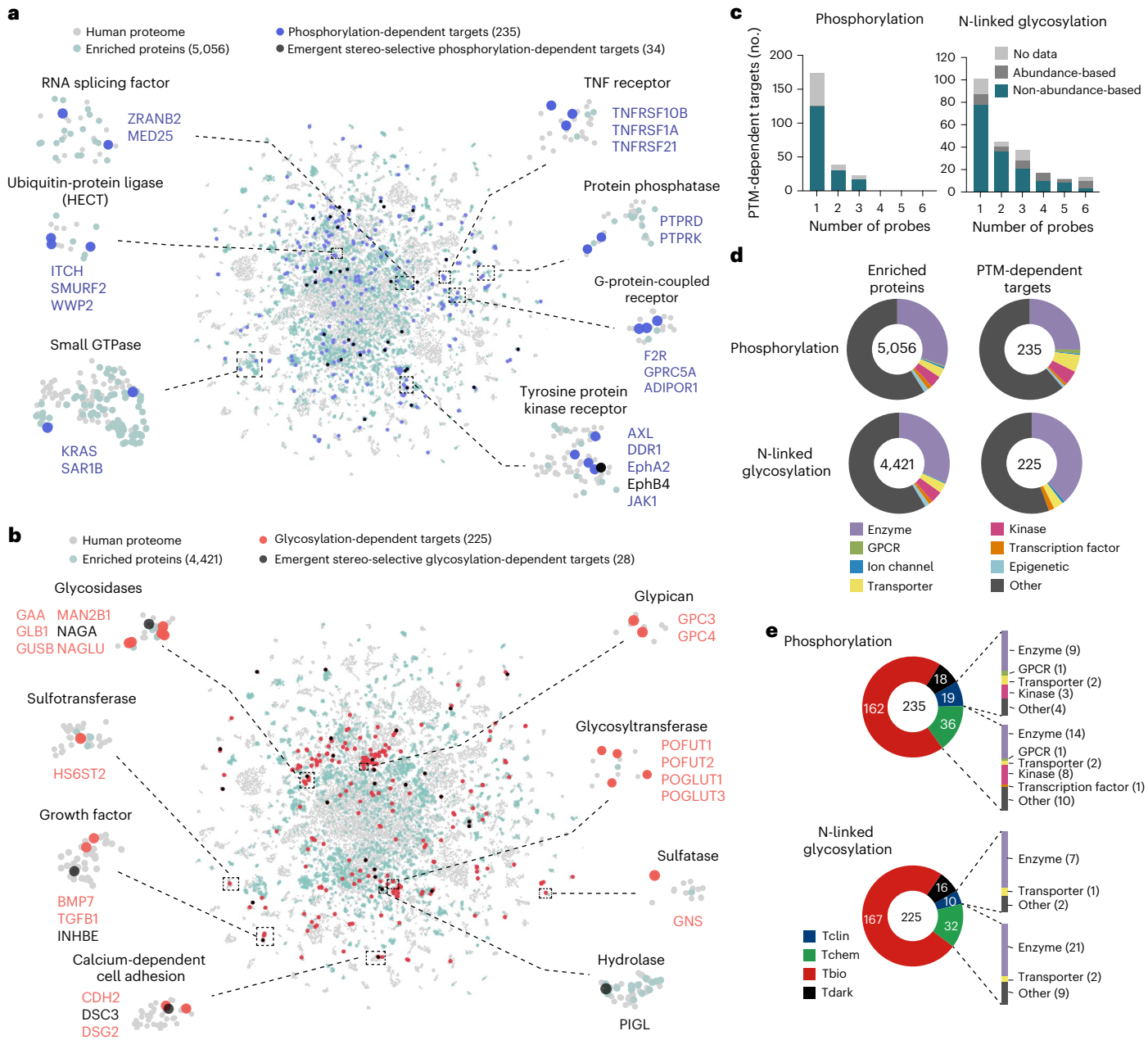



**Fig. 2 | Proteome-wide ligandability changes associated with PTM status.** **a**,**b**, Protein functional clustering of probe (100 µM)-enriched proteins and PTM-dependent targets. Green dots represent probe-enriched proteins (>5-fold enrichment over control probe, $P < 0.05$, $n = 2$). Blue and red dots denote phosphorylation-dependent and glycosylation-dependent targets, respectively, defined by >2-fold difference between DMSO and STR (blue) or Tuni (red) treatments ($P < 0.05$, $n = 2$). Black dots represent proteins with state-specific stereo-selective (emergent) interactions. **a**, Phosphorylation-associated ligandability profiles. **b**, N-linked glycosylation-associated ligandability profiles. **c**, Number of PTM-dependent targets detected by number of probes. Dark gray corresponds to targets with detected protein abundance changes (>2-fold, $P < 0.05$). Light gray represents proteins without abundance detection. **d**, IDG functional classes of enriched protein and PTM-dependent targets. **e**, IDG Target Development Level (TDL) of PTM-dependent targets, based on four categories: Tclin (targets of approved drugs), Tchem (targets with known bioactive compounds), Tbio (biologically characterized targets lacking drug-like modulators) and Tdark (poorly characterized proteins with limited functional information). IDG functional pathways are highlighted for Tclin and Tchem categories. Associated datasets are provided in Supplementary Tables 1–4 and 6 and 7.

(Extended Data Fig. 3c). Finally, dose-dependent probe labeling for a subset of targets (ATP6V1E1, EphA2, LAMTOR2, NPC2 and EDEM3) confirmed retention of state-selective binding over a broad range of concentrations (Extended Data Fig. 3d–m).

Among phosphorylation-dependent targets, 72 (31%) harbored phosphosites quantified in our phosphoproteomic experiments, enabling more detailed analyses. Of these, 34 displayed concordant changes in phosphorylation and ligandability (Extended Data Fig. 4a,b). For example, we observed significantly reduced phosphorylation at S686, S697 and S706 on the cell surface receptor CD44 and a concomitant decrease in binding with P2, whereas we observed increased phosphorylation on S144 of chromatin-associated protein NUCKS1 and increased binding with P2. We also observed 22 instances of ligandability changes that occur directionally opposite to observed phosphorylation changes. For example, the calmodulin-binding protein MARCKS displayed increased binding with probe P2 and decreased

https://doi.org/10.1038/s41589-026-02216-y

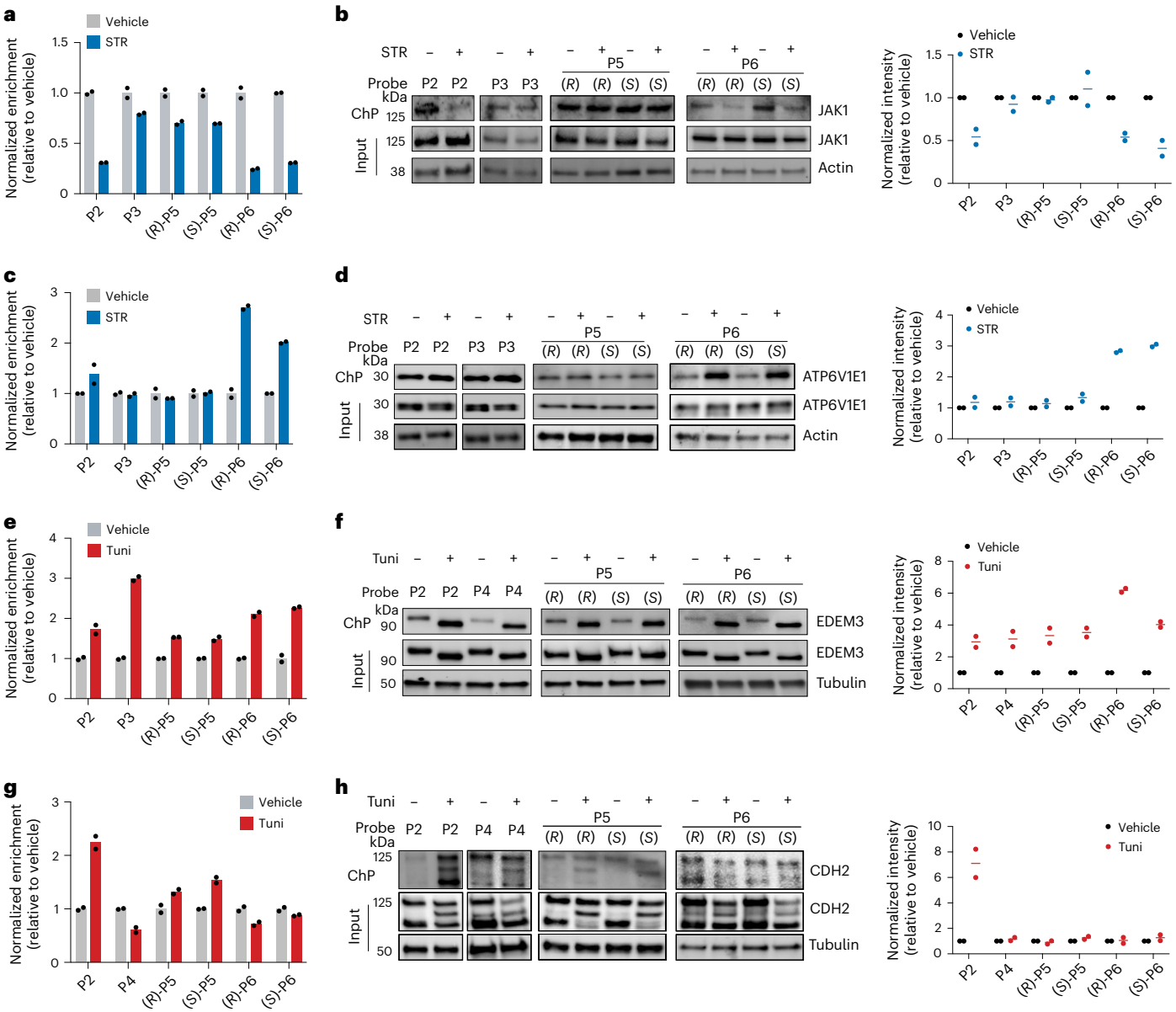



**Fig. 3 | Analysis and validation of PTM-dependent ligandability events.** Proteomic profiles and corresponding chemoprecipitation (ChP) validation for selected targets exhibiting PTM-sensitive probe (100 µM) binding: JAK1 (**a**,**b**), ATP6V1E1 (**c**,**d**), EDEM3 (**e**,**f**) and CDH2 (**g**,**h**). Panels **a**, **c**, **e** and **g** show quantification of chemoproteomic profiling; panels **b**,**d**,**f** and **h** present validation by ChP (left) and correlated quantification across biological replicates (right). Proteomic data and immunoblot quantification derived from two independent biological replicates are presented as the mean with individual data points overlaid. Associated datasets are provided in Supplementary Tables 1–8.

phosphorylation at S81 and T150. Finally, we also identified 16 targets without significant phosphorylation changes, including CLN3, a lysosomal protein with strong genetic links to Batten disease[29], where all reported phosphorylation sites were quantified in our phosphoproteomic experiments but were unaltered. Such instances indicate that differences in probe labeling likely occur indirectly from changes in phosphorylation status.

Among the glycosylation-dependent targets, we confirmed broadly increased ligandability across all probes for EDEM3 (Fig. 3e,f), an endoplasmic reticulum-localized glycoprotein with seven annotated N-linked glycosites[30]. We also validated CDH2, a cell membrane-localized adhesion glycoprotein (Fig. 3g,h), and DDOST, a subunit of the oligosaccharyltransferase (OST) complex, which, in contrast to EDEM3, displayed selective increased binding to P2 (Extended Data Fig. 5a) upon Tuni treatment. We noted a subset of targets (for example, HSPA5, HYOU1 and PDIA4) that were preferentially enriched by all six probes. Further inspection revealed that these events are largely related to changes in protein abundance and consist of members of the unfolded protein response (UPR), in line with previous reports demonstrating that Tuni activates this pathway (Extended Data Fig. 5b)[31]. We also identified 21 functionally diverse proteins that exhibit differential ligandability under both phosphorylation and glycosylation perturbations, often in divergent directions (Extended Data Fig. 5c,d), underscoring the complexity of PTM influence over small-molecule–protein interactions.

We and others have shown that integration of stereo-chemical features into probe design facilitates the confident assignment of authentic ligandable pockets on proteins[20,32,33]. As preluded in our gel-based profiles (Fig. 1d,f and Supplementary Fig. 1), we identified 62 ‘emergent’ stereo-selective liganding events across both

PTM perturbations (Fig. 2a,b and Extended Data Fig. 6a,b), wherein stereo-selective binding was found to occur in only one condition or state (34 in phosphorylation, 28 in glycosylation). Instances of emergent stereo-selective events in the phosphorylation dataset include CETN2, HIGD1A and EPHB4 (Extended Data Fig. 6c–e) as well as AS3MT, SLC25A4 and MPV17 (Extended Data Fig. 6f–h) in the glycosylation dataset. These data suggest that dynamic protein states can give rise to conditional stereo-selective liganding events.

### Characterizing PTM-dependent binding sites

We recently developed a quantitative chemical proteomic workflow to determine, with high resolution, proteome-wide binding sites of photoaffinity probes in cells (Supplementary Fig. 3)[21,34]. Using this method under the PTM perturbations described above, we identified differentially labeled binding sites ($P < 0.05$) on 82 and 55 proteins, respectively, for previously identified phosphorylation-dependent and glycosylation-dependent targets (Supplementary Data 1). We calculated the minimal spatial distance between labeled sequences and UniProt-annotated PTM sites based on experimental or predicted structural information. This analysis revealed that, perhaps not surprisingly, binding sites exhibiting PTM dependency are generally proximal to corresponding UniProt-annotated PTM sites (Fig. 4a, Supplementary Fig. 4a,b and Supplementary Data 1), suggestive that phosphate or N-glycan modifications may directly hinder or facilitate interactions between small molecules and proteins. We observed that differentially liganded sites often occurred near annotated functional sites (<10 Å), including active, ion-binding, cofactor-binding and nucleotide-binding sites, implicating potential roles of PTM status on protein function for these targets (Extended Data Fig. 7a). Notably, in the phosphorylation dataset, PTM-dependent sites were additionally enriched near non-canonical functional regions such as cleavage sites, reactive sites and key protein–protein interaction sites (Supplementary Fig. 4c–l).

We noted that a portion of identified sites overlapped with predicted small-molecule binding pockets (Extended Data Fig. 7b). Interestingly, we observed that pockets displaying PTM dependency generally overlap less frequently with predicted small-molecule binding pockets relative to pockets that do not display PTM dependency, suggesting that observed ligandability shifts occur within more dynamic sites rather than predictable, static pockets (Supplementary Fig. 4m,n). To begin to better understand molecular recognition components that might influence probe binding, we integrated our state-dependent site mapping data with molecular docking. We obtained atomic structures for a subset of interactions (57 structures from the Protein Data Bank (PDB) and 45 from AlphaFold) and then blindly docked every probe into every predicted pocket of unmodified protein structures and cross-referenced the results to the proteomics data[21]. We identified low-energy probe binding modes across a variety of pockets proximal to corresponding PTMs. These docked structures include diverse functional sites, such as ATP binding sites (TGFBR1), calcium binding sites (NUCB2 and CALM3) and phosphosites (COPE, HMGB1 and CD63) in phosphorylation-dependent pockets (Supplementary Fig. 5a–f) and protease cleavage sites (HBA1), substrate binding sites (HS6ST2), enzyme active sites (CTSB) and glycosites (OSTM1) in glycosylation-dependent pockets (Supplementary Fig. 5g–j).

Consulting matched phosphoproteomic measurements, we identified 20 binding pockets with altered ligandability within 10 Å of phosphosites exhibiting STR-dependent changes. Of these, six exhibited ligandability changes that correlated with phosphorylation changes, whereas the other 14 showed the opposite trend (Extended Data Fig. 7c). For instance, we observed selective increased binding of (*R*)-P6 with the heat shock protein HSPB1 (Fig. 4b) in a pocket proximal (approximately 5 Å) to S82, which decreases in phosphorylation (Fig. 4c), suggesting that the phosphate group may directly obstruct probe binding. By contrast, for CTSD, both (*R*)-P6 binding (Fig. 4d) and phosphorylation at S37 (approximately 6 Å) decreased (Fig. 4e), indicating that the phosphate group may, in some cases, facilitate probe binding. We also observed increased P2 binding to a pocket near S87/S88 on GABARAPL2, phosphosites implicated in the autophagic roles of GABARAPL2 (ref. 35) (Fig. 4f). Mutation of these residues (S87/S88A) to block phosphorylation led to substantial increased P2 binding, confirming the impact of phosphorylation on the ligandability of this site (Fig. 4g).

In addition to PTM-proximal pockets, we also identified several differentially liganded sites near protein–protein interfaces. For instance, we observed increased (*S*)-P5 binding to a pocket that is located at the interface of the GSTP1 homodimer and proximal to the glutathione binding site (Extended Data Fig. 7d). Interestingly, phosphorylation of GSTP1 shifts the dimer–monomer equilibrium and promotes the formation of the GSTP1–JNK complex[36], suggesting that dephosphorylation may result in the formation of a neopocket at the dimer interface that promotes probe binding. Consistent with this, we observed increased formation of GSTP1 dimers and multimers upon STR treatment (Extended Data Fig. 7e,f). However, we were unable to detect GSTP1 phosphorylation and, therefore, cannot assert whether these effects are caused by changes in GSTP1 phosphorylation status or other indirect effects. We also observed an increase in (*R*)-P6 binding of the metalloprotease inhibitor TIMP3 after STR treatment (Extended Data Fig. 7g), although TIMP3 is itself not annotated to be phosphorylated. Binding site inspection and molecular docking revealed that (*R*)-P6 likely binds to a pocket at the binding interface of TNF-converting enzyme (TACE), whose activity is inhibited upon TIMP3 binding[37]. Interestingly, we observed a significant decrease in TACE phosphorylation at S791 (Extended Data Fig. 7h) upon STR treatment, and mutation of S791 (S791A) resulted in substantial reduction in the TIMP3–TACE interaction as well as a concomitant increase in (*R*)-P6 binding (Extended Data Fig. 7i,j). Together, these data suggest that increased (*R*)-P6 binding of TIMP3 emanates from decreased stabilization of the TIMP3–TACE complex (and, therefore, exposing a ligandable pocket), which is mediated by S791 phosphorylation status. In another example, we observed increased binding of (*R*)-P6 to LAMTOR2, a subunit of the Ragulator–Rag complex[38], upon STR treatment (Fig. 4h and Supplementary Fig. 5k). Site mapping and docking suggest that the probe binds a pocket on LAMTOR2 that is occupied by LAMTOR1 in the intact Ragulator complex (Fig. 4i). Although several phosphosites have been reported in the Ragulator complex, primarily on LAMTOR1, we detected decreased phosphorylation only at S26 (Fig. 4j), which is distal to the (*R*)-P6-labeled site. This prompted us to test whether STR treatment may impact complex stability. Indeed, STR treatment substantially reduced LAMTOR1–LAMTOR2 interactions (Fig. 4k), suggesting that ligandability differences arise from disruption of the Ragulator complex and exposure binding pocket. From the glycosylation dataset, we observed an increased binding of P2 to calreticulin (CALR), a chaperone with specificity for monoglucosylated oligosaccharides, such as those of HLA-A, a component of the major histocompatibility complex class I (MHC I) complex[39]. Site mapping on CALR revealed increased binding at the glycoprotein interaction region, and structural docking showed that P2 occupies the same pocket as the N-linked glycan on N110 of HLA-A (Supplementary Fig. 5l), suggesting that substrate engagement may occlude probe binding.

As previously noted, we observed that a subset of proteins exhibited ligandability changes under both the STR-treated and Tuni-treated conditions (Extended Data Fig. 5c,d). Although these events occur at distinct binding sites, we identified cases where the same pocket displayed opposing ligandability changes depending on the treatment. For example, we mapped the binding site of both P2 and (*S*)-P6 to a shared pocket near the intracellular death domain of TNFRSF10B (DR5), the receptor for the cytotoxic ligand TNFSF10/TRAIL (Extended Data Fig. 7k). STR treatment reduced binding to

https://doi.org/10.1038/s41589-026-02216-y

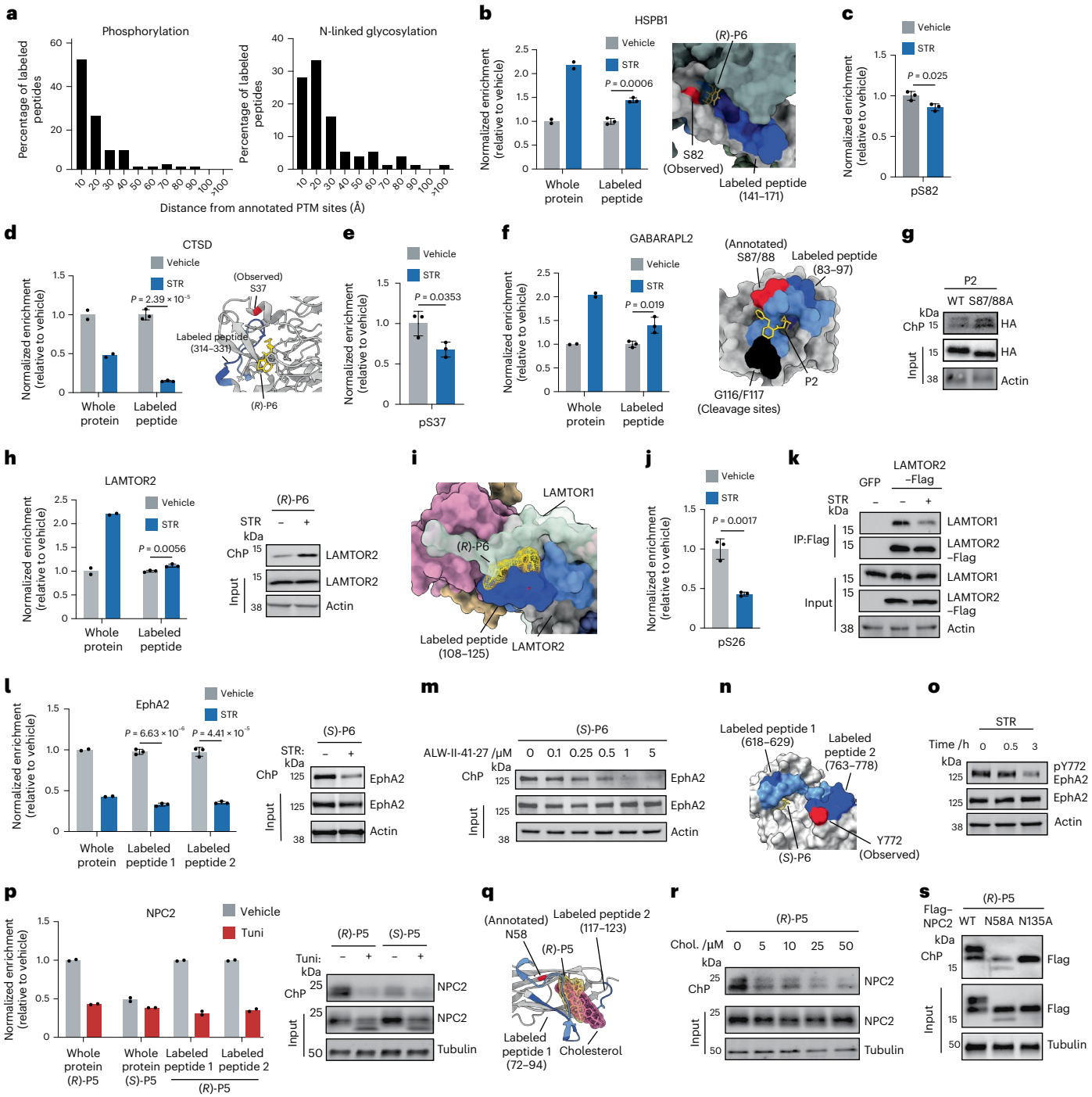



**Fig. 4 | Mapping PTM-dependent binding sites in cells. a**, Spatial distance distributions between probe-labeled peptides and Uniprot-annotated phosphorylation (left) and N-linked glycosylation (right) sites. **b**,**c**, Profiling and docking show that (*R*)-P6 binds HSPB1 near S82 (**b**, PDB: 6VD5), which is dephosphorylated upon STR treatment (**c**). **d**,**e**, Profiling and docking show that (*R*)-P6 binds CTSD near S37 (**d**, AF-P07339-F1), which undergoes STR-induced dephosphorylation (**e**). **f**,**g**, P2 labels GABARAPL2 near S87/88 (**f**, PDB: 7KL3), validated by chemoprecipitation (ChP) with wild-type (WT) and S87/88A mutant (**g**). **h**–**k**, Ligandability profiling and ChP validation of LAMTOR2 with (*R*)-P6 after STR treatment (**h**). **i**, Docked structure of LAMTOR2 (AF-Q9Y2Q5-F1) with (*R*)-P6 overlaps with the LAMTOR1 interface in the Ragulator complex (PDB: 5X6V). STR induces LAMTOR1 S26 dephosphorylation (**j**) and reduces LAMTOR1–LAMTOR2 complex formation (**k**). **l**–**o**, Ligandability profiling and ChP of EphA2 with (*S*)-P6 after STR treatment (**l**). Binding is competed by ALW-II-41-27 (**m**), as both share a site near the ATP pocket (**n**, PDB: 5EK7). STR induces EphA2 Y772 dephosphorylation (**o**). **p**–**s**, Ligandability profiling and ChP reveal PTM-selective and stereo-selective (*R*)-P5 binding to NPC2 after Tuni treatment (**p**). (*R*)-P5 binds the cholesterol pocket near glycosylated N58 (**q**), competed by cholesterol (**r**). N58 mutation disrupts (*R*)-P5 binding (**s**). Phosphorylation experiments were conducted in MDA-MB-231 cells with or without STR treatment (250 nM, 3 hours). Glycosylation experiments were conducted with or without Tuni (10 μg ml$^{-1}$, 24 hours) in HEK293T cells. All structures depict probe-labeled residues in dark blue; the remainder of each peptide in light blue; PTM sites in red (annotated: sites assigned in UniProt; observed: sites detected in phosphoproteomics); functional residues in black; and probes in gold. Proteomics and immunoblots represent the mean of two (data points overlaid) or three (±s.d.) independent biological replicates. Significance was determined using a two-tailed Student's *t*-test. Associated datasets are provided in Supplementary Tables 11 and 12. Chol., cholesterol; h, hours; IP, immunoprecipitation.

P2, whereas Tuni treatment increased binding with (*S*)-P6 at this site. Although TNFRSF10B lacks UniProt-annotated PTMs, it contains Asn-X-Ser/Thr ('X' denotes any amino acid but Pro) canonical N-glycosylation sequons and reported phosphosites (T381/Y383) within the death domain[40]. Although we did not identify any phosphopeptides from TNFRSF10B in our phosphoproteomic analysis, STR treatment decreased its phosphorylation levels detected via immunoblot (Extended Data Fig. 7l). Consistent with this, P2 labeling was substantially reduced in cells recombinantly expressing T381A/Y383A TNFRSF10B (Extended Data Fig. 7m), phenocopying STR treatment. Conversely, PNGase F treatment increased (*S*)-P6 binding (Extended Data Fig. 7n), mirroring the effect of Tuni. Although it remains unclear whether these effects arise from modification changes in TNFRSF10B or its interactors (for example, TNFSF10), these observations highlight the dynamic nature of pocket ligandability and the context-dependent effects of PTM status.

Among mapped binding pockets displaying PTM-dependent ligandability, several have known ligands, leading us to inquire whether changes in PTM status could affect binding of these ligands. For example, we identified a selective decrease in binding of probe (*S*)-P6 with the receptor tyrosine kinase EphA2 in the presence of STR (Fig. 4l). We identified two (*S*)-P6-labeled peptides on EphA2 located near the ATP binding pocket and binding site of ALW-II-41-27 (Supplementary Fig. 6a), an ATP-competitive EphA2 inhibitor[41]. We first validated this finding via immunoblotting (Fig. 4l and Supplementary Fig. 6b) and confirmed that the observed decrease in probe binding was not due to competitive binding with STR itself (Supplementary Fig. 6c). However, co-incubation of (*S*)-P6 with increasing concentrations of ALW-II-41-27 revealed clear blockade of probe labeling, indicating that they likely engage the same pocket (Fig. 4m), supported by binding site mapping and molecular docking (Fig. 4n). ALW-II-41-27 inhibitory activity decreases when Y772 on EphA2 is dephosphorylated[42], aligning with our observation that STR treatment lowers Y772 phosphorylation and correspondingly decreases (*S*)-P6 binding (Fig. 4o).

Among glycosylation-dependent targets, we identified NPC intracellular cholesterol transporter 2 (NPC2) (Fig. 4p), which facilitates lysosomal cholesterol egress, and mutations in NPC2 as well as NPC1 are associated with Niemann–Pick C disease[43]. We observed a stereo-selective decrease in (*R*)-P5 binding in Tuni-treated cells (Fig. 4p and Supplementary Fig. 6d), and binding site mapping and docking revealed that (*R*)-P5 engages the cholesterol-binding pocket (Fig. 4q). Consistent with this, co-incubation with cholesterol resulted in a dose-dependent decrease in (*R*)-P5 labeling (Fig. 4r and Supplementary Fig. 6e). We initially considered that reduced glycosylation may alter NPC2 lysosomal localization but observed minimal changes in localization after Tuni treatment (Supplementary Fig. 6f). NPC2 contains two reported N-linked glycosylation sites (N58 and N135)[44]. Structural analysis shows that N58 is proximal to the (*R*)-P5 site and the cholesterol-binding pocket (Fig. 4q), suggesting a direct role in ligand binding. Indeed, we observed that (*R*)-P5 binding was substantially reduced in the N58A mutant but not in the N135A mutant (Fig. 4s), suggesting that N-glycosylation on N58 may play a crucial role in small-molecule interactions of this pocket.

## Phosphorylation status alters KRAS inhibitor activity

Among targets with functional ligands displaying phosphorylation-dependent ligandability, we identified significant reduction of P3 binding to the small GTPase KRAS (Fig. 5a, Extended Data Fig. 8a and Supplementary Data 1). RAS family proteins, including KRAS, are molecular switches, receiving signals from growth factor receptors and relaying them to downstream effector pathways, which regulate processes such as cell growth and proliferation[45]. Somatic mutations on KRAS are the most common activating lesions found in cancer cells, with the most frequent occurring at codons 12 (G12), 13 (G13) and 61 (Q61), resulting in abnormal activation of the RAS pathway[46]. Substantial efforts have been made over the past decades to drug KRAS, particularly targeting oncogenic variants[45,47].

We first confirmed the identified P3 ligandability change against both endogenous $KRAS^{G13D}$ in MDA-MB-231 cells[48] (Fig. 5b and Extended Data Fig. 8b) and recombinantly expressed HA–$KRAS^{G13D}$ in Lenti-X 293T cells over a broad range of P3 concentrations (Supplementary Fig. 7a and Extended Data Fig. 8c,d). We also observed similar phosphorylation-dependent engagement with additional common mutants, including G12C and Q61H (Extended Data Fig. 8e,f and Supplementary Fig. 7a,b). By contrast, we observed directionally opposite P3 binding to $KRAS^{WT}$ (endogenous and recombinantly expressed) relative to the oncogenic mutants (Extended Data Fig. 8g) upon STR treatment. Moreover, cellular thermal shift assay (CETSA)[49] experiments using the unfunctionalized parent 6-aminocoumarin confirmed that this phosphorylation-dependent interaction extends to the binding of the fragment itself (Extended Data Fig. 8h,i). We mapped the binding site of P3 to a region adjacent to the switch-II (SII) pocket (Fig. 5c). Molecular docking to GDP-bound KRAS (PDB: 8B00) yielded a binding pose that overlaps with several KRAS inhibitors[50–53], including BI-2865 and AMG-510 (Supplementary Fig. 7c,d), and this assignment was supported by competition experiments in cells, where both inhibitors dose-dependently blocked probe binding (Fig. 5d and Extended Data Fig. 8j). Although these data localize P3 binding to the SII region and indicate overlap with inhibitor binding sites, we cannot unambiguously distinguish between occupation of the canonical SII pocket and the adjacent SI/SII pocket, both of which are known to accommodate ligands[54]. Consistent with engagement of this regulatory interface, we observed that GppNHp, a non-hydrolyzable analog of GTP, blocks P3 binding to $KRAS^{G13D}$, whereas GDP had no observable effect, demonstrating that P3 preferentially binds to the GDP-bound state (Extended Data Fig. 8k).

Inspection of P3's binding mode revealed its proximity to Y32 and Y64 (<10 Å), raising the possibility that phosphorylation of these sites contributes to the observed differential binding. Consistent with this, STR led to dephosphorylation of $KRAS^{G13D}$ (Fig. 5e), and phosphorylation-deficient Y32F and Y64F mutants showed ablated P3 binding to both G13D and G12C mutants, consistent with the effects observed with STR treatment of tyrosine counterparts (Fig. 5f and Extended Data Fig. 8l). Pharmacological inhibition of the KRAS phosphatase SHP2 with SHP099 (refs. 55,56) modestly increased P3 engagement in both MDA-MB-231 ($KRAS^{G13D}$) cells (Fig. 5g) and HCC44 ($KRAS^{G12C}$) cells (Extended Data Fig. 8e). Conversely, inhibition of c-Src kinase with dasatinib, which phosphorylates KRAS at Y32 and Y64 (refs. 56,57), reduced P3 binding (Supplementary Fig. 7e). Together, these data establish that phosphorylation at Y32 and Y64 modulates ligand engagement proximal to the SII pocket.

We next wondered whether phosphorylation would also affect the interaction between KRAS and SWII pocket inhibitors. Using CETSA, we found that BI-2865 induced robust thermal stabilization of KRAS in MDA-MB-231 cells, which was effectively diminished when the cells were co-treated with STR or dasatinib (Fig. 5h and Supplementary Fig. 7f,g). By contrast, treatment with SHP099 restored and even enhanced the stabilizing effects (Fig. 5h and Supplementary Fig. 7f), indicating that KRAS phosphorylation status influences inhibitor engagement. Because SWII inhibitors block interactions with c-Raf[51,53,58], we tested whether phosphorylation status impacts this activity. We observed a dose-dependent disruption of the RAS–RAF interaction in cells treated with BI-2865; however, this disruption was ablated upon STR treatment (Fig. 5i and Supplementary Fig. 8a), an effect sustained for at least 8 hours (Extended Data Fig. 9a). Critically, BI-2865 failed to disrupt KRAS–RAF in Y32F ($KRAS^{G13D\text{-}Y32F}$) and Y64F ($KRAS^{G13D\text{-}Y64F}$) mutants[58] (Extended Data Fig. 9b), consistent with the hypothesis that KRAS phosphorylation at these sites impacts inhibitor binding. Similar trends were observed with another non-covalent inhibitor (BI-2493) as well as covalent inhibitors (AMG-510 and MRTX-849), whose activities were likewise

https://doi.org/10.1038/s41589-026-02216-y

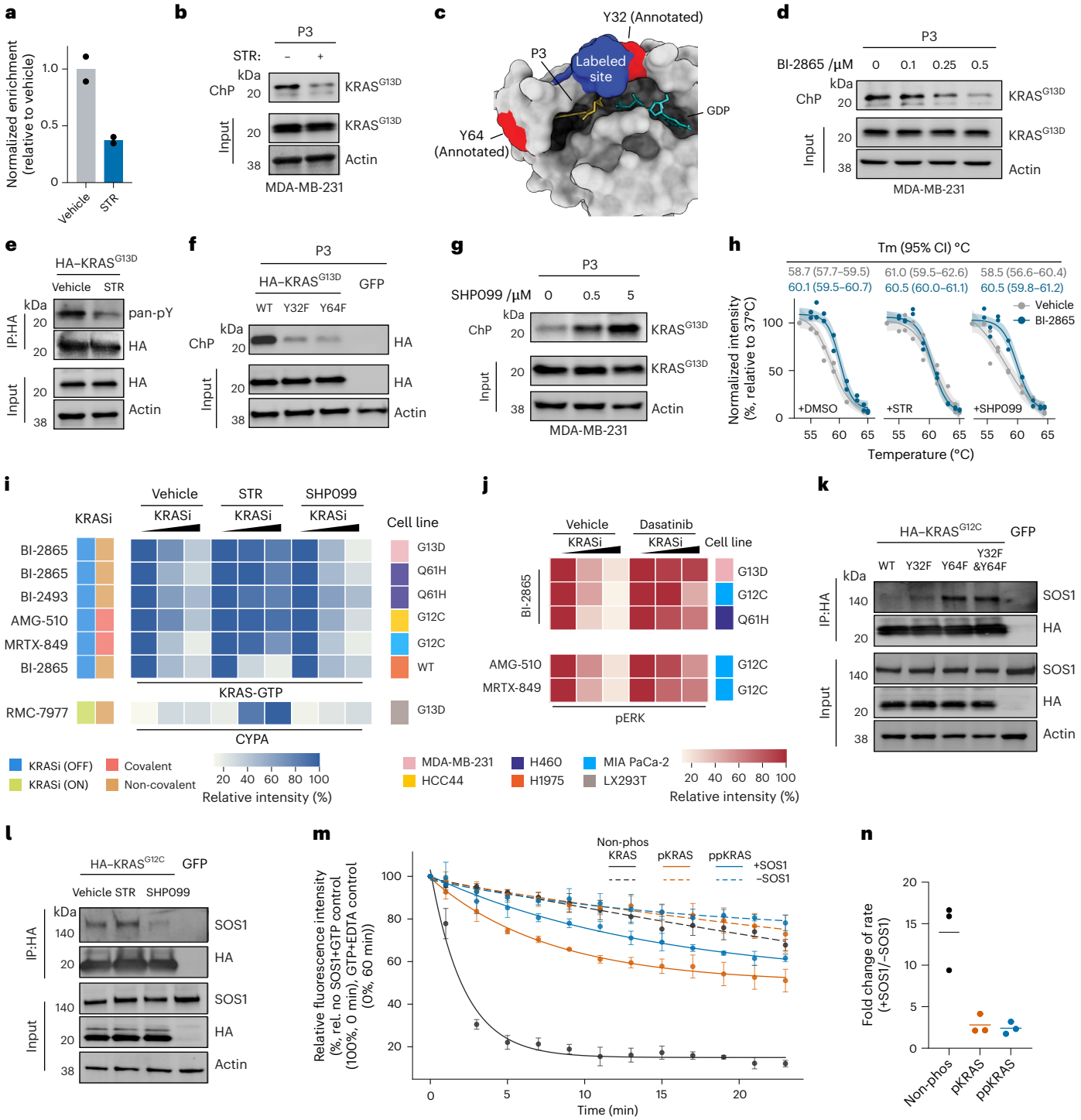



**Fig. 5 | KRAS phosphorylation status alters druggability. a**,**b**, Proteomic profile (**a**) and chemoprecipitation (ChP) validation (**b**) of P3 binding to KRAS$^{G13D}$ after STR treatment (250 nM, 3 hours, $n = 2$). **c**, Docked KRAS–P3 interaction near the SII pocket (PDB: 8B00), with P3-labeled residues shown in blue, phosphorylation sites (Y32 and Y64) in red, P3 in yellow and GDP in cyan. **d**, Dose-dependent P3 competition by the pan-KRAS inhibitor BI-2865. **e**, KRAS phosphorylation level decreased after STR (250 nM, 3 hours) treatment. HA-tagged KRAS was immunoprecipitated, and phosphorylation status was assessed by immunoblotting using a pan-phosphotyrosine antibody. **f**, ChP shows reduced P3 binding to Y32F and Y64F mutants of KRAS$^{G13D}$. **g**, Increased P3 engagement with KRAS$^{G13D}$ upon SHP2 inhibition by SHP099 (500 nM, 30 minutes). **h**, CETSA reveals decreased KRAS stabilization by BI-2865 in the presence of STR, whereas SHP099 has no observable effect. Data are presented as mean with 95% confidence intervals for curve fits. **i**, RBD assay shows that STR diminishes the ability of KRAS-OFF inhibitors to disrupt the active (GTP-bound) KRAS–RAF interaction across multiple KRAS-mutant cell lines, whereas SHP099 restores the effect. Immunoprecipitation (IP) reveals that STR enhances KRAS–CYPA ternary complex formation in the presence of the KRAS-ON state inhibitor RMC-7977. **j**, Total pERK (T202/Y204) levels assessed by immunoblotting in cells co-treated with dasatinib (1 μM) and indicated KRAS inhibitors restore pERK across various KRAS mutations in multiple cell lines. **k**,**l**, Co-IP shows that the KRAS–SOS1 interaction is enhanced by Y32F/Y64F mutation (**k**) and STR treatment (**l**) but attenuated by SHP099 (**l**). **m**, In vitro fluorescence-based nucleotide exchange assay demonstrates that phosphorylation impedes SOS1-mediated GDP release, as mono-phosphorylated (pKRAS) and di-phosphorylated (ppKRAS) forms exhibit slower exchange kinetics compared to non-phosphorylated KRAS (KRAS:SOS 10:1). **n**, Quantification of the fold change in exchange rates (+SOS1/–SOS1). Proteomics and immunoblots represent the mean of two (data points overlaid) or three (±s.d.) independent biological replicates. See Supplementary Tables 2 and 13 for related datasets. CI, confidence interval; Tm, melting temperature; KRASi, KRAS inhibitor; min, minutes; WT, wild-type.

diminished in cells treated with STR (Fig. 5i and Supplementary Fig. 8a) or dasatinib (Extended Data Fig. 9c,d). We observed similar effects with BI-2865-treated or BI-2493-treated H460 cells harboring the Q61H mutation, which exhibits impaired intrinsic and GAP-mediated GTP hydrolysis[59–61], possibly indicating that phosphorylation-dependent modulation of inhibitor engagement is not explained solely by altered nucleotide cycling (Extended Data Fig. 9e and Supplementary Fig. 8a).

Intriguingly, treatment of cells with RMC-7977, which targets GTP-bound KRAS via ternary complex with cyclophilin A (CYPA) to block the RAS–RAF interaction[62], resulted in increased CYPA binding upon STR treatment, as did $KRAS^{G13D\text{-}Y32F}$ and $KRAS^{G13D\text{-}Y64F}$ mutations (Fig. 5i and Extended Data Fig. 9f,g). These findings suggest that phosphorylation differentially modulates the activity of KRAS-OFF and KRAS-ON inhibitors. Consistent with our observations with P3 binding, this effect appears to be mutant specific, as STR had no effect on the ability of BI-2865 to disrupt the KRAS–RAF interaction in H1975 cells, which express $KRAS^{WT}$ (Fig. 5i and Supplementary Fig. 8a). Finally, we observed a restoration of downstream phospho-ERK signaling when KRAS G12, G13 or Q61 mutant cells are co-treated with KRAS inhibitors and dasatinib, demonstrating that phosphorylation status influences both inhibitor binding and functional suppression (Fig. 5j and Supplementary Fig. 8b).

Phosphorylation of Y32 and Y64 has been shown to impact KRAS structural conformation, impacting interactions with the effector RAF and GTP cycling[56,59,63], suggesting that the observed ligandability differences may, in part, arise from phosphorylation-dependent changes around the SII region. Consistent with this, unbiased enhanced sampling molecular dynamics simulations revealed that phosphorylation at Y64 in GDP-bound $KRAS^{G13D}$ decreases SII flexibility while increasing SI flexibility (Extended Data Fig. 10a,b and Supplementary Fig. 9). Metadynamics-derived free energy surfaces further suggested that phosphorylation at Y32 or Y64 induces a drastic shift in the conformational population, reshaping the energy landscape in a way that might favor a closed-like state compatible with BI-2865 binding (Extended Data Fig. 10c). To test whether these predicted conformational shifts directly alter BI-2865 affinity, we generated, purified and characterized non-phosphorylated, mono-phosphorylated (pY64 and pKRAS) and di-phosphorylated (pY32/pY64 and ppKRAS) $KRAS^{G12C}$ variants (Supplementary Fig. 10a–e and Supplementary Table 15). However, surface plasmon resonance (SPR) measurements revealed no differences in BI-2865 binding affinity (Extended Data Fig. 10d–g), indicating that phosphorylation does not measurably alter intrinsic ligand affinity.

We, therefore, considered whether phosphorylation modulates KRAS regulatory interactions. The crystal structure of KRAS in complex with the guanine nucleotide exchange factor SOS1 (PDB: 6EPL; Supplementary Fig. 10f) shows that Y64 participates in hydrophobic interactions at the RAS–SOS interface[58,64]. Previous work showed that Y64A substitution reduces RAS GTPase activity, impairs SOS interaction and diminishes SII inhibitor activity[58,65–67], while Y32S was also reported to decrease nucleotide exchange[68–70]. We, therefore, asked whether phosphorylation at these residues modulates SOS–KRAS association. Cells expressing recombinant $KRAS^{Y64F}$ (G12C or G13D), which preserves aromaticity while preventing phosphorylation, exhibited substantially increased SOS1 binding relative to non-mutated KRAS, whereas $KRAS^{Y32F}$ showed little to no enhancement. Similarly, STR treatment significantly enhanced SOS1 association with KRAS, whereas SHP099 abrogated this effect (Fig. 5k,l and Extended Data Fig. 10h–m). Consistent with these observations, phosphorylation significantly reduced (approximately seven-fold) the rate of SOS-mediated GDP–GTP exchange (Fig. 5m,n and Extended Data Fig. 10n), with minimal effects on intrinsic exchange. Collectively, these data support a model where phosphorylation of Y64 disrupts SOS binding and SOS-mediated nucleotide exchange, enriching a GDP-bound state preferred by ligands overlapping the SII inhibitor binding site (Supplementary Fig. 10g).

## Discussion

Although previous efforts systematically cataloged PTM prevalence and dynamics through MS[5], translating these high-dimensional datasets into actionable insight regarding protein function, chemical tractability or druggability remains limited[71]. A limited number of examples, often discovered serendipitously, demonstrate direct PTM-dependent modulation of ligandability. For instance, unphosphorylated Abelson (Abl) tyrosine kinase exhibits over 150-fold greater sensitivity to inhibition by imatinib; acetylation of CYPA antagonizes the immunosuppressive effects of cyclosporin[72,73]; and α1-acid glycoprotein (AGP) exhibits glycoform-dependent binding to warfarin[74]. Recent chemical proteomic studies have similarly identified instances of context-dependent liganding events, highlighting the potential of this strategy to broadly assess state-dependent pharmacology[8,75,76]. Our approach directly addresses this gap by enabling proteome-wide assessment of how phosphorylation, N-linked glycosylation and, in principle, any PTM or cellular state can influence small-molecule–protein interactions.

The implications of our findings extend broadly across biological and therapeutic contexts. PTM-dependent ligandability events span diverse protein classes, including traditionally challenging drug targets such as transcription factors and epigenetic regulators. Our data point to a wide range of mechanisms, beyond abundance changes, by which PTMs may affect protein ligandability. We observed strong enrichment of differentially liganded sites proximal to corresponding altered PTM (Fig. 4a–g), suggesting direct shaping of ligand binding pockets, either by altering pocket accessibility orthosterically or influencing conformational dynamics. We also identified distal events (Extended Data Fig. 7k–n), exemplified by LAMTOR2, where STR-mediated disruption of the Ragulator complex appears to create a 'neo-pocket' (Fig. 4h–k). Notably, ligandability changes frequently localize to annotated functional regions (Extended Data Fig. 7a,b and Supplementary Figs. 4 and 5), including active sites, substrate-binding pockets, protein–protein interfaces as well as functionally unannotated sites, supporting the idea that ligandability can serve as a proxy for protein status—reporting shifts in conformation, interactions and other functions beyond direct small-molecule binding.

Critically, our study also identified clinically relevant targets, such as KRAS, whose phosphorylation state profoundly influences inhibitor efficacy. This raises important considerations for how chemical probes and approved drugs behave across cellular states. SHP2 inhibitors impair growth and induce death in KRAS-driven cancers, and their combination with KRAS inhibitors has resulted in enhanced efficacy in clinical settings[77,78]. These findings have largely been attributed to coordinated suppression of upstream RTK signaling and altered KRAS GTP cycling through direct GEF and GAP modulation[56,79–87]. Extensive work has shown that phosphorylation of KRAS alters switch dynamics and perturbs GTPase cycling, leading to insensitivity to GEF-mediated and GAP-mediated regulation and impaired effector engagement[56,59,63]. However, our observation that phosphorylation has similar impacts to cells harboring G12/G13 mutants, as well as the Q61H mutant, suggests that additional KRAS-intrinsic factors mediated by phosphorylation may contribute to the observed effects of ligand binding to the SII region. We show that phosphorylation of KRAS, particularly at Y64, reduces interactions with SOS, leading to increased levels of GDP-bound KRAS and correspondingly enhanced engagement with SWII ligands. Wild-type KRAS exhibits opposing phosphorylation-dependent ligandability patterns relative to oncogenic mutants, and RMC-7977-mediated KRAS–CYPA stabilization is enhanced upon KRAS dephosphorylation, underscoring a multilayered regulation of pocket activity. Together, these results highlight PTM-dependent ligandability as a previously underappreciated determinant of KRAS inhibitor response and suggest opportunities to optimize therapies tailored to specific cellular states.

Several limitations warrant consideration. Although we observed more than 400 PTM-dependent ligandability events, our analysis was

restricted to phosphorylation and N-linked glycosylation perturbed by STR and Tuni, respectively, and thus reflects a relatively limited perspective of how PTMs and other factors might influence proteome-wide ligandability. Additionally, all experiments were conducted in HEK293T or MDA-MB-231 cells, confining our coverage to proteins expressed in these cells. Extending this approach to additional PTMs, cellular states, disease-relevant contexts and diverse tissues will further illuminate how protein status shapes ligandability and druggability. Moreover, although we employed relatively promiscuous fragment probes, our library is small and generally lipophilic and inadequately covers broad chemical space. Larger libraries with structurally diverse and stereo-chemically defined members should enable deeper examination of the proteome and facilitate discovery of state-dependent chemicals[33,88,89]. Integrating computational methods to model the structural impact of PTMs on small-molecule binding en masse could complement experimental efforts and perhaps enable state-dependent drug discovery de novo. Finally, although PTM databases (for example, UniProt and PhosphoSitePlus) serve as valuable resources for generating mechanistic hypotheses, these annotated sites may not always reflect the specific PTM status under considered experimental conditions, underscoring the need for targeted PTM validation on a case-by-case basis. Collectively, this work provides a framework not only to investigate how PTMs modulate protein status but also to discover chemical probes tailored to specific functional or pathological contexts.

## Online content

Any methods, additional references, Nature Portfolio reporting summaries, source data, extended data, supplementary information, acknowledgements, peer review information; details of author contributions and competing interests; and statements of data and code availability are available at https://doi.org/10.1038/s41589-026-02216-y.

## References


1. Huang, X. et al. PTMD 2.0: an updated database of disease-associated post-translational modifications. *Nucleic Acids Res.* **53**, D554–D563 (2025).
2. Aebersold, R. et al. How many human proteoforms are there? *Nat. Chem. Biol.* **14**, 206–214 (2018).
3. Aebersold, R. & Mann, M. Mass-spectrometric exploration of proteome structure and function. *Nature* **537**, 347–355 (2016).
4. Olsen, J. V. & Mann, M. Status of large-scale analysis of post-translational modifications by mass spectrometry. *Mol. Cell. Proteomics* **12**, 3444–3452 (2013).
5. Doll, S. & Burlingame, A. L. Mass spectrometry-based detection and assignment of protein posttranslational modifications. *ACS Chem. Biol.* **10**, 63–71 (2015).
6. Parker, C. G. & Pratt, M. R. Click chemistry in proteomic investigations. *Cell* **180**, 605–632 (2020).
7. Grammel, M. & Hang, H. C. Chemical reporters for biological discovery. *Nat. Chem. Biol.* **9**, 475–484 (2013).
8. Vinogradova, E. V. et al. An activity-guided map of electrophile-cysteine interactions in primary human T cells. *Cell* **182**, 1009–1026 (2020).
9. Kemper, E. K., Zhang, Y., Dix, M. M. & Cravatt, B. F. Global profiling of phosphorylation-dependent changes in cysteine reactivity. *Nat. Methods* **19**, 341–352 (2022).
10. Takahashi, M. et al. DrugMap: a quantitative pan-cancer analysis of cysteine ligandability. *Cell* **187**, 2536–2556 (2024).
11. Jessani, N., Liu, Y., Humphrey, M. & Cravatt, B. F. Enzyme activity profiles of the secreted and membrane proteome that depict cancer cell invasiveness. *Proc. Natl Acad. Sci. USA* **99**, 10335–10340 (2002).
12. Gupta, V., Yang, J., Liebler, D. C. & Carroll, K. S. Diverse redoxome reactivity profiles of carbon nucleophiles. *J. Am. Chem. Soc.* **139**, 5588–5595 (2017).
13. Kisty, E. A., Falco, J. A. & Weerapana, E. Redox proteomics combined with proximity labeling enables monitoring of localized cysteine oxidation in cells. *Cell Chem. Biol.* **30**, 321–336 (2023).
14. Ardito, F., Giuliani, M., Perrone, D., Troiano, G. & Lo Muzio, L. The crucial role of protein phosphorylation in cell signaling and its use as targeted therapy. *Int. J. Mol. Med.* **40**, 271–280 (2017).
15. Schjoldager, K. T., Narimatsu, Y., Joshi, H. J. & Clausen, H. Global view of human protein glycosylation pathways and functions. *Nat. Rev. Mol. Cell Biol.* **21**, 729–749 (2020).
16. Cohen, P., Cross, D. & Jänne, P. A. Kinase drug discovery 20 years after imatinib: progress and future directions. *Nat. Rev. Drug Discov.* **20**, 551–569 (2021).
17. Kim, Y. et al. Glycosidase-targeting small molecules for biological and therapeutic applications. *Chem. Soc. Rev.* **52**, 7036–7070 (2023).
18. White, J. et al. Histone lysine acetyltransferase inhibitors: an emerging class of drugs for cancer therapy. *Trends Pharmacol. Sci.* **45**, 243–254 (2024).
19. Gani, O. A. & Engh, R. A. Protein kinase inhibition of clinically important staurosporine analogues. *Nat. Prod. Rep.* **27**, 489–498 (2010).
20. Wang, Y. et al. Expedited mapping of the ligandable proteome using fully functionalized enantiomeric probe pairs. *Nat. Chem.* **11**, 1113–1123 (2019).
21. Wozniak, J. M. et al. Enhanced mapping of small-molecule binding sites in cells. *Nat. Chem. Biol.* **20**, 823–834 (2024).
22. Chiu, T.-Y. et al. Chemoproteomic development of SLC15A4 inhibitors with anti-inflammatory activity. *Nat. Chem. Biol.* **20**, 1000–1011 (2024).
23. Offensperger, F. et al. Large-scale chemoproteomics expedites ligand discovery and predicts ligand behavior in cells. *Science* **384**, eadk5864 (2024).
24. Parker, C. G. et al. Ligand and target discovery by fragment-based screening in human cells. *Cell* **168**, 527–541 (2017).
25. Rostovtsev, V. V., Green, L. G., Fokin, V. V. & Sharpless, K. B. A stepwise huisgen cycloaddition process: copper(I)-catalyzed regioselective 'ligation' of azides and terminal alkynes. *Angew. Chem.* **114**, 2708–2711 (2002).
26. Esko, J. D., Bertozzi, C. & Schnaar, R. L. Chemical tools for inhibiting glycosylation. In *Essentials of Glycobiology* 3rd edn (eds Varki, A. et al.) (Cold Spring Harbor Laboratory Press, 2017).
27. Vilen, Z., Joeh, E., Critcher, M., Parker, C. G. & Huang, M. L. Proximity tagging identifies the glycan-mediated glycoprotein interactors of galectin-1 in muscle stem cells. *ACS Chem. Biol.* **16**, 1994–2003 (2021).
28. Sharma, K. R., Colvis, C. M., Rodgers, G. P. & Sheeley, D. M. Illuminating the druggable genome: pathways to progress. *Drug Discov. Today* **29**, 103805 (2024).
29. Calcagni', A. et al. Loss of the batten disease protein CLN3 leads to mis-trafficking of M6PR and defective autophagic-lysosomal reformation. *Nat. Commun.* **14**, 3911 (2023).
30. Hirao, K. et al. EDEM3, a soluble EDEM homolog, enhances glycoprotein endoplasmic reticulum-associated degradation and mannose trimming. *J. Biol. Chem.* **281**, 9650–9658 (2006).
31. Wiseman, R. L., Mesgarzadeh, J. S. & Hendershot, L. M. Reshaping endoplasmic reticulum quality control through the unfolded protein response. *Mol. Cell* **82**, 1477–1491 (2022).
32. Scott, K. A. et al. Stereochemical diversity as a source of discovery in chemical biology. *Curr. Res. Chem. Biol.* **2**, 100028 (2022).
33. Ogasawara, D. et al. Chemical tools to expand the ligandable proteome: diversity-oriented synthesis-based photoreactive stereoprobes. *Cell Chem. Biol.* **31**, 2138–2155 (2024).
34. Wozniak, J. M., Li, W. & Parker, C. G. Chemical proteomic mapping of reversible small molecule binding sites in native systems. *Trends Pharmacol. Sci.* **45**, 969–981 (2024).

35. Herhaus, L. et al. TBK1-mediated phosphorylation of LC3C and GABARAP-L2 controls autophagosome shedding by ATG4 protease. *EMBO Rep.* **21**, e48317 (2020).
36. Okamura, T. et al. Phosphorylation of glutathione S-transferase P1 (GSTP1) by epidermal growth factor receptor (EGFR) promotes formation of the GSTP1-c-Jun N-terminal kinase (JNK) complex and suppresses JNK downstream signaling and apoptosis in brain tumor cells. *J. Biol. Chem.* **290**, 30866–30878 (2015).
37. Amour, A. et al. TNF-α converting enzyme (TACE) is inhibited by TIMP-3. *FEBS Lett.* **435**, 39–44 (1998).
38. Mu, Z., Wang, L., Deng, W., Wang, J. & Wu, G. Structural insight into the Ragulator complex which anchors mTORC1 to the lysosomal membrane. *Cell Discov.* **3**, 17049 (2017).
39. Domnick, A. et al. Molecular basis of MHC I quality control in the peptide loading complex. *Nat. Commun.* **13**, 4701 (2022).
40. Hornbeck, P. V. et al. PhosphoSitePlus, 2014: mutations, PTMs and recalibrations. *Nucleic Acids Res.* **43**, D512–D520 (2014).
41. Choi, Y. et al. Discovery and structural analysis of Eph receptor tyrosine kinase inhibitors. *Bioorg. Med. Chem. Lett.* **19**, 4467–4470 (2009).
42. Xiang, Y.-P. et al. Y772 phosphorylation of EphA2 is responsible for EphA2-dependent NPC nasopharyngeal carcinoma growth by Shp2/Erk-1/2 signaling pathway. *Cell Death Dis.* **11**, 709 (2020).
43. Infante, R. E. et al. NPC2 facilitates bidirectional transfer of cholesterol between NPC1 and lipid bilayers, a step in cholesterol egress from lysosomes. *Proc. Natl Acad. Sci. USA* **105**, 15287–15292 (2008).
44. Chikh, K., Vey, S., Simonot, C., Vanier, M. T. & Millat, G. Niemann–Pick type C disease: importance of N-glycosylation sites for function and cellular location of the NPC2 protein. *Mol. Genet. Metab.* **83**, 220–230 (2004).
45. Singhal, A., Li, B. T. & O'Reilly, E. M. Targeting KRAS in cancer. *Nat. Med.* **30**, 969–983 (2024).
46. Huang, L., Guo, Z., Wang, F. & Fu, L. KRAS mutation: from undruggable to druggable in cancer. *Signal Transduct. Target. Ther.* **6**, 386 (2021).
47. Bar-Sagi, D., Knelson, E. H. & Sequist, L. V. A bright future for KRAS inhibitors. *Nat. Cancer* **1**, 25–27 (2020).
48. Kozma, S. C. et al. The human c-Kirsten *ras*gene is activated by a novel mutation in codon 13 in the breast carcinoma cell line MDA-MB231. *Nucleic Acids Res.* **15**, 5963–5971 (1987).
49. Molina, D. M. et al. Monitoring drug target engagement in cells and tissues using the cellular thermal shift assay. *Science* **341**, 84–87 (2013).
50. Ostrem, J. M. L. & Shokat, K. M. Direct small-molecule inhibitors of KRAS: from structural insights to mechanism-based design. *Nat. Rev. Drug Discov.* **15**, 771–785 (2016).
51. Fell, J. B. et al. Identification of the clinical development candidate MRTX849, a covalent $KRAS^{G12C}$ inhibitor for the treatment of cancer. *J. Med. Chem.* **63**, 6679–6693 (2020).
52. Canon, J. et al. The clinical KRAS(G12C) inhibitor AMG 510 drives anti-tumour immunity. *Nature* **575**, 217–223 (2019).
53. Kim, D. et al. Pan-KRAS inhibitor disables oncogenic signalling and tumour growth. *Nature* **619**, 160–166 (2023).
54. Vasta, J. D. et al. KRAS is vulnerable to reversible switch-II pocket engagement in cells. *Nat. Chem. Biol.* **18**, 596–604 (2022).
55. Chen, Y.-N. P. et al. Allosteric inhibition of SHP2 phosphatase inhibits cancers driven by receptor tyrosine kinases. *Nature* **535**, 148–152 (2016).
56. Kano, Y. et al. Tyrosyl phosphorylation of KRAS stalls GTPase cycle via alteration of switch I and II conformation. *Nat. Commun.* **10**, 224 (2019).
57. Lombardo, L. J. et al. Discovery of N-(2-chloro-6-methyl- phenyl)-2-(6-(4-(2-hydroxyethyl)- piperazin-1-yl)-2-methylpyrimidin-4-ylamino)thiazole-5-carboxamide (BMS-354825), a dual Src/Abl kinase inhibitor with potent antitumor activity in preclinical assays. *J. Med. Chem.* **47**, 6658–6661 (2004).
58. Lito, P., Solomon, M., Li, L.-S., Hansen, R. & Rosen, N. Allele-specific inhibitors inactivate mutant KRAS G12C by a trapping mechanism. *Science* **351**, 604–608 (2016).
59. Gebregiworgis, T. et al. The Q61H mutation decouples KRAS from upstream regulation and renders cancer cells resistant to SHP2 inhibitors. *Nat. Commun.* **12**, 6274 (2021).
60. Buhrman, G., Holzapfel, G., Fetics, S. & Mattos, C. Allosteric modulation of Ras positions Q61 for a direct role in catalysis. *Proc. Natl Acad. Sci. USA* **107**, 4931–4936 (2010).
61. Der, C. J., Finkel, T. & Cooper, G. M. Biological and biochemical properties of human $ras^{H}$ genes mutated at codon 61. *Cell* **44**, 167–176 (1986).
62. Holderfield, M. et al. Concurrent inhibition of oncogenic and wild-type RAS-GTP for cancer therapy. *Nature* **629**, 919–926 (2024).
63. Bunda, S. et al. Src promotes GTPase activity of Ras via tyrosine 32 phosphorylation. *Proc. Natl Acad. Sci. USA* **111**, E3785–E3794 (2014).
64. Hillig, R. C. et al. Discovery of potent SOS1 inhibitors that block RAS activation via disruption of the RAS–SOS1 interaction. *Proc. Natl Acad. Sci. USA* **116**, 2551–2560 (2019).
65. Margarit, S. M. et al. Structural evidence for feedback activation by Ras·GTP of the Ras-specific nucleotide exchange factor SOS. *Cell* **112**, 685–695 (2003).
66. Boriack-Sjodin, P. A., Margarit, S. M., Bar-Sagi, D. & Kuriyan, J. The structural basis of the activation of Ras by Sos. *Nature* **394**, 337–343 (1998).
67. Sondermann, H. et al. Structural analysis of autoinhibition in the Ras activator Son of sevenless. *Cell* **119**, 393–405 (2004).
68. Feig, L. A. & Cooper, G. M. Relationship among guanine nucleotide exchange, GTP hydrolysis, and transforming potential of mutated *ras*proteins. *Mol. Cell. Biol.* **8**, 2472–2478 (1988).
69. Hall, B. E., Yang, S. S., Boriack-Sjodin, P. A., Kuriyan, J. & Bar-Sagi, D. Structure-based mutagenesis reveals distinct functions for Ras switch 1 and switch 2 in Sos-catalyzed guanine nucleotide exchange. *J. Biol. Chem.* **276**, 27629–27637 (2001).
70. Patel, G., MacDonald, M. J., Khosravi-Far, R., Hisaka, M. M. & Der, C. J. Alternate mechanisms of ras activation are complementary and favor and formation of ras-GTP. *Oncogene* **7**, 283–288 (1992).
71. Brenner, S. Sequences and consequences. *Philos. Trans. R. Soc. Lond. B Biol. Sci.* **365**, 207–212 (2010).
72. Schindler, T. et al. Structural mechanism for STI-571 inhibition of abelson tyrosine kinase. *Science* **289**, 1938–1942 (2000).
73. Lammers, M., Neumann, H., Chin, J. W. & James, L. C. Acetylation regulates Cyclophilin A catalysis, immunosuppression and HIV isomerization. *Nat. Chem. Biol.* **6**, 331–337 (2010).
74. Wu, D., Struwe, W. B., Harvey, D. J., Ferguson, M. A. J. & Robinson, C. V. N-glycan microheterogeneity regulates interactions of plasma proteins. *Proc. Natl Acad. Sci. USA* **115**, 8763–8768 (2018).
75. Goetzke, F. W. et al. Complexoform-restricted covalent TRMT112 ligands that allosterically agonize METTL5. *Nat. Chem. Biol.* https://doi.org/10.1038/s41589-025-02099-5 (2026).
76. Kavanagh, M. E. et al. Selective inhibitors of JAK1 targeting an isoform-restricted allosteric cysteine. *Nat. Chem. Biol.* **18**, 1388–1398 (2022).
77. Li, T. et al. Developing SHP2-based combination therapy for KRAS-amplified cancer. *JCI Insight* **8**, e152714 (2023).

78. Wang, J. et al. 653O Glecirasib (KRAS G12C inhibitor) in combination with JAB-3312 (SHP2 inhibitor) in patients with KRAS p.G12C mutated solid tumors. *Ann. Oncol.* **34**, S459 (2023).
79. Ruess, D. A. et al. Mutant *KRAS*-driven cancers depend on *PTPN11*/SHP2 phosphatase. *Nat. Med.* **24**, 954–960 (2018).
80. Wong, G. S. et al. Targeting wild-type *KRAS*-amplified gastroesophageal cancer through combined MEK and SHP2 inhibition. *Nat. Med.* **24**, 968–977 (2018).
81. Nichols, R. J. et al. RAS nucleotide cycling underlies the SHP2 phosphatase dependence of mutant BRAF-, NF1- and RAS-driven cancers. *Nat. Cell Biol.* **20**, 1064–1073 (2018).
82. Mainardi, S. et al. SHP2 is required for growth of *KRAS*-mutant non-small-cell lung cancer in vivo. *Nat. Med.* **24**, 961–967 (2018).
83. Bennett, A. M., Tang, T. L., Sugimoto, S., Walsh, C. T. & Neel, B. G. Protein-tyrosine-phosphatase SHPTP2 couples platelet-derived growth factor receptor beta to Ras. *Proc. Natl Acad. Sci. USA* **91**, 7335–7339 (1994).
84. Li, W. et al. A new function for a phosphotyrosine phosphatase: linking GRB2-Sos to a receptor tyrosine kinase. *Mol. Cell. Biol.* **14**, 509–517 (1994).
85. Agazie, Y. M. & Hayman, M. J. Molecular mechanism for a role of SHP2 in epidermal growth factor receptor signaling. *Mol. Cell. Biol.* **23**, 7875–7886 (2003).
86. Lou, K. et al. $KRAS^{G12C}$ inhibition produces a driver-limited state revealing collateral dependencies. *Sci. Signal.* **12**, eaaw9450 (2019).
87. Fedele, C. et al. SHP2 inhibition diminishes $KRAS^{G12C}$ cycling and promotes tumor microenvironment remodeling. *J. Exp. Med.* **218**, e20201414 (2021).
88. Chaheine, C. M., Tang, J., Conway, L. P. & Parker, C. G. Fully-functionalized natural product probes to expand the chemical tractability of the human proteome. *Angew. Chem. Int. Ed.* **64**, e202502648 (2025).
89. Kim, A. S. et al. Integrated phenotypic screening and chemical proteomics identifies ETF1 ligands that modulate viral translation and replication. Preprint at *bioRxiv* https://doi.org/10.1101/2025.08.27.672717 (2025).

**Publisher's note** Springer Nature remains neutral with regard to jurisdictional claims in published maps and institutional affiliations.

**Open Access** This article is licensed under a Creative Commons Attribution-NonCommercial-NoDerivatives 4.0 International License, which permits any non-commercial use, sharing, distribution and reproduction in any medium or format, as long as you give appropriate credit to the original author(s) and the source, provide a link to the Creative Commons licence, and indicate if you modified the licensed material. You do not have permission under this licence to share adapted material derived from this article or parts of it. The images or other third party material in this article are included in the article's Creative Commons licence, unless indicated otherwise in a credit line to the material. If material is not included in the article's Creative Commons licence and your intended use is not permitted by statutory regulation or exceeds the permitted use, you will need to obtain permission directly from the copyright holder. To view a copy of this licence, visit http://creativecommons.org/licenses/by-nc-nd/4.0/.

© The Author(s) 2026

## Methods

### Cell culture and treatment

MDA-MB-231 (HTB-26), HEK293T (CRL-3216), H460 (HTB-177), MIA PaCa2 (CRL-1420) and H1975 (CRL-5908) cell lines were procured from the American Type Culture Collection; HCC44 (ACC 534) cells were obtained from DSMZ; and Lenti-X 293 T (LX293T and 632180) cells were obtained from Takara Bio. MDA-MB-231, MIA PaCa2, HEK293T and Lenti-X 293T cells were cultured in DMEM supplemented with 10% (v/v) FBS and 2 mM L-glutamine. HCC44, H1975 and H460 cells were maintained in RPMI 1640 medium supplemented with 10% (v/v) FBS and 2 mM L-glutamine. All cell lines were incubated at 37 °C in a humidified atmosphere containing 5% $CO_2$. Unless otherwise indicated, all compound treatment experiments were performed when cells are around 50–70% confluency.

### Chemical probes and materials

The chemical probes and acid-cleavable biotin-azide used in this study were synthesized in-house based on previously reported research from our laboratory[20,24,90]. The structural identity of these resynthesized compounds was verified by $^{1}H$ and $^{13}C$ nuclear magnetic resonance (NMR) spectroscopy alongside high-resolution MS. Purity of synthesized compounds was determined to be greater than 95% by analytical high-performance liquid chromatography (HPLC) using ultraviolet detection at 254 nm and $^{1}H$ NMR.

Commonly used reagents were purchased from Corning, Gibco, Bio-Rad, Research Product International, Sigma-Aldrich and Thermo Fisher Scientific. Biotin-PEG3-Azide (AZ104) was from Click Chemistry Tools. Sequencing-grade modified trypsin (V5111) was purchased from Promega. Endoproteinase LysC (P8109S) is from New England Biolabs. Pierce Streptavidin Agarose (cat. no. 20353), Pierce High pH Reversed-Phase Fractionation Kit (84868), TMT10plex Isobaric Label Reagent Set (90406), TMTpro 16plex Label Reagent Set (A44520) and Halt protease and phosphatase inhibitors (78438 or 78441) were from Thermo Fisher Scientific. Specific chemical reagents originated from the following sources without further purification: STR (Selleck Chemicals, S1421); ALW-II-41-27 (HY-18007), BI-2493 (HY-153723), BI-2865 (HY-153724), AMG-510 (HY-114277), MRTX-849 (HY-130149), RMC-7977 (HY-156498), SHP-099 (HY-100388) and dasatinib (HY-10181), all from MedChemExpress; Tuni (Merck, T7765); and cholesterol (Avanti Research, 700100). All purchased compounds have greater than 98% purity, as reported by the vendors.

### Plasmids and transient transfection

The full-length codon-optimized human NPC2 (including wild-type, N58A or N135A mutation) and human GABARAPL2 (wild-type and S87/88A) were synthesized (Twist Bioscience) and cloned into a pTWIST-CMV-puro vector individually. The full-length codon-optimized human TNFRSF10B–Flag was synthesized (GenScript) and cloned into a pcDNA3.1 vector individually. pBabe–HA–KRAS (75282), pRK5–p14–Flag (42330) and pRK5F–TACE (31713) were obtained from Addgene. Site-directed mutagenesis was generated by Phusion Flash High-Fidelity PCR (Thermo Fisher Scientific, F548S) and ligated by In-Fusion Snap Assembly (Takara Bio, 638947). All plasmids were verified by Sanger or whole-plasmid sequencing.

For transient transfection, LX293T cells were seeded and transfected by Lipofectamine 3000 Transfection Reagent (Invitrogen, L3000075). Cells were harvested at 24 hours or 48 hours after transfection for subsequent analysis.

### Proliferation assay

Cells were plated at 20,000 cells per well in 96-well plates. The media were first aspirated after the cells were attached, and the cells were then treated in triplicate with media containing different concentrations of STR (24 nM–50 μM) for MDA-MB-231 cells and Tuni (1–100 μg $ml^{-1}$) for HEK293T cells. The same volume of DMSO was used as a vehicle control. Cell proliferation was assayed using the CellTiter-Glo Luminescent Cell Viability Assay (Promega) following the manufacturer's guidelines. Data represent the average and standard deviation of triplicates in measured luminescence.

### Photoaffinity probe cell treatments

For MDA-MB-231 cells, cells were cultured to approximately 90% confluency in 15-cm plates, pretreated with STR for 3 hours. For HEK293T cells, cells grew to about 70% confluency and were then treated with Tuni for 24 hours. After aspirating the growth medium, the cells were incubated in serum-free medium containing FFF probes (20 μM for in-gel labeling, 100 μM for proteomics, site of labeling (SoL) and gel-based validations) for 30 minutes at 37 °C in a 5% $CO_2$ atmosphere. After treatment, the cells were exposed to ultraviolet light (365 nm) for 20 minutes, harvested, washed with cold DPBS and transferred to tubes. The cell suspensions were then centrifuged (400*g*, 5 minutes) and washed with cold DPBS, and the resulting pellets were stored at −80 °C until further processing.

### Gel-based fluorescence analysis

Gel-based analysis of probe cross-linked proteins was performed as previously described[90]. In brief, 6 μl of a freshly prepared click reaction mixture was added to each 50-μl protein sample (2 mg $ml^{-1}$). The click mix included 3 μl of 1.7 mM tris((1-benzyl-1H-1,2,3-triazol-4-yl)methyl) amine (TBTA) in 4:1 *t*-BuOH:DMSO; 1 μl of 50 mM $CuSO_4$ in water; 1 μl of 1.25 mM tetramethylrhodamine (TAMRA) azide in DMSO; and 1 μl of freshly prepared 50 mM tris(2-carboxyethyl)phosphine (TCEP) in DPBS. Samples were mixed with the click mix and incubated at room temperature for 1 hour. Reactions were then quenched with 17 μl of 4× SDS sample buffer. Proteins (15 μg per lane) were resolved by SDS-PAGE using in-house prepared 10% acrylamide gels and visualized via in-gel fluorescence with a ChemiDoc Imaging System (Bio-Rad). Images were processed using Image Lab software (Bio-Rad).

### Preparation of samples for proteomic analysis

For unenriched proteomic samples, cell pellets were resuspended in 100 μl of ice-cold DPBS containing 1× protease inhibitor cocktail (Thermo Fisher Scientific, 78441) and lysed by probe sonication (Branson Sonifier; 15 ms on, 40 ms off, 15% amplitude, seven pulses). Protein concentrations were measured using the BCA assay (Thermo Fisher Scientific). Then, 100–200 μg of protein was denatured in 8 M urea, reduced with 5 mM dithiothreitol (DTT) and alkylated with 55 mM iodoacetamide (IAA). Proteins were precipitated with 4:1 methanol:chloroform, washed and resuspended in 100 mM TEAB. Sequential digestion was performed using LysC (New England Biolabs, P8109S) for 2 hours, followed by trypsin (Promega, V5111) overnight at 37 °C in the presence of 1 mM $CaCl_2$. Peptides were quantified using the Pierce Quantitative Fluorometric Peptide Assay (Thermo Fisher Scientific) and labeled with TMT10plex reagents (Thermo Fisher Scientific) in 30% acetonitrile. Labeling was quenched with 6 μl of 5% hydroxylamine (v/v), followed by a 15-minute incubation. Samples were acidified with 8 μl of formic acid, dried and resuspended in 0.1% trifluoroacetic acid (TFA). Fractionation was carried out using the Pierce High pH Reversed-Phase Fractionation Kit (Thermo Fisher Scientific, 84868). MDA-MB-231 peptides were divided into 18 fractions and pooled into nine sets; HEK293T peptides were divided into 28 fractions and pooled into 14 sets. All fractions were dried and stored at −80 °C until liquid chromatography–mass spectrometry (LC–MS) analysis.

For phosphoproteomic samples, MDA-MB-231 cells were treated with 0.25 μM STR for 3 hours prior to harvest. Cell pellets were lysed in 1 ml of ice-cold DPBS containing protease and phosphatase inhibitors (Thermo Fisher Scientific, 78441) and sonicated. Proteins were denatured with 4 M urea, reduced (DTT, 5 mM), alkylated (IAA, 55 mM) and precipitated. Pellets were resuspended in 1 M urea in 50 mM HEPES (pH 8.5), digested with LysC and then trypsin and desalted using

Sep-Pak C18 cartridges. Approximately 2 mg of peptides per sample was enriched using $TiO_2$ beads (GL Sciences, 5010-21315) or Fe-NTA beads (Thermo Fisher Scientific, A32992), following manufacturer protocols. For $TiO_2$ enrichment, peptides were resuspended in 2 M lactic acid and 50% acetonitrile and incubated with beads at a 1:4 peptide:bead ratio for 1 hour at room temperature with vortexing. Beads were washed three times with binding buffer and three times with wash buffer (50% acetonitrile, 0.1% TFA). Phosphopeptides were eluted with 50 mM potassium phosphate (pH 10) and desalted using Sep-Pak C18 cartridges. The eluates from the $TiO_2$ or Fe-NTA enrichment were dried in a vacuum centrifuge and then labeled with TMT10plex reagents (Thermo Fisher Scientific) for 1 hour at room temperature, quenched, acidified and dried. Then, peptides were resuspended in 0.1% TFA, pooled and fractionated using the Pierce High pH Reversed-Phase Fractionation Kit into 18 fractions (7.5–95% acetonitrile), which were pooled into nine final sets, dried and stored at −80 °C.

KRAS phosphoproteomics sample preparation was performed using the S-Trap micro spin column protocol. In brief, 5 µg of purified KRAS protein was solubilized in 130 µl of buffer containing 50 mM TEAB (pH 7.5) and 5% SDS. Proteins were reduced with 5 mM DTT at 56 °C for 30 minutes and subsequently alkylated with 50 mM IAA for 30 minutes in dark. The sample was acidified with 15 µl of 12% phosphoric acid, followed by the addition of 900 µl of S-Trap binding buffer (90% methanol, 100 mM TEAB (pH 7.1)). The mixture was loaded onto an S-Trap micro spin column and centrifuged at 10,000*g* for 30 seconds. The column was washed three times with 225 µl of S-Trap binding buffer. For digestion, 5 µg of trypsin reconstituted in 100 mM TEAB (pH 8.5) was added to the column and incubated overnight at 37 °C. Peptides were eluted sequentially with 40 µl of 50 mM TEAB (pH 8.0), 40 µl of 0.2% formic acid and 40 µl of 50% acetonitrile/0.2% formic acid. Elutions were collected by centrifugation at 4,000*g* for 1 minute. The combined eluates were dried using a vacuum concentrator prior to analysis.

Chemoproteomic samples were prepared in biological duplicates for each condition using previously described procedures[91]. In brief, cell pellets were resuspended in 500 µl of cold DPBS and lysed via sonication. Protein concentrations were normalized to 2 mg $ml^{-1}$ in 500 µl of ice-cold DPBS, using a DC Protein Assay (Bio-Rad), in 15-ml Falcon tubes. The 'click chemistry cocktail' was then added to each lysate, consisting of TBTA (final concentration: 100 µM), TCEP (final concentration: 1 mM), biotin-azide (final concentration: 100 µM) and $CuSO_4$ (final concentration: 1 mM). Samples were incubated at room temperature for 1 hour. Ice-cold 4:1 MeOH:$CHCl_3$ (2.5 ml) and ice-cold DPBS (1 ml) were added to each sample to quench the click reaction, followed by centrifugation (3,200*g*, 4 °C, 10 minutes) to precipitate proteins. The precipitates were washed with 4:1 MeOH:$CHCl_3$ and resuspended in 500 µl of 6 M urea in DPBS, along with 10 µl of 10% SDS. Protein reduction was performed by adding 50 µl of a freshly prepared 1:1 solution of TCEP (25 µl, 200 mM in DPBS) and $K_2CO_3$ (25 µl, 600 mM in DPBS) and incubated at 37 °C for 30 minutes. After reduction, proteins were alkylated by adding 70 µl of freshly prepared IAA (400 mM in DPBS) and incubated for 30 minutes at room temperature in dark. After alkylation, 130 µl of 10% SDS was added to the samples, followed by dilution with 5.5 ml of DPBS. A 100-µl aliquot of 50% streptavidin agarose slurry (Thermo Fisher Scientific, 20349) was added to each tube, and samples were rotated for approximately 1.5 hours at room temperature to enrich probe-labeled proteins. The beads were then centrifuged down to tube bottom (750*g*, 2 minutes, 4 °C) and washed once with 0.2% SDS in DPBS (5 minutes), twice with DPBS and once with water and transferred to LoBind microcentrifuge tubes with 100 mM TEAB (pH 8.5).

Bound proteins were digested overnight with trypsin (Promega, V5111) in digestion buffer (100 ml, 100 mM TEAB (pH 8.5) and 100 µM $CaCl_2$) at 37 °C. The resulting peptides were transferred to new tubes for each condition and labeled with the respective TMT (Thermo Fisher Scientific) 10plex or 16plex reagents (8 µl, 20 µg $µl^{-1}$) for 1 hour, quenched, acidified and dried through a SpeedVac vacuum concentrator. The dried peptides were redissolved in 0.1% TFA in water, combined and fractionated into 12 fractions by Pierce High pH Reversed-Phase Fractionation Kit. The fractions were pooled pairwise into six final fractions, dried and stored at −80 °C until MS analysis.

The preparation of SoL samples followed our previously reported protocol[21]. In brief, cell pellets were resuspended in cold DPBS (1,000 µl) and lysed via sonication. Then, 3 mg of the lysates was taken and diluted into 1 ml of DPBS in 15-ml Falcon tubes. Each sample was then added with TBTA (final concentration: 100 µM), TCEP (final concentration: 1 mM), cleavable biotin-azide tag (light L-valine tag, final concentration: 100 µM) and $CuSO_4$ (final concentration: 1 mM) for 1 hour. Cold methanol (4 ml) was added, and the protein was allowed to precipitate overnight. The precipitated proteins were pelleted by centrifugation (4,000*g*, 10 minutes), and the supernatant was discarded. The pellets were washed with 4:1 (v/v) MeOH:$CHCl_3$, resuspended by sonication and centrifuged again (4,000*g*, 10 minutes). The pellets were then resuspended in freshly prepared 6 M urea solution (1,000 µl, in DPBS) and a solution of SDS (100 µl, 10% w/v), followed by reduction and alkylation steps as described above. The samples were diluted with DPBS (11 ml); streptavidin-agarose slurry (200 µl, 50%, Pierce) was added; and the tubes were rotated for 1.5 hours at room temperature. The beads were pelleted by centrifugation (500*g*, 5 minutes) and washed with 0.2% SDS in DPBS (1×), DPBS (2×), water (1×) and 100 mM TEAB (2 × 5 ml (pH 8.5) in water). The beads were then transferred to 1.5-ml LoBind microcentrifuge tubes, added with sequencing-grade modified trypsin (4 µg, 100 mM TEAB (pH 8.5), 100 µM $CaCl_2$) and incubated overnight at 37 °C. The beads were further washed with SDS in DPBS once (0.2% w/v), NaCl in DPBS (2×, 150 mM) and water (2×) by centrifugation (400*g*, 5 minutes). Elution was performed with a buffer of formic acid/water (3% v/v, 200 µl) for 1 hour with gentle shaking. The supernatant was collected, and the beads were re-eluted with the same buffer, followed by an additional elution with acetonitrile/water (50% v/v, with 3% formic acid, 200 µl). The supernatants were combined and dried using vacuum centrifugation. The resulting residue was reconstituted in TEAB (100 mM) and labeled with TMT reagents (Thermo Fisher Scientific) across replicates as per the manufacturer's instructions. TMT-labeled samples were pooled, dried, fractionated into 12 fractions by Pierce High pH Reversed-Phase Fractionation Kit, combined into six final fractions, dried and stored at −80 °C until MS analysis.

### LC–MS analysis of proteomic samples

LC–MS analysis was conducted following our previously published protocol[21]. For phosphor, unenriched and enriched proteomics, samples were resuspended in MS sample buffer (20 µl, 5% acetonitrile, 0.1% formic acid in water) prior to LC–MS analysis, following published methods[91]. In short, 3 µl of each sample was loaded onto an Acclaim PepMap 100 precolumn (75 µm × 2 mm) and separated on a PepMap RSLC analytical column (2 µm, 100 Å, 75 µm × 25 cm) using an UltiMate 3000 RSLCnano system (Thermo Fisher Scientific). Buffer A (0.1% formic acid in water) and buffer B (0.1% formic acid in acetonitrile) were used in a 220-minute gradient at a flow rate of 300 nl $min^{-1}$. The gradient consisted of 2% buffer B for the first 10 minutes, a gradual increase to 30% buffer B over the next 192 minutes, 60% buffer B for 5 minutes, followed by a ramp to 95% buffer B in 1 minute, hold for 5 minutes, then back to 2% buffer B in 1 minute and re-equilibrated for 6 minutes.

Eluents were analyzed using an Orbitrap Fusion Lumos mass spectrometer (Thermo Fisher Scientific) with a 3-second cycle time and a nano-LC electrospray ionization voltage of 2,000 V. Data were acquired with Xcalibur software (version 4.1.50). MS1 spectra were captured with a scan range of 375–1,500 $m/z$, a maximum injection time of 50 ms and dynamic exclusion enabled (one repeat, exclusion duration of 20 seconds). The resolution was set to 120,000 with an automatic gain control (AGC) target of $1 \times 10^6$. Peptides chosen for MS2 analysis were

fragmented by collision-induced dissociation (CID) at 30% collision energy at 1.6-$m/z$ isolation window. Fragment ions were recorded in the ion trap (AGC target $1.8 \times 10^4$, maximum injection time of 120 ms). MS3 spectra were generated using high-energy collision dissociation (HCD) mode with 65% collision energy, and synchronous precursor selection (SPS) was set as 10.

For SoL proteomics, samples were resuspended in 30 µl of MS sample buffer, and 10 µl was injected onto the analytical column. The loading phase involved 2% buffer B (0.1% formic acid in acetonitrile) for 10 minutes, followed by elution with a gradient of 2–35% buffer B over 215 minutes, 35–55% over 10 minutes, 55–95% over 5 minutes, 95% buffer B for 2 minutes and then decreasing to 2% buffer B over 1 minute. After holding at 2% for 2 minutes, the gradient was ramped to 95% buffer B in 1 minute, held at 95% for 2 minutes, decreased again to 2% in 1 minute and held at 2% for an additional 11 minutes, totaling 260 minutes of run time.

Eluents were analyzed using an Orbitrap Fusion Lumos mass spectrometer (Thermo Fisher Scientific). MS1 scans were performed with a resolution of 120,000, a scan range of 375–2,000 $m/z$ and an RF lens setting of 60%, with a dynamic exclusion window of 30 seconds. MS2 scans used the Orbitrap mass analyzer with a resolution of 15,000 and a first mass of 120. Peptide isolation and fragmentation were carried out with quadrupole isolation of 1.6 $m/z$, an AGC target of $5 \times 10^4$, a maximum injection time of 110 ms and an HCD energy of 28%. For MS3, the Orbitrap mass analyzer was set to a resolution of 50,000 with an AGC target of $1.5 \times 10^5$, a maximum injection time of 120 ms and an HCD collision energy of 65% (SPS 10).

### Proteomic result analysis

Proteomic analysis was carried out using Proteome Discoverer (version 3.0, Thermo Fisher Scientific) following previously established protocols[91]. For phosphor, unenriched and enriched proteomic results, peptide identification was conducted using the SEQUEST HT algorithm; precursor mass tolerance is 10 ppm; and fragment mass tolerances is 0.6 Da, allowing for two missed cleavage sites. Variable modifications included oxidation (methionine, +15.994915) and carbamidomethyl (cysteine, +57.02146), and TMT modifications (lysine and N-terminal, +229.1629 for 10plex, +304.207 for 16plex tags) were used as fixed modifications. The spectral data were searched against the *Homo sapiens* proteome database (UniProt 2018; 42,358 sequences), applying a 1% false discovery rate (FDR) with Percolator. MS3 peptide quantification was performed using a mass tolerance of 20 ppm.

For unenriched proteomic analysis, abundances in each channel were normalized to the average of the median signal intensity across all channels. For phosphoproteomic analysis, no normalization was applied to peptide abundances. For enriched proteomic results, abundances in each channel were normalized to endogenously biotinylated proteins (PCCA, PC, MCCC1 or ACACA). For phospho-dependent experiments P2 and P6, no normalization was applied to protein abundances.

SoL analysis was conducted according to the previously published protocol[21], using Proteome Discoverer (version 3.0, Thermo Fisher Scientific) for data processing. Peptide sequences were identified by comparing experimental fragmentation patterns with proteome databases via the SEQUEST HT algorithm. The precursor mass tolerance was set to 10 ppm; fragment mass tolerance was set to 0.05 Da; and up to two missed cleavage sites were allowed. Static modifications included TMT at the N terminus (+229.163), and variable modifications specified were carbamidomethyl (cysteine, +57.02146), oxidation (methionine, +15.994915), TMT tag (lysine and N-terminal, +229.1629 for 10plex, +304.207 for 16plex tags) and FFF tags (P2: +481.310; P3: +501.274; P4: +467.217; P5: +517.305; P6: +453.274) on all amino acids. The spectral data were searched against each probe's enrichment database from the whole protein profiling experiment with a 0.01 FDR using the target–decoy approach. Further validation was performed using Percolator, applying the target–decoy strategy with a 'Separate' setting and a maximum $\Delta C_n$ threshold of 0.1. TMT quantification was carried out at the MS3 level, with a tolerance of 20 ppm. Only peptides with an average signal-to-noise ratio greater than 10 were retained for further analysis.

For MSFragger SoL searches, an open search workflow was used[92]. In brief, precursor mass tolerance was set to 0–520 Da, and MS1 tolerance was set to 20 ppm. Full trypsin specificity was designated with a maximum of two missed cleavages. Peptide length was set from 4 to 50; peptide mass range was set from 500 to 5,000. Oxidation (methionine, +15.9949), carbamidomethyl (cysteine, +57.02146) and TMT tag (lysine, +229.1629 for 10plex, +304.207 for 16plex tags) were used as variable modifications, and TMT tags (N-terminal, +229.1629 for 10plex, +304.207 for 16plex tags) were used as fixed modifications.

To ensure data reliability, proteins reported required at least two unique peptides. TMT ratios calculated in Proteome Discoverer were transformed using $\log_2(x)$, and statistical significance of the ratios was assessed with two-tailed Student's $t$-tests across two biological replicates (significance threshold set at $P < 0.05$). Detailed proteomics data are available in Supplementary Tables 1–15.

### Gel-based analysis of probe cross-linked targets in cells

Cells were treated as described in the 'Photoaffinity probe cell treatments' section. Probe-labeled cell pellets were lysed in ice-cold DPBS supplemented with 1× Halt protease inhibitor cocktail (Thermo Fisher Scientific, 78438) and lysed by sonication. Protein concentrations were normalized and click reactions were performed as described in the chemoproteomic part in the 'Preparation of samples for proteomic analysis' section. In brief, after the 'click chemistry' reaction, 2 ml of ice-cold MeOH was added to each sample to precipitate proteins and incubated overnight at −20 °C. The samples were then centrifuged (3,200$g$, 4 °C, 10 minutes) and washed with 4:1 MeOH:$CHCl_3$, resuspended by sonication and centrifuged as above. Pellets were resuspended in freshly prepared urea solution (500 µl of DPBS, 6 M) with SDS (100 µl of 10% w/v). After incubating the samples for 30 minutes at 37 °C to fully dissolve the protein pellet, samples were diluted with DPBS (5.5 ml), added with a streptavidin-agarose slurry (100 µl, 50%, Pierce) and rotated for 1.5 hours at room temperature. The beads were pelleted by centrifugation (500$g$, 5 minutes, 4 °C) and washed once with DPBS with 0.2% SDS, washed three times with DPBS and then boiled with 2× SDS sample buffer for 15 minutes. Boiled samples and saved input samples were resolved by SDS-PAGE and followed by immunoblotting analysis.

### Knowledge-based and structure-based enrichment analyses

Protein enrichment analysis was conducted and modified following an established protein enrichment clustering workflow[23]. In brief, enriched proteins were analyzed and clustered based on protein classifications (PANTHER database 19.0 and UniProt 'Family and domain databases')[93]. Significant and emerging significant hits were identified based on ligandability changes. Proteins were visualized in clusters reflecting functional and classification similarities. Downstream analyses included Gene Ontology term and Illuminating the Druggable Genome (IDG) category enrichment, using PANTHER family annotations and IDG database annotations, respectively. Clustering and plotting were performed using Python scripts adapted from previously published work[23].

Protein information for the labeled peptides was used to extract additional information from UniProt, such as structural features (ACT_SITE, BINDING, METAL, DNA_BIND and NP_BIND), presence in DrugBank, Gene Ontology keywords and PDB and AlphaFold structure identities. Protein structures were batch downloaded from PDB or AlphaFold using command line prompts in terminal. Proteomic, pocket, site and structure data were processed together using R scripts adapted from previously published work[21].

### Immunostaining

For NPC2 localization, HEK293T cells were seeded on 0.02% poly-L-lysine (Sigma-Aldrich, P1274)-coated eight-well plates (ibidi, 80827) at 37 °C overnight. Cells were treated with Tuni for another 24 hours, fixed in Bouin's solution (Sigma-Aldrich) for 10 minutes and permeabilized with ice-cold methanol at −20 °C for 10 minutes. After fixation/permeabilization, cells were washed for 5 minutes with PBS and then blocked with 3% BSA/PBST (PBS with 0.05% Triton X-100) for 10 minutes. Primary antibodies were diluted with blocking buffer (rabbit anti-NPC2 1:100 and mouse anti-LAMP1 1:500) and incubated with cells for 1 hour. After three washes with PBST, cells were incubated with Alexa Fluor-labeled secondary antibodies (1:500) for an additional hour. Cells were then washed three times with PBST and stained with NucBlue probe (Thermo Fisher Scientific, R37606) for nuclear imaging. Confocal images were carried out on a Zeiss LSM 780 microscope using a ×100 objective (numerical aperture = 1.40), and 1 Airy unit was set as a pinhole for each channel. Imaris, ImageJ and ZEN (Zeiss) software were used for image processing and analysis.

### Thermostability experiments

MDA-MB-231 cells were digested with 0.25% trypsin, and equal amounts of cells were incubated with DMSO, BI-2865 (10 nM) or 6-aminocoumarin (100 µM) with or without STR/SHP-099/dasatinib in fresh DMEM media for 30 minutes at 37 °C. Cells were then collected and washed once with binding buffer (cold DPBS containing DMSO or the indicated concentration of inhibitors and 1× Halt protease inhibitor cocktail). Cells were then resuspended in binding buffer, counted and aliquoted to a concentration of 300,000 cells per 50 µl before being transferred to polymerase chain reaction (PCR) tubes for heat treatment. PCR tubes were heated at the indicated temperature gradient on a thermal cycler (Bio-Rad) for 3 minutes, followed by incubation at 25 °C for 3 minutes. After three snap freeze–thaw cycles with liquid nitrogen, lysates were transferred to 1.5-ml Eppendorf tubes and centrifuged at 100,000*g* for 20 minutes at 4 °C to separate destabilized proteins from proteins remaining in solution. The resulting supernatant was transferred to new Eppendorf tubes, mixed with 4× SDS sample buffer, boiled for 5 minutes and processed for immunoblotting as described below.

### RAS-binding domain pull-down assay

RAS-binding domain (RBD) experiments were performed using the Active Ras Pull-Down and Detection Kit (Thermo Fisher Scientific, 16117) following the manufacturer's instructions. In brief, after compound treatment for the specified duration, cells were washed with ice-cold PBS, harvested, snap frozen in liquid nitrogen and stored at −80 °C until use. Cells were lysed in lysis buffer, vortexed and incubated on ice for 15 minutes. The lysates were then centrifuged at 14,000*g* for 15 minutes at 4 °C, and supernatants were collected. Cell lysates were incubated with Raf-GST and GST beads at 4 °C for 1.5 hours with rotation, washed three times with lysis buffer and eluted by incubating in 2× sample buffer for 15 minutes. All samples were resolved by SDS-PAGE and processed for immunoblotting as described below.

### Immunoprecipitation and immunoblotting

For immunoblotting, cells were treated with indicated compounds for specified time and then washed with ice-cold PBS and lysed in NP-40 buffer (10 mM Tris-HCl, 150 mM NaCl, 1 mM EDTA and 1% (w/v) NP-40) supplemented with protease and phosphatase inhibitors. After centrifuging at 14,000*g* for 10 minutes at 4 °C to remove cell debris, supernatants were taken, and protein concentrations were determined by a DC Protein Assay (Bio-Rad, 5000112). Equal amounts of protein lysates were mixed with the 4× SDS sample buffer and resolved by SDS-PAGE.

For LAMTOR2–Flag immunoprecipitation, cells were resuspended in E1C buffer (50 mM HEPES, 250 mM NaCl, 5 mM EDTA and 0.3% (w/v) CHAPS supplemented with protease inhibitor) and sonicated three times. Lysates were cleared by centrifugation and normalized to 1.5–2.0 mg ml$^{-1}$. Then, 1 µg of anti-Flag antibody was added to supernatants and rotated overnight at 4 °C and incubated with 20 µl of protein A/G agarose beads (MedChemExpress) for an additional hour on the next day. The beads were washed three times with the E1C buffer and eluted by incubating in 2× sample buffer at 95 °C for 10 minutes and resolved by SDS-PAGE.

For TACE–Flag immunoprecipitation, cells were resuspended in 1% NP-40 buffer supplemented with protease inhibitor. Lysates were cleared by centrifugation and normalized to 1.5–2.0 mg ml$^{-1}$. Then, 1 µg of anti-Flag antibody was added to supernatants and rotated overnight at 4 °C and incubated with 20 µl of protein A/G agarose beads (MedChemExpress) for an additional hour on the next day. The beads were washed three times with the E1C buffer and eluted by incubating in 2× sample buffer at 95 °C for 10 minutes and resolved by SDS-PAGE.

For HA–KRAS immunoprecipitation, after compound treatment for the designated time, cells were washed twice with ice-cold PBS and lysed in NP-40 buffer supplemented with protease and phosphatase inhibitors. Lysates were then cleared by centrifugation, normalized and incubated with 20 µl of anti-HA magnetic beads at 4 °C for 3 hours or overnight with rotation. The beads were washed three times with lysis buffer and eluted with 2× sample buffer.

Resolved proteins were transferred to PVDF membranes using the Trans-Blot Turbo Transfer system (Bio-Rad). Membranes were blocked with 5% non-fat milk or 3% BSA in TBST and incubated overnight with primary antibodies. Blots were washed three times with TBST and incubated with secondary antibodies for 1 hour. Membrane visualization was performed using the ChemiDoc Imaging System (Bio-Rad), and band density was quantified with Image Lab software (version 6.1.0).

### KRAS production and purification

The His6-MBP-TEV-Avi-Hs.KRAS$^{G12C}$ plasmid was transformed into *Escherichia coli* BL21(DE3) cells. Cultures were grown at 37 °C to an optical density at 600 nm ($OD_{600}$) ≈ 0.6, and then 0.5 mM IPTG was added. The culture was continued for 20 hours at 18 °C. Cells were harvested by centrifugation, resuspended in lysis buffer (100 mM HEPES (pH 7.4), 500 mM NaCl and 25 mM imidazole) and lysed via sonication. The recombinant protein was purified using Ni-NTA affinity chromatography. After purification, the fusion protein was dialyzed using a PD-10 desalting column (GE Healthcare, 17085101). The His6-MBP tag was cleaved by incubation with HQ-TEV protease (ProTEV Plus; Promega) for 1 hour at room temperature. Both the cleaved His6-MBP tag and the protease were removed by passing the mixture through Ni-NTA spin columns (NEBExpress, S1427L).

KRAS was biotinylated using a commercial biotinylation kit (Avidity LLC). In brief, 3.2 mg (approximately 137 nmol) of MBP-cleaved KRAS in 4 ml of assay buffer (100 mM HEPES and 150 mM NaCl (pH 7.4)) was treated with 500 µl of Biomix A, 500 µl of Biomix B and 13.8 µg of BirA. The final reaction conditions included 10 mM ATP, 10 mM $MgOAc_2$, 50 µM biotin and 27 µM KRAS. The mixture was incubated for 3 hours at room temperature and subsequently buffer exchanged twice with assay buffer via a PD-10 desalting column.

To generate fluorescently labeled KRAS for binding assays, the purified protein was loaded with BODIPY-GDP (Invitrogen, G22360) as described previously[94]. KRAS protein was diluted to 2 µM in EDTA buffer (20 mM HEPES (pH 7.5), 50 mM NaCl, 10 mM EDTA and 0.01% Tween 20) and incubated at room temperature for 1 hour to strip native nucleotides. This mixture was then diluted to 90 nM in assay buffer (20 mM HEPES (pH 7.5), 150 mM NaCl, 10 mM $MgCl_2$ and 0.005% Tween 20) containing 900 nM BODIPY-GDP (Invitrogen, G22360) and incubated at 4 °C for overnight. Excess BODIPY-GDP was removed using a PD-10 column, and the protein was concentrated via ultracentrifugation.

### In vitro kinase assay of KRAS

In vitro phosphorylation of purified recombinant human KRAS$^{G12C}$ was carried out following a previously reported procedure[56]. KRAS

(450 µg) was incubated with 6.8 µg of active human Src (Sigma-Aldrich, 14-326) and ATP (3 mM) in 600 µl of kinase buffer (50 mM HEPES (pH 7.5), 10 mM $MgCl_2$, 1 mM EGTA and 0.01% Brij-35) for overnight at room temperature.

### Ion exchange chromatography (HPLC)

The un-phosphorylated, mono-phosphorylated and di-phosphorylated forms of KRAS were separated by anion exchange chromatography using a WAX-10 column (Thermo Fisher Scientific) with mobile phases consisting of buffer A (20 mM HEPES (pH 7.0), 5 mM $MgCl_2$ and 1 mM TCEP) and buffer B (20 mM HEPES (pH 7.0), 5 mM $MgCl_2$, 1 mM TCEP and 1 M NaCl), both supplemented with phosphatase inhibitors (1 mM activated sodium vanadate, 2 mM imidazole and 1 mM sodium fluoride) to stabilize the phosphorylated forms[56]. Separation was performed at a flow rate of 1 ml $min^{-1}$ with a gradient of 0–5% B (0–20 minutes), 5–18% B (20–70 minutes), 18–80% B (70–72 minutes) and 80–100% B (72–80 minutes). Isolated KRAS fractions were concentrated via ultracentrifugation, desalted using a Zeba micro spin desalting column (Thermo Fisher Scientific, 89877) and characterized by Phos-tag gel electrophoresis and phosphoproteomics.

### SPR

Binding of BI-2865 to different phosphorylation forms of KRAS was evaluated by SPR (Cytiva, Biacore S200). In brief, biotinylated KRAS constructs were diluted to 0.3 µM in immobilization buffer (1× HBS-P+ containing 100 nM BODIPY-GDP and 1 mM $MgCl_2$) and injected over a streptavidin sensor chip surface until the target immobilization levels (4,000–4,500 resonance units) were reached. Flow cells were subsequently quenched with three 60-second injections of 50 µM biotin-PEG at 10 µl $min^{-1}$. Binding experiments were conducted in running buffer consisting of 1× HBS-P+ supplemented with 100 nM GDP, 1 mM $MgCl_2$, 2% DMSO and an inhibitor cocktail (0.5 mM activated sodium vanadate, 1 mM imidazole, 1 mM sodium fluoride and 1 mM sodium molybdate). BI-2865 doses were injected over all three protein channels, as well as a reference surface, simultaneously. Resulting sensorgrams were reference subtracted, blank subtracted and subsequently analyzed using Biacore Evaluation Software to determine kinetic parameters from 1:1 binding model fits.

### Nucleotide exchange assay

BODIPY-GDP preloaded KRAS proteins were diluted to 1 µM in reaction buffer (50 mM HEPES (pH 7.4), 150 mM NaCl and 2.5 mM $MgCl_2$) containing 10 µM GTP and SOS1 (BPS Bioscience, 101573). All assays were performed in 384-well plates. Condition screening was conducted in duplicate using un-phosphorylated KRAS with SOS1 concentrations ranging from 2 nM to 500 nM, whereas quantitative kinetic analysis was performed in triplicate on un-phosphorylated, mono-phosphorylated and di-phosphorylated forms using 100 nM SOS1. Positive controls (containing 1 mM EDTA in the absence of SOS1) and negative controls (without both SOS1 and GTP) were included for each KRAS variant. Fluorescence was monitored using a fluorescence microplate reader with excitation at 470 nm and emission at 525 nm over time (0–220 minutes for condition screening; 0–60 minutes for quantitative kinetic analysis). Final data were normalized by setting the negative control value at 0 minutes as 100% and the positive control value at the final timepoint (220 minutes for screening; 60 minutes for kinetic analysis) as 0%.

### Modeling and docking

Three-dimensional coordinates of the probes were generated from SMILES using the RDKit's ETKDG version 3 followed by universal force field (UFF) energy minimization. Target protein structures were obtained from the PDB when available; otherwise, AlphaFold2-predicted models were used. In cases where multiple PDB structures existed, the most suitable was selected based on the presence of the SoL residue coordinates, highest sequence coverage and best resolution, with a preference for X-ray crystallography over cryogenic electron microscopy. In some specific cases, the structures were manually selected. These cases include $KRAS^{G13D}$ and $KRAS^{G12C}$ (PDB: 8B00 and 8AZV, respectively) and EphA2 (PDB: 5EK7). Hydrogen atoms were added using Reduce, and both ligands and receptors were prepared according to the standard AutoDock protocol[95]. Druggable pockets were identified using fpocket, and a docking grid box was defined for each, encompassing the pocket region with a minimum side length of 24 Å. All probes were docked into each predicted pocket using AutoDock-GPU[96], employing default parameters for the Lamarckian Genetic Algorithm and ADADELTA local search to generate 50 poses per ligand. Pockets were ranked based on the best binding energy, and the proximity (<6 Å) of the diazirine moiety to any proteomics-identified adducted residue was used as a criterion for successful labeling. Pocket prediction success was defined as the percentage of docking events meeting these criteria across the entire probe library, and site prediction success considered only probes experimentally observed in proteomics. Molecular visualization of docking results was performed using ChimeraX 1.8.

### KRAS molecular dynamics simulations

Structural models of GDP-bound KRAS were generated via homology modeling (SwissModel) to ensure consistency with K-Ras4A (UniProt ID: P01116). Crystallographic water molecules were retained, and protonation states were assigned at pH 7.4.

Molecular dynamics simulations were performed in OpenMM 8.1.2 using Amber ff14SB for the protein and the recently published phosaa14SB for phosphotyrosine. Ligands were parameterized via Espaloma 0.3.2, and modified 12-6-4 Lennard-Jones parameters were used for divalent metal ions. Systems were solvated with TIP3P-FB water molecules and 0.15 M NaCl. A Langevin Middle Integrator was used with a 4-fs timestep combining HMR and SHAKE algorithms. Harmonic positional restraints were applied on all heavy atoms, and the systems were gradually heated to 300 K in the NVT ensemble. Subsequently, a Monte Carlo barostat was introduced, and 15 steps of NPT equilibration were performed, progressively releasing the restraints. Finally, 50 ns of unrestrained molecular dynamics simulations were conducted to ensure proper equilibration.

The experimental structure of $KRAS^{G13D}$ bound to the BI-2865 compound (PDB: 8B00) was simulated for 100 ns, and the average of the last 50 ns was used as a reference. The root mean square deviation (RMSD) to the BI-2865 binding competent conformation was calculated over the Cα atoms of residues within 4 Å of the ligand.

### Enhanced sampling protocol

An ad hoc computational sampling pipeline was implemented to explore the conformational landscape of the systems efficiently. Initially, well-tempered metadynamics simulations (WTMetaD) were conducted, biasing the RMSD of Cα atoms relative to the initial conformation. Gaussian potentials of height 0.3 kcal $mol^{-1}$ and width 0.01 nm were deposited every 2 ps with a bias factor of 10. Three simulations of 300 ns were run in parallel, sharing the bias history (that is, multiple-walker scheme). Then, all Cα pairwise distances (13,041 features) were calculated from the trajectories, and MoSAIC analysis was used to identify clusters of highly correlated motions. Features from the top three bigger clusters were subjected to principal component analysis, retaining the components that explained 95% of the variance. Regular space clustering in the reduced space was conducted to achieve uniform sampling, and 30 representative conformations were extracted for each system. Each state was equilibrated, followed by 200 ns of unbiased molecular dynamics.

### Metadynamics free energy surfaces

WTMetaD simulations were performed with PLUMED 2.9 using G12–T35 and G35–G60 minimum distances as collective variables. Gaussians

(0.5 kcal $mol^{-1}$ height, 0.01 nm width) were deposited every 1 ps with a bias factor of 12. Four independent replicas of 100 ns were simulated per system and combined using the mean force integration (MFI) method to obtain the free energy surfaces.

### Statistical analysis

All fluorescent gel scanning and western blots were performed with a minimum of two biological replicates. Compound effects at different doses were normalized to vehicle-treated cells and fitted with Sigmoidal 4PL curve. All statistical analysis was performed using GraphPad Prism (version 9.3.0 or version 10.4.0) or Microsoft Excel (version 2122). Proteomic data were statistically evaluated using two-tailed Student's *t*-tests performed across a minimum of two biological replicates, with significance defined as $P < 0.05$.

### Reporting summary

Further information on research design is available in the Nature Portfolio Reporting Summary linked to this article.

## Data availability

The data that support the findings in this work are available within the paper and the Supplementary Information (Supplementary Text and Supplementary Tables 1–15). Uncropped, full western blot images and fluorescent gels are provided in Source data and Supplementary Figs. 9–12. All raw proteomics data files have been deposited to the PRIDE repository and are available under accession numbers PXD056973 (unenriched and phosphorproteomics), PXD056976 (chemoproteomics) and PXD056980 (SoL). The simulation input PDB models necessary to reproduce the results in this study have been deposited in the Zenodo[97] public repository and are accessible under the digital object identifier https://doi.org/10.5281/zenodo.19054682. Source data are provided with this paper.

## Code availability

The scripts used to run and analyze the simulations in this study are part of an in-house software package currently under active development by the Forli laboratory. Because the complete software suite remains unpublished and is undergoing final development, the specific code necessary to reproduce the reported results is available from the corresponding author upon reasonable request. Upon the official release of the software, the full package will be made publicly accessible through the Forli laboratory GitHub repository at https://github.com/forlilab.

## References


90. Conway, L. P. et al. Evaluation of fully-functionalized diazirine tags for chemical proteomic applications. *Chem. Sci.* **12**, 7839–7847 (2021).
91. Tang, J. et al. Synthesis of portimines reveals the basis of their anti-cancer activity. *Nature* **622**, 507–513 (2023).
92. Yu, F. et al. Identification of modified peptides using localization-aware open search. *Nat. Commun.* **11**, 4065 (2020).
93. Thomas, P. D. et al. PANTHER: making genome-scale phylogenetics accessible to all. *Protein Sci.* **31**, 8–22 (2022).
94. Garrigou, M. et al. Accelerated identification of cell active KRAS inhibitory macrocyclic peptides using mixture libraries and Automated Ligand Identification System (ALIS) technology. *J. Med. Chem.* **65**, 8961–8974 (2022).
95. Forli, S. et al. Computational protein–ligand docking and virtual drug screening with the AutoDock suite. *Nat. Protoc.* **11**, 905–919 (2016).
96. Santos-Martins, D. et al. Accelerating AutoDock4 with GPUs and gradient-based local search. *J. Chem. Theory Comput.* **17**, 1060–1073 (2021).
97. Llanos, M., & Forli, S. Simulation files for KRAS phosphorylation dependent ligandability changes. https://doi.org/10.5281/zenodo.19054682 (2026).


## Acknowledgements

We thank C. Frohreich and P. Ordoukhanian from the Biophysics and Biochemistry Core at Scripps Research for SPR. We also thank B. F. Cravatt for useful discussions and input. The research of C.G.P. in this area is supported by National Institute of Allergy and Infectious Diseases grants R01AI156268 and R01AI182439 as well as grant 2023-332369 from the Chan Zuckerberg Initiative DAF, an advised fund of the Silicon Valley Community Foundation. Q.W. is supported by the Hou Wang Fellowship in the Skaggs Graduate School. M.L.H. acknowledges support from the National Institute of General Medical Sciences under grant R35GM142462.

## Author contributions

C.G.P., W.L. and Q.W. conceived the study, designed experiments and interpreted results. W.L. and Q.W. performed the proteomics experiments, analyzed MS data and performed validation experiments, with input from A.D. and M.L.H. S.F. and P.G. performed molecular docking analysis. S.F., M.L. and M.H. performed molecular dynamics analysis. T.-Y.C., C.G. and J.C. assisted with validation experiments. J.M.W. assisted with proteomics experiments. A.M.J. synthesized compounds. C.G.P., W.L. and Q.W. wrote the manuscript, with input from all authors.

## Competing interests

C.G.P. is a founder of and scientific advisor to Belharra Therapeutics, a biotechnology company interested in using chemical proteomic methods to develop small-molecule therapeutics. A.D. is an employee of Bristol Myers Squibb. All other authors declare no competing interests.

## Additional information

**Extended data** is available for this paper at https://doi.org/10.1038/s41589-026-02216-y.

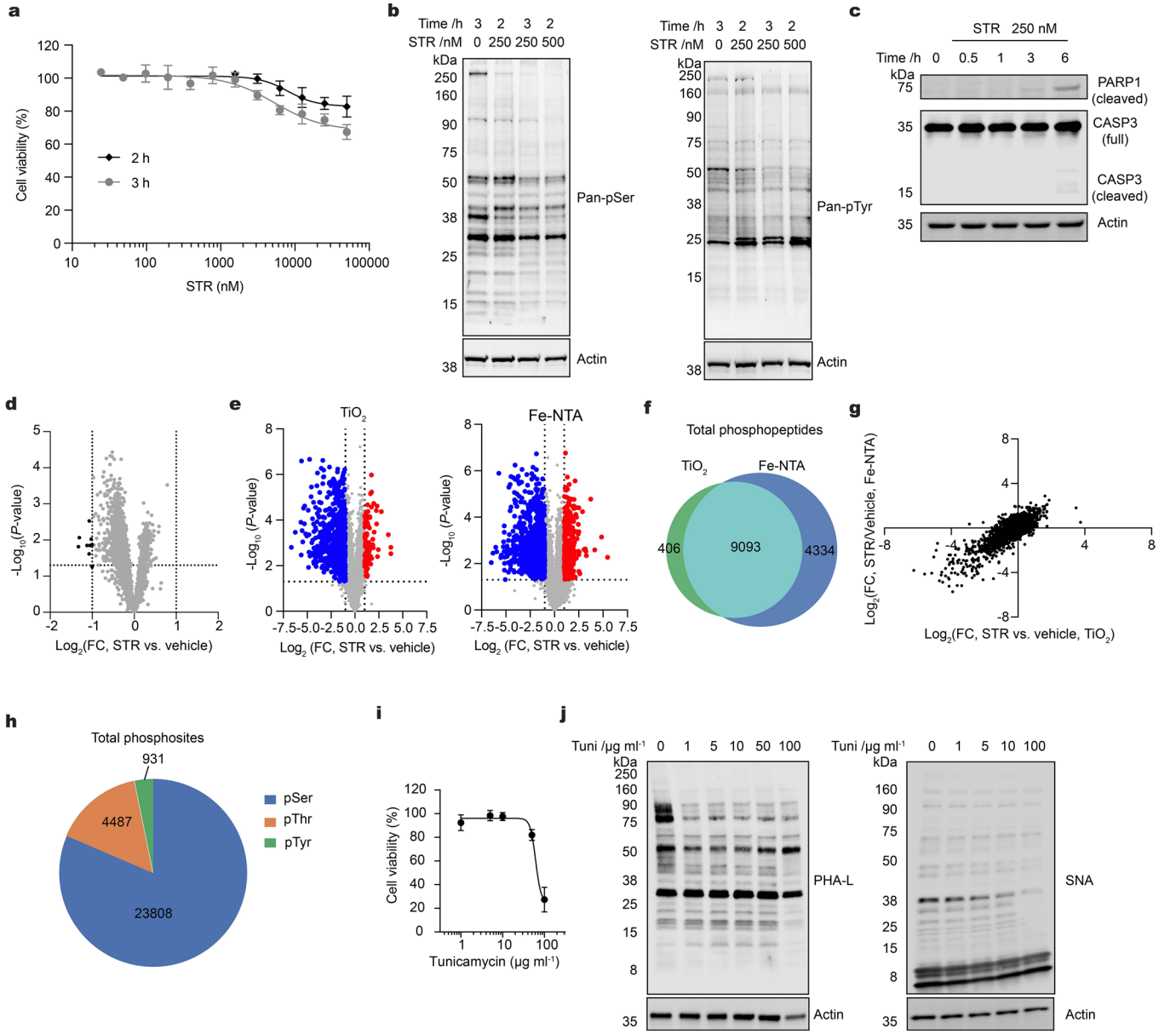
**Supplementary information** The online version contains supplementary material available at https://doi.org/10.1038/s41589-026-02216-y.

**Correspondence and requests for materials** should be addressed to Christopher G. Parker.

**Peer review information** *Nature Chemical Biology* thanks Kirill Medvedev, Matthew Pratt and the other, anonymous reviewer(s) for their contribution to the peer review of this work.

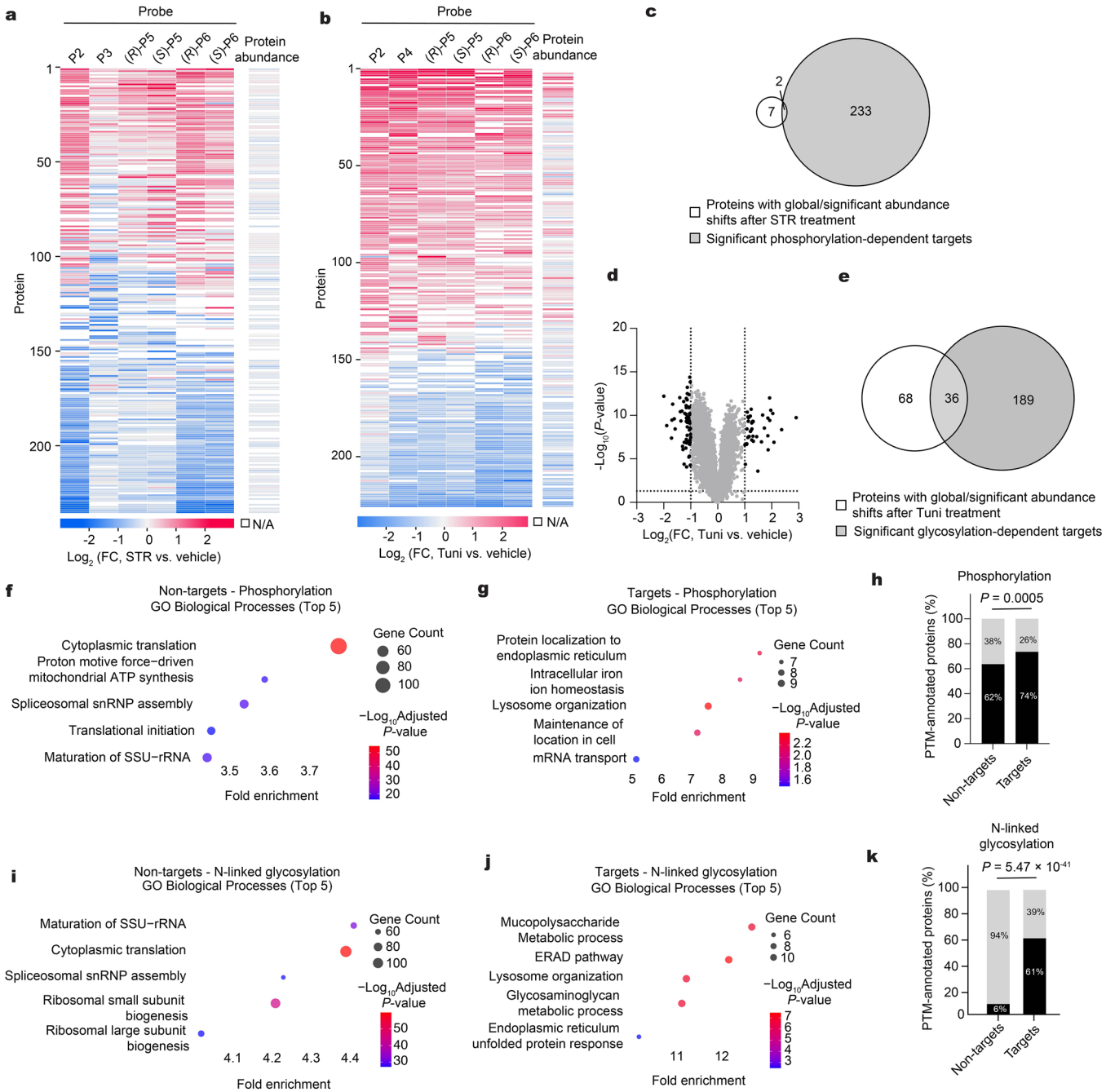
**Reprints and permissions information** is available at www.nature.com/reprints.

https://doi.org/10.1038/s41589-026-02216-y



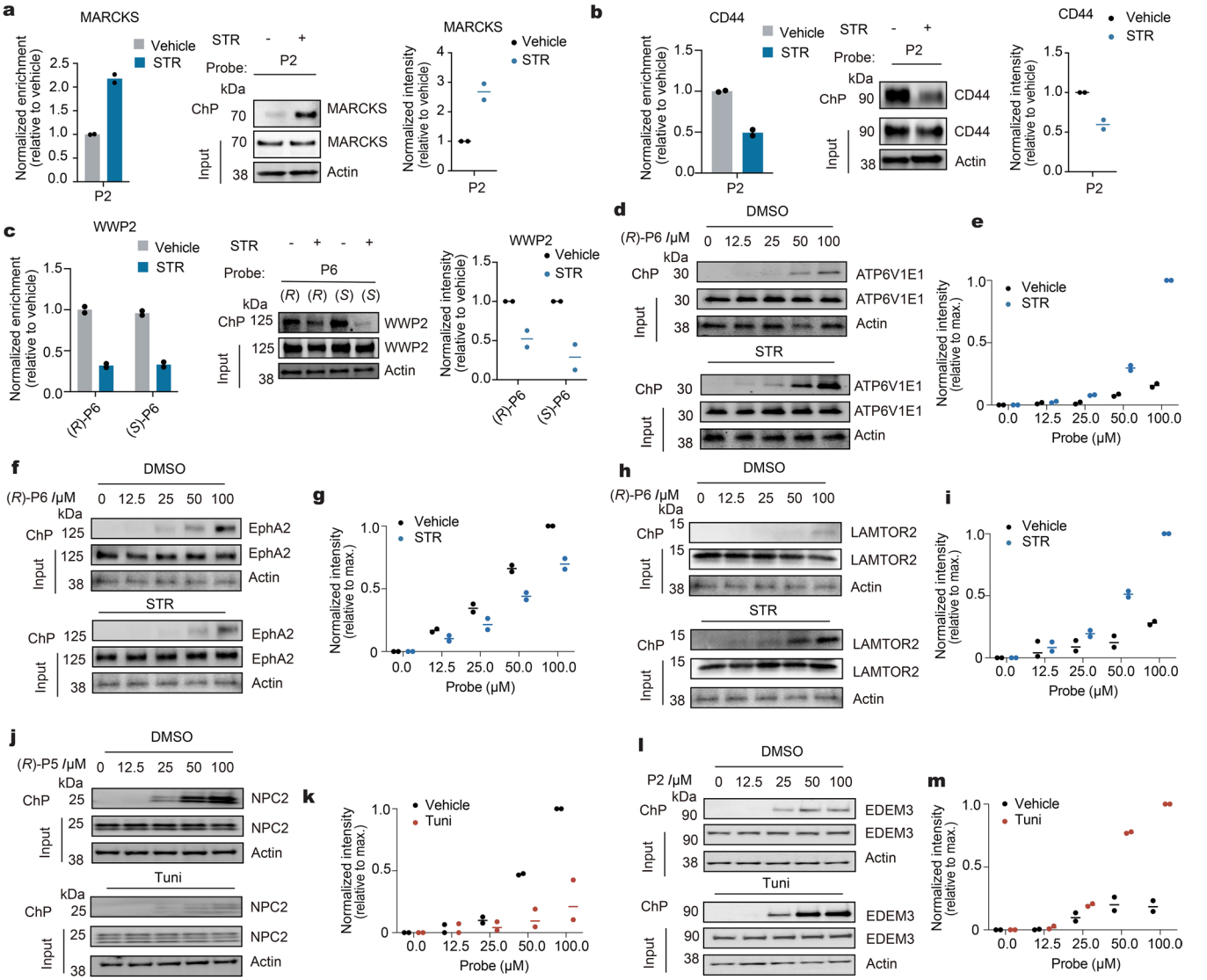

**Extended Data Fig. 1 | Characterization of PTM-dependent model systems.** **a**, Cell viability of MDA-MB-231 cells treated with staurosporine (STR) at indicated concentrations and treatment times. **b**, Immunoblot analysis of global serine (left) and tyrosine (right) phosphorylation levels in MDA-MB-231 cells across STR concentrations and treatment durations. **c**, Apoptosis evaluation in MDA-MB-231 cells treated with 250 nM STR, as indicated by changes in the abundance of cleaved PARP1 and caspase-3 at indicated time points. **d**, Volcano plots of protein abundances comparing PTM-dependent targets displaying abundance changes after STR treatment. Vertical dashed lines represent a 2-fold change (FC) threshold, while horizontal dashed lines denote a *p*-value threshold of 0.05. Black dots highlight proteins that meet both significance thresholds. **e**, Volcano plots of phosphoproteomics experiments using different enrichment methods. Left, $TiO_2$ enrichment; right, Fe-NTA enrichment. The vertical dashed line corresponds to a 2-fold change (FC) and the horizontal line corresponds to a p-value of 0.05. Colored dots correspond to phospho-peptides passing both specified thresholds, gained (red) and loss (blue). **f**, Venn diagram comparing phospho-peptides enriched by two methods. **g**, Correlation of phospho-peptide quantitation by two enrichment methods. **h**, Pie chart of enriched phospho-sites distribution, pSer (blue), pThr (orange) and pTyr (green). See data in Table S9-10. **i**, Assessment of HEK293T cell viability following treatment with tunicamycin (Tuni) at indicated concentrations for 24 h. **j**, Immunoblot analysis of global N-linked glycosylation levels in HEK293T cells treated with tunicamycin for 24 h at indicated concentrations, using *Phaseolus vulgaris* leucoagglutinin (PHA-L) and Sambucus nigra agglutinin (SNA) lectins. Proteomic data and cell viability data were obtained from three independent biological replicates and are presented as mean ± s.d. Gel images are representative of two independent experiments. Associated datasets are provided in Supplementary Tables 5, 9–10.

https://doi.org/10.1038/s41589-026-02216-y



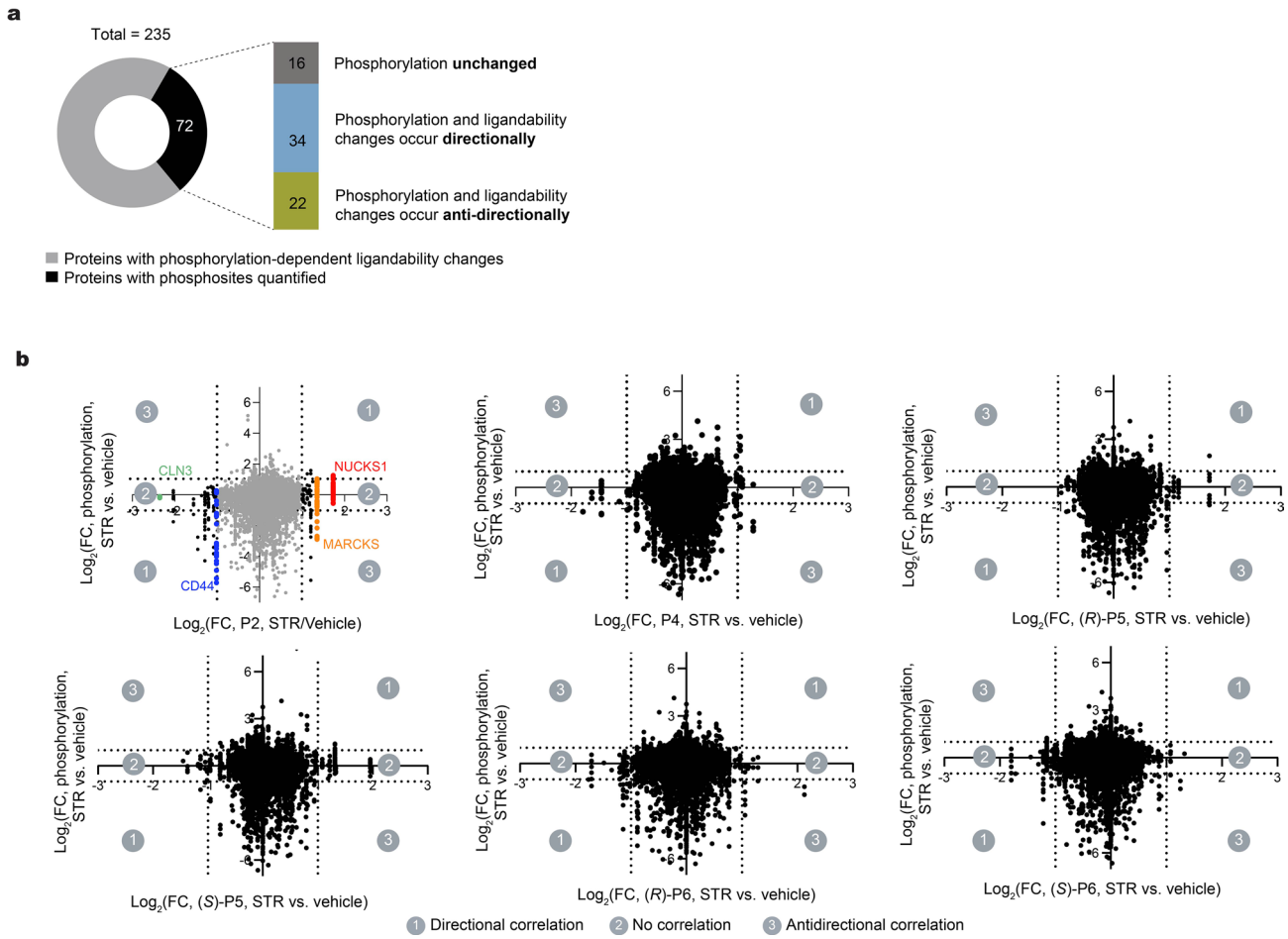

**Extended Data Fig. 2 | Proteomic profiling of PTM-dependent ligandability events in cells. a**-**b**, Heatmap of proteins displaying significant ligandability changes (FC > 2, $p < 0.05$) after treatment with STR or Tuni and associated abundance changes. **a**, phosphorylation; **b**, N-linked glycosylation perturbations. Observed proteins with increased (red) and decreased (blue) ligandability changes. Protein abundance changes before and after STR or Tuni treatment were detected by unenriched proteomics. N/A, not detected from the unenriched proteomics. **c**-**e**, Venn diagram (**c**, **e**) and volcano plots (**d**) of protein abundances and comparing PTM-dependent targets displaying abundance changes after STR (**c**) or Tuni (**d**-**e**) treatment. Vertical dashed lines represent a 2-fold change (FC) threshold, while horizontal dashed lines denote a *p*-value threshold of 0.05. Black dots highlight proteins that meet both significance thresholds. **f**-**g**, **i**-**j**, Gene Ontology (GO) biological process enrichment analysis comparing non-targets (proteins enriched by probes, but do not display PTM-dependent ligandability; **f**, **i**) relative to PTM-dependent targets (**g**, **j**). Top 5 enriched terms shown for phosphorylation (**f**,**g**) and N-linked glycosylation (**i**, **j**) datasets. Dot size indicates gene count; color indicates significance (-log adjusted *P*-value). **h**,**k**, Proportion of proteins with UniProt-annotated PTM sites comparing the total non-targets versus the identified PTM-dependent targets for phosphorylation (**h**) and N-linked glycosylation (**k**). Statistical significance assessed by a Chi-square test. Proteomic data were obtained from two independent biological replicates and are presented as mean. Significance was determined using a two-tailed Student's *t*-test. Associated datasets are provided in Supplementary Tables 1–8.

https://doi.org/10.1038/s41589-026-02216-y



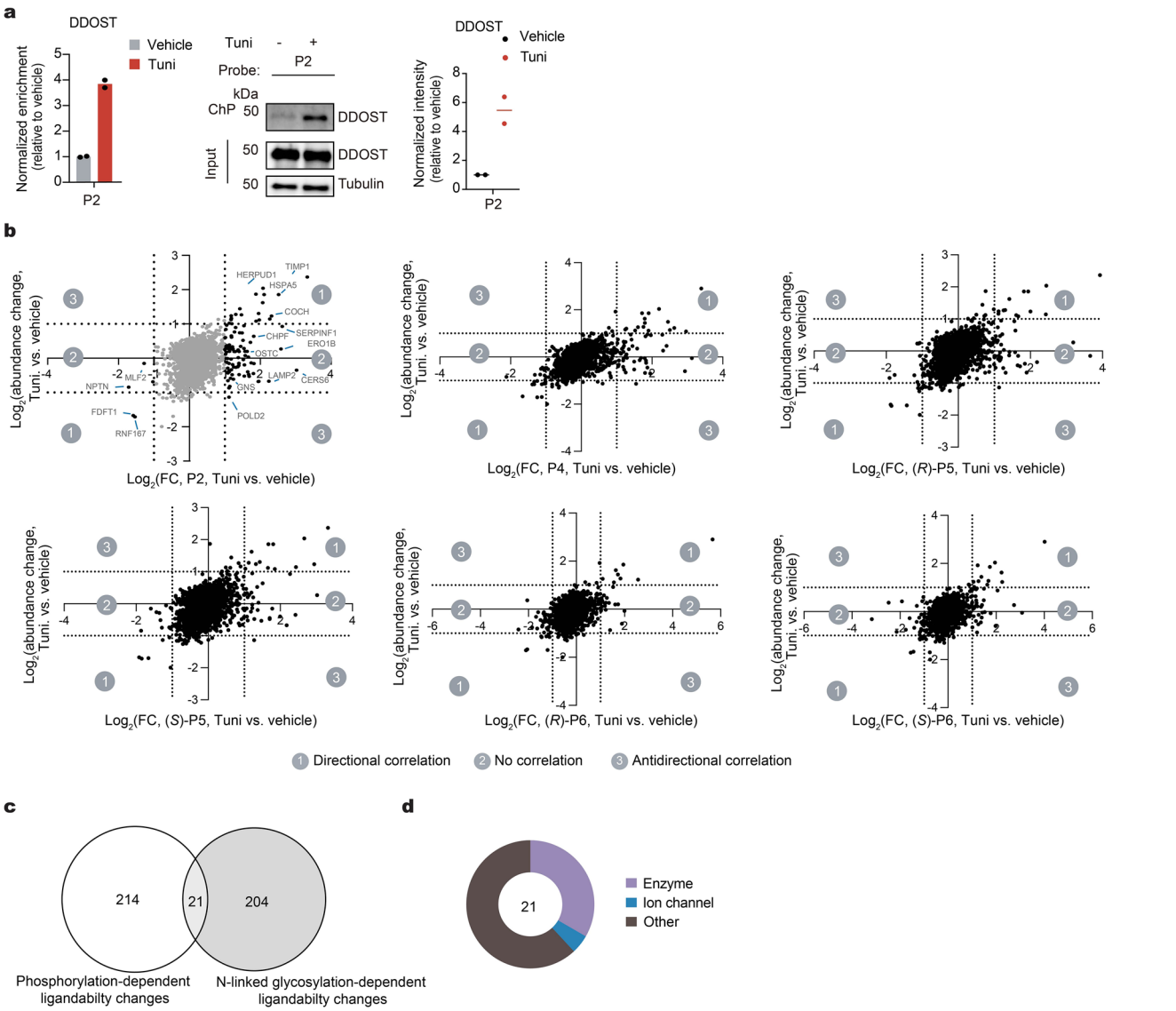

**Extended Data Fig. 3 | Analysis and validation of PTM-dependent ligandability events. a-c**, Proteomic profiles and corresponding chemo-precipitation (ChP) validation for selected targets exhibiting PTM-sensitive probe binding: MARCKS (**a**), CD44 (**b**) and WWP2 (**c**). Left panels show quantitative chemoproteomic data; middle panels display ChP immunoblots; right panels show corresponding quantification across biological replicates. **d-i**, (*R*)-P6 probe labeling of ATP6V1E1 (**d-e**), EphA2 (**f-g**), and LAMTOR2 (**h-i**) is increased following STR across a broad range of concentration. **j-m**, Labeling of NPC2 by (*R*)-P5 (**j-k**) and EDEM3 by P2 (**l-m**) is increased upon Tuni treatment across a broad range of probe concentrations. Representative immunoblots show chemoprecipitation (ChP) signal and input loading controls. Scatter plots depict the quantification of probe labeling intensity normalized to the maximum signal across biological replicates. Gel images are representative of two independent experiments. Associated datasets are provided in Supplementary Tables 1–4 and 9–10.

https://doi.org/10.1038/s41589-026-02216-y



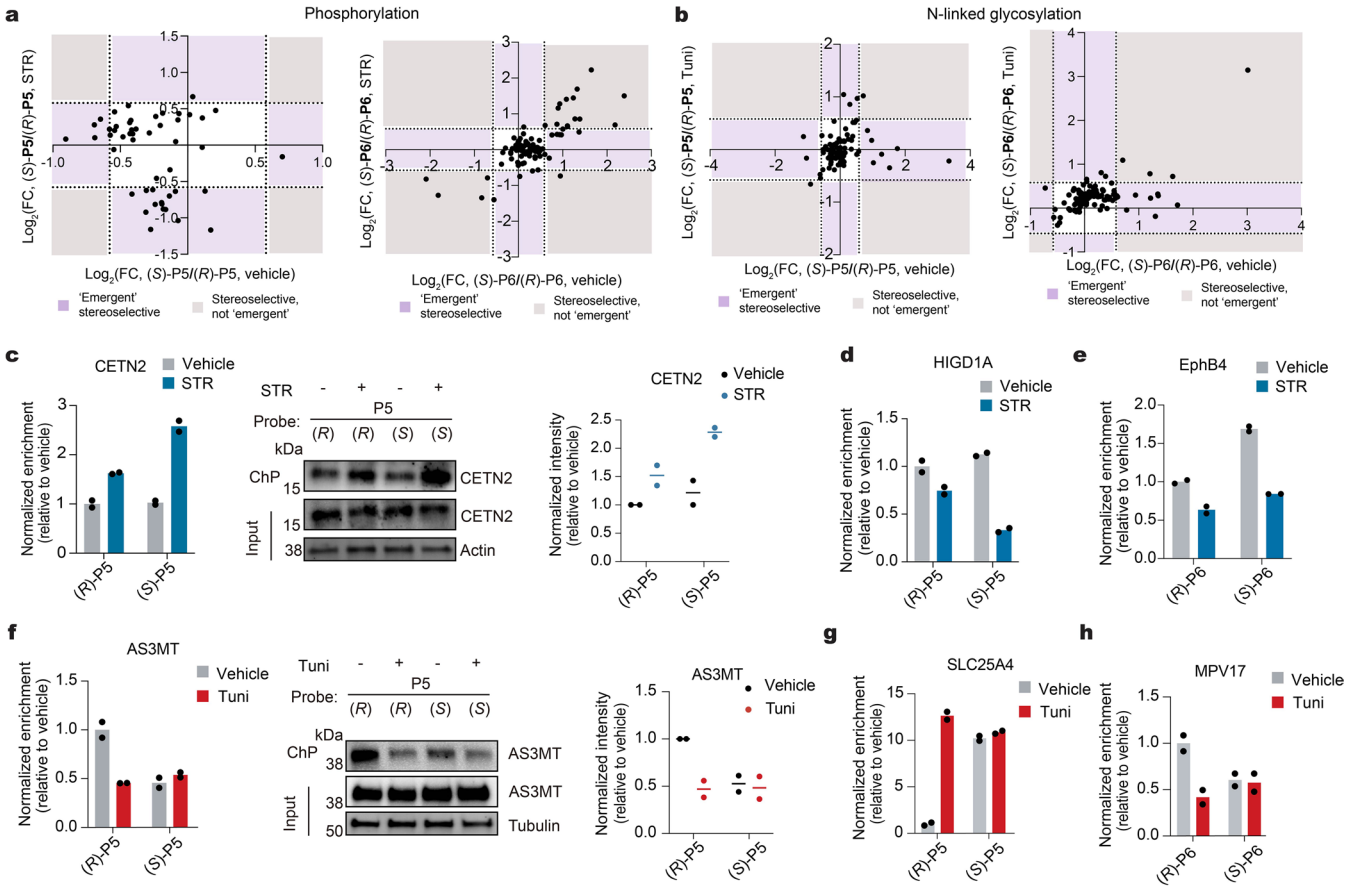

**Extended Data Fig. 4 | Analysis of phosphorylation-dependent ligandability events. a**, Distribution of phosphorylation-dependent targets with quantified phosphosites from phosphoproteomics experiments. **b**, Scatter plot depicting protein ligandability change versus phosphorylation change with indicated probes after STR treatment in MDA-MB-231 cells. Plots marked with three regions of ligandability changes: ligandability changes align with phosphorylation changes (region 1), ligandability changes occur without corresponding phosphorylation changes (region 2), and ligandability changes occur in the opposite direction of phosphorylation changes (region 3). The vertical and the horizontal dashed line represent a 2-fold change (FC) threshold. Proteomic data were obtained from two independent biological replicates and are presented as mean. Associated datasets are provided in Supplementary Tables 1–4 and 9–10.

https://doi.org/10.1038/s41589-026-02216-y



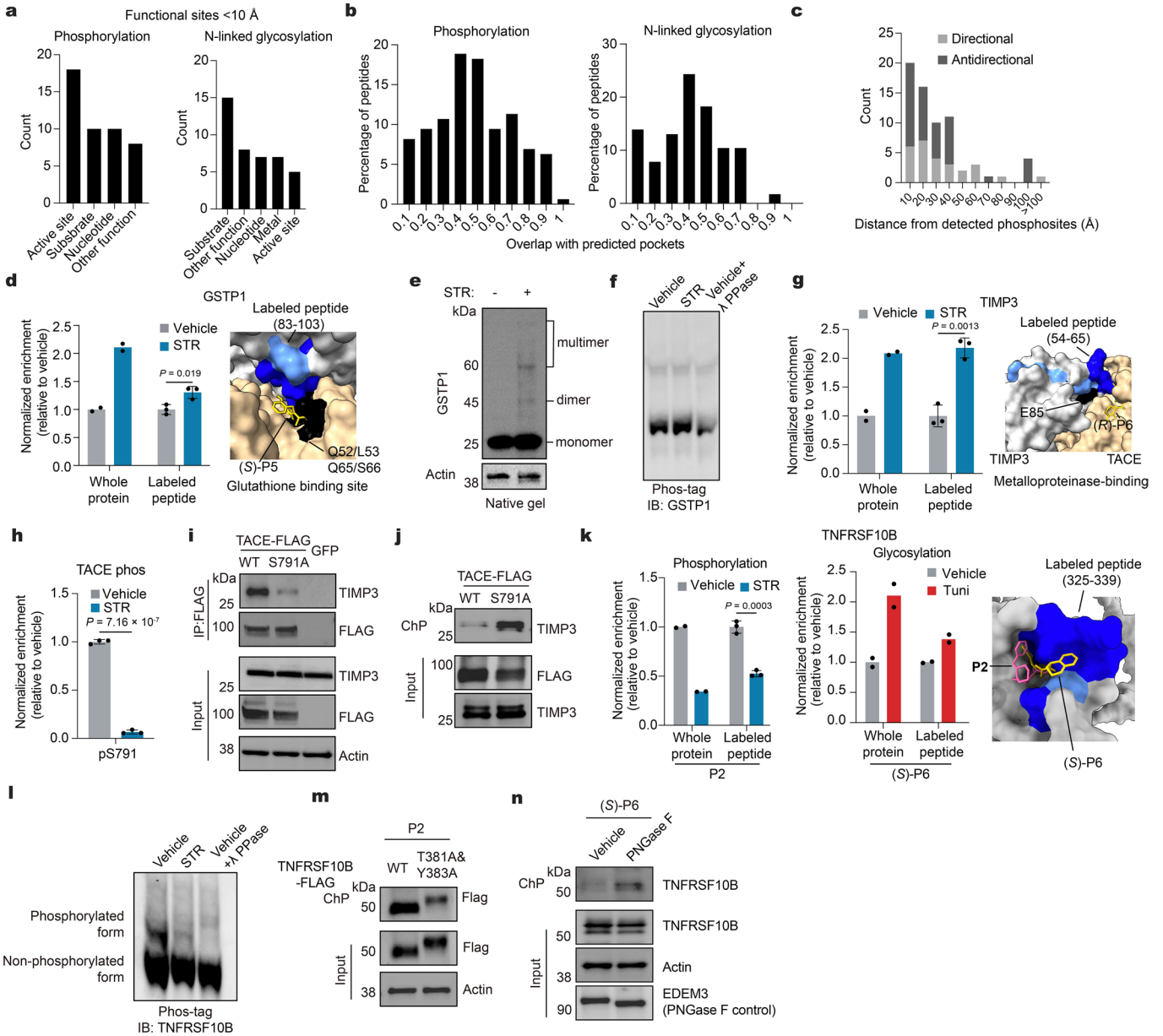

**Extended Data Fig. 5 | Analysis and validation of glycosylation-dependent ligandability events. a**, Proteomic profiles and corresponding chemoprecipitation (ChP) validation for DDOST. Left panel shows quantitative chemoproteomic data; middle panel shows ChP immunoblot results; right panel shows corresponding quantification across biological replicates. **b**, Scatter plot depicting protein ligandability change versus abundance change with indicated probes after Tuni treatment in HEK293T cells. Plots marked with three regions of ligandability changes: ligandability changes align with abundance changes (region 1), ligandability changes occur without corresponding abundance changes (region 2), and ligandability changes occur in the opposite direction of abundance changes (region 3). The vertical and the horizontal dashed line represent a 2-fold change (FC) threshold. **c**, Venn diagram comparing proteins with ligandability changes in both PTMs. **d**, IDG functional classes of proteins with ligandability changes in both PTMs. Proteomic data and immunoblot quantification derived from two independent biological replicates are presented as the mean with individual data points overlaid. Associated datasets are provided in Supplementary Tables 1–4 and 6–8.

https://doi.org/10.1038/s41589-026-02216-y



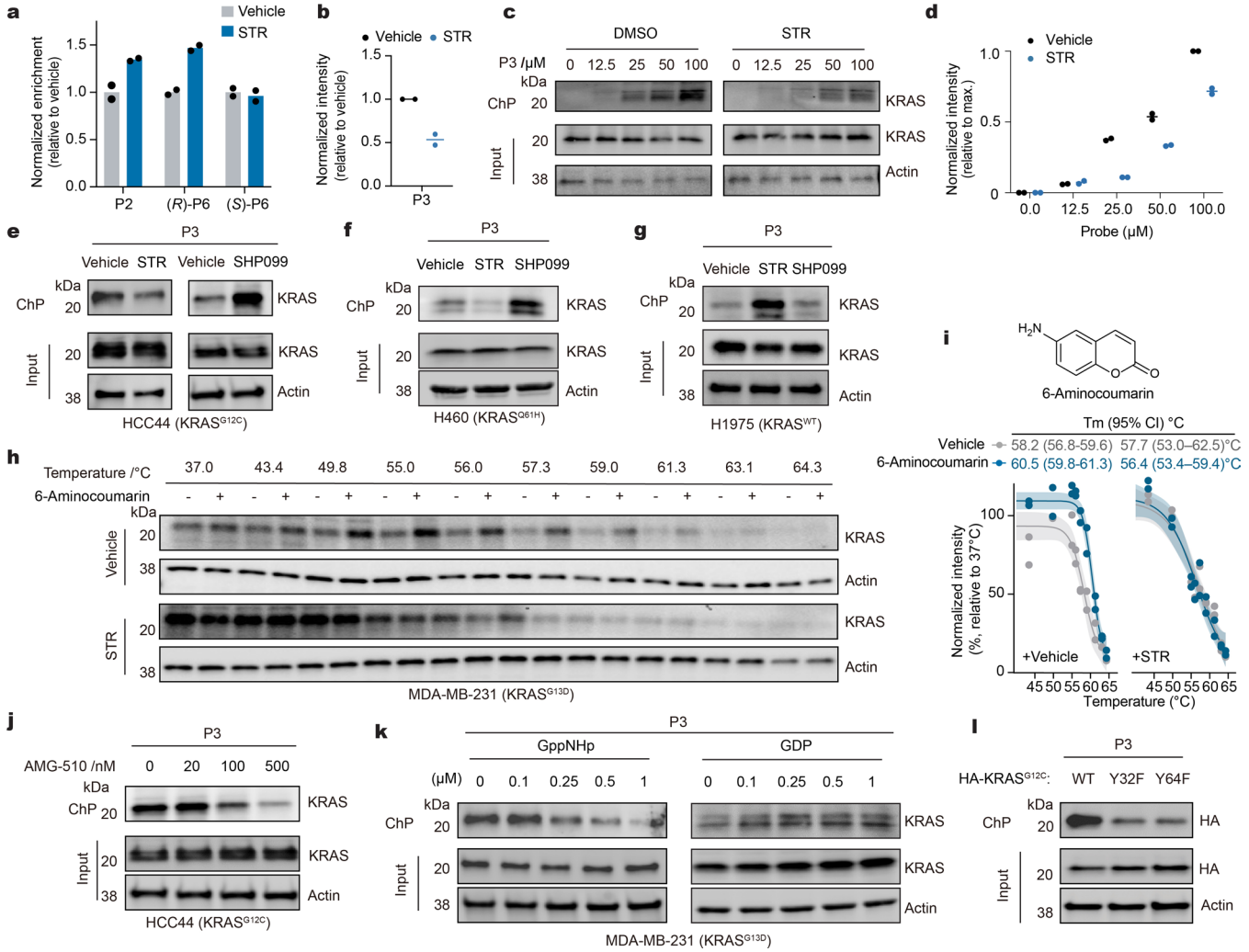

**Extended Data Fig. 6 | Discovery of emergent stereoselective PTM-dependent events. a**-**b**, Scatter plots of significant PTM-dependent targets of enantioprobes to compare stereoselectivity between DMSO and STR or Tuni treated cells. The vertical and the horizontal dashed line represent a 1.5-fold change (FC) threshold. Proteins with emergent stereoselectivity (stereoselective engagement in one condition but not the other) are shown in pink region and ones displaying stereoselectivity in both states are in grey region. **a**, phosphorylation; **b**, N-linked glycosylation perturbed conditions. **c**,**f**, Proteomic profiles (left), chemo-precipitation (ChP) validation (middle) and quantification (right) of ligandability changes of CETN2 (**c**) and AS3MT (**f**). **d**-**e**, **g**-**h**, Proteomic profiles of indicated proteins. HIGD1A (**d**), EphB4 (**e**), SLC25A4 (**g**), MPV17 (**h**). Proteomic data and immunoblot quantification derived from two independent biological replicates are presented as the mean with individual data points overlaid. Associated datasets are provided in Supplementary Tables 1–4 and 6–7.

https://doi.org/10.1038/s41589-026-02216-y



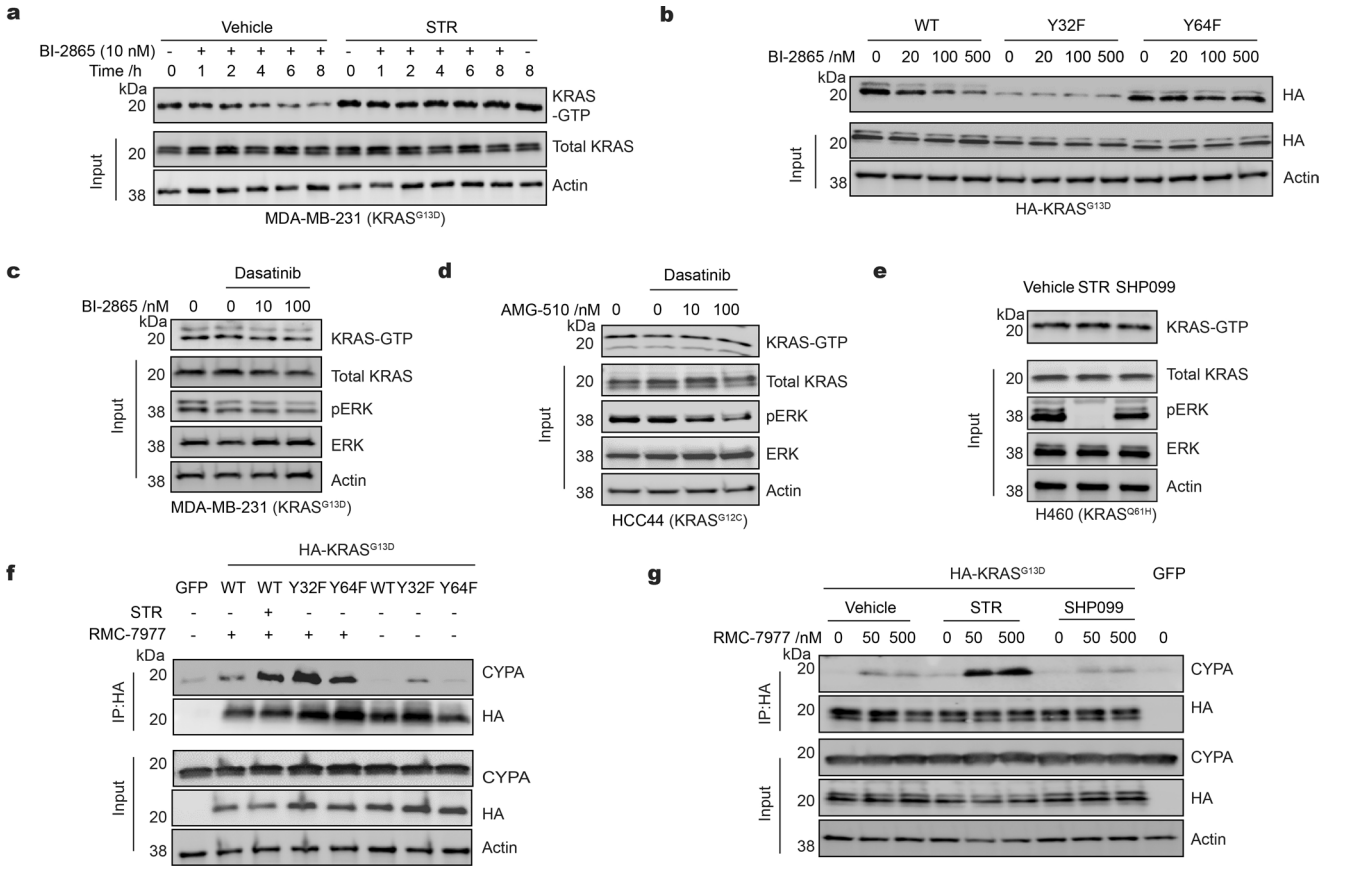

**Extended Data Fig. 7 | Features of pockets displaying PTM-dependent ligandability. a**, Categorization of functional sites (Uniprot) located within 10 Å of probe-labeled peptides for phosphorylation (left) and N-linked glycosylation (right) datasets. **b**, Overlap of PTM-dependent probe-labeled peptides with predicted pockets (Fpocket). **c**, Histogram showing the spatial distance of probe-labeled peptides to the detected quantified phosphosites. **d**, Proteomic profile of whole protein and peptide (83-103) labeled by (*S*)-P5 (left) and docked structure (PDB 2A2R) highlighting the probe site near the glutathione binding site (right). **e**, Native gel analysis showing GSTP1 oligomerization states under vehicle or STR treatment. **f**, Phos-tag western blot showing GSTP1 phosphorylation is not obviously changed under STR or λ-PPase treatment. **g**, Proteomic profile of TIMP3 and peptide (54-65) labeled by (*R*)-P6 (left) and docked structure (PDB 3CKI) showing the probe site near the metalloproteinase-binding interface (right). **h**, Quantification of TACE pS791 levels following STR treatment. **i**, Co-immunoprecipitation of TIMP3 with FLAG-tagged TACE (WT vs S791A). **j**, ChP validation showing altered TIMP3 ligandability in cells expressing the phosphorylation-deficient TACE-S791A mutant. **k**, Proteomic profiles for phosphorylation-dependent labeling by P2 (left) and glycosylation-dependent labeling by (*S*)-P6 (middle), alongside a docked structure (AF-Q8N8Q9-F1) showing the distinct binding sites (right). **l**, Phos-tag blot confirming TNFRSF10B phosphorylation status. **m**, ChP validation showing reduced P2 binding to the phosphorylation-deficient mutant (T381A/Y383A). **n**, ChP validation showing enhanced (*S*)-P6 binding following enzymatic deglycosylation by PNGase F. For all structures, the primary peptide residues labeled by probes are colored dark blue and the remainder colored light blue. PTM sites in red ('annotated' sites cataloged in Uniprot or PhosphoSitePlus database; 'observed' sites detected in phosphoproteomics showing changes upon STR treatment), functional sites are colored black, and probes are colored gold. Proteomic data and immunoblot quantifications derived from two independent biological replicates are presented as the mean with individual data points overlaid. Proteomic data derived from three independent biological replicates are presented as mean ± s.d. Significance was determined using a two-tailed Student's *t*-test. Associated datasets are provided in Supplementary Tables 1–4, 6–7 and 9–12.

https://doi.org/10.1038/s41589-026-02216-y



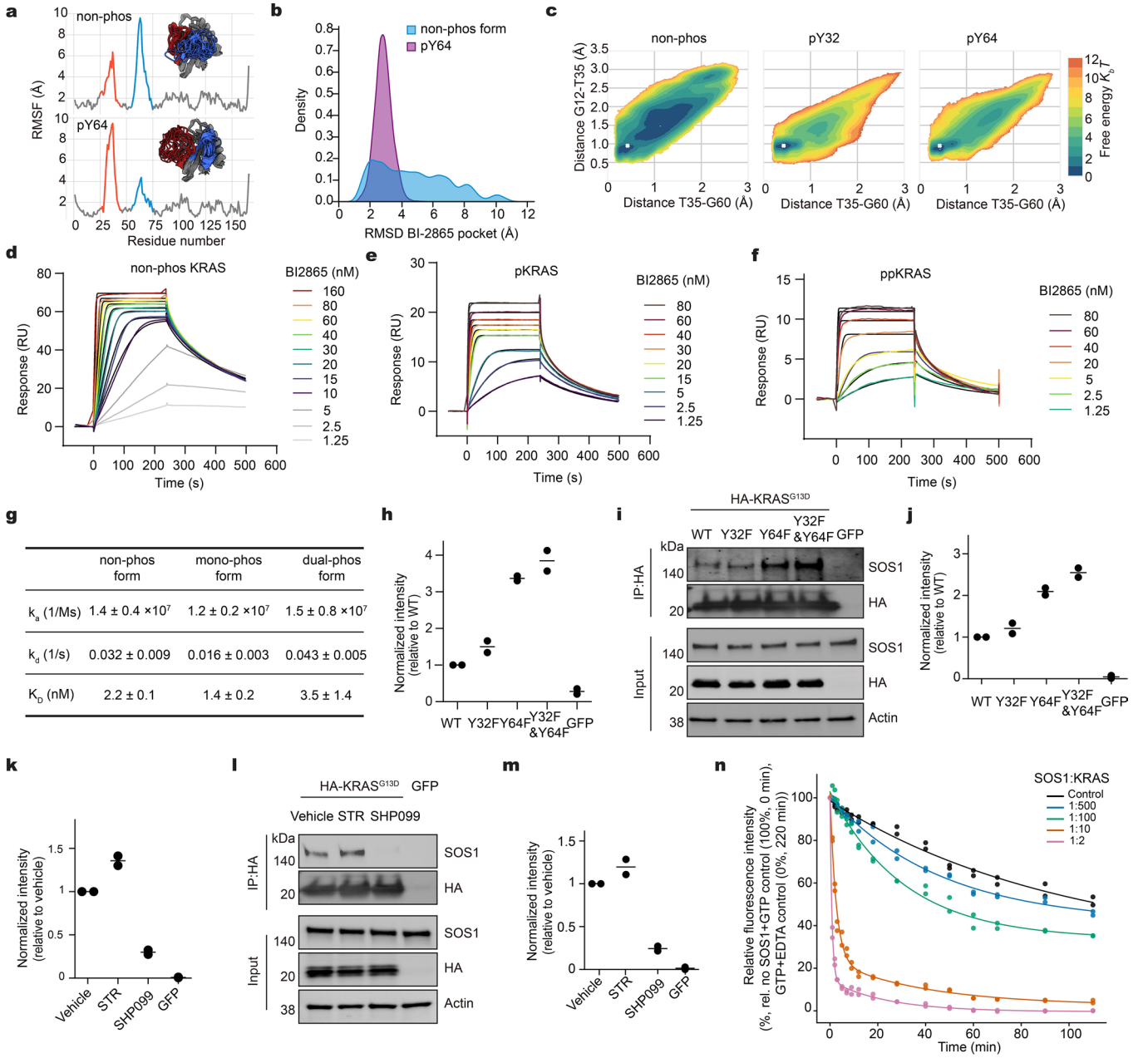

**Extended Data Fig. 8 | Phosphorylation status impacts KRAS ligandability.** **a**, Proteomic profile of P2 and (*R*/*S*)-P6 binding to KRAS$^{G13D}$ following STR treatment in MDA-MB-231 cells. **b**, Quantification of immunoblot replicates in Fig. 5b. **c**-**d**, Dose-dependent validation of phosphorylation-dependent ligandability. Representative ChP immunoblots (**c**) and quantification (**d**) of P3 (0-100 μM) engagement with KRAS$^{G13D}$ in MDA-MB-231 cells treated with vehicle or STR (250 nM, 3 h). **e**-**g**, ChP analysis of P3 binding to KRAS variants in different cell lines: **e**, KRAS$^{G12C}$ in HCC44 cells treated with vehicle, STR, or SHP099; **f**, KRAS$^{Q61H}$ in H460 cells; **g**, KRAS$^{WT}$ in H1975 cells. **h**, Cellular thermal shift assay (CETSA) immunoblots of KRAS$^{G13D}$ in MDA-MB-231 cells treated with vehicle or STR in the presence of 6-Aminocoumarin. **i**, Chemical structure of 6-Aminocoumarin and corresponding melting curves showing no significant thermal stabilization. Data are presented as mean with 95% confidence intervals for curve fits. **j**, ChP competition assay P3 binding to KRAS$^{G12C}$ co-incubated with AMG510 at indicated concentrations in HCC44 cells. **k**, ChP analysis of P3 binding to KRAS$^{G13D}$ when co-incubated with increasing concentration of GppNHp (left) and GDP (right) in MDA-MB-231 cells. **l**, ChP analysis of P3 binding to HA-KRAS$^{G12C}$ Y32F and Y64F recombinantly expressed in LX293T cells. Proteomic data and immunoblots were quantified from two independent biological replicates and plotted as the mean. Gel images are representative of two independent experiments. Associated datasets are provided in Supplementary Tables 1 and 4.

https://doi.org/10.1038/s41589-026-02216-y




**Extended Data Fig. 9 | Influence of phosphorylation status on KRAS inhibitor activity. a**, Immunoblot of GTP-bound KRAS by RBD pull-down assay in MDA-MB-231 cells. Cells were pre-treated with STR (250 nM, 3 h) and co-treated with BI-2865 and STR for indicated time. **b**, Immunoblot and quantification plot of mutant GTP-bound HA-KRAS$^{G13D}$ levels in LX293T cells expressing HA-tagged KRAS$^{G13D}$ constructs containing Y32 and Y64 site-specific mutations. Cells were treated with BI-2865 for 5 h followed by immunoblot after HA-tag pulldown. **c**, Immunoblot of GTP-bound KRAS by RBD pull-down assay in dasatinib-treated (1 μM, 1 h) MDA-MB-231 cells with BI-2865 (1 h). **d**, Immunoblot of GTP-bound KRAS by RBD pull-down assay in dasatinib-treated (1 μM, 1 h) HCC44 cells with AMG-510 (1 h). **e**, Immunoblot of GTP-bound KRAS$^{Q61H}$ by RBD pull-down assay in STR (250 nM) or SHP099 (500 nM) treated in H460 cells. **f**, LX293T cells expressing HA-tagged KRAS$^{G13D}$ Y32F and Y64F mutants were treated with RMC-7977 (500 nM, 2 h) with STR followed by HA-pulldown and CYPA immunoblot. **g**, LX293T cells expressing HA-tagged KRAS$^{G13D}$ were treated with STR (250 nM) or SHP099 (500 nM), and RMC-7977 with indicated concentration for 2 h followed by HA-pulldown and CYPA immunoblot. Results are representative of two or three biological replicates.

https://doi.org/10.1038/s41589-026-02216-y




| | non-phos form | mono-phos form | dual-phos form |
|---|---|---|---|
| $k_a$ (1/Ms) | 1.4 ± 0.4 ×10$^7$ | 1.2 ± 0.2 ×10$^7$ | 1.5 ± 0.8 ×10$^7$ |
| $k_d$ (1/s) | 0.032 ± 0.009 | 0.016 ± 0.003 | 0.043 ± 0.005 |
| $K_D$ (nM) | 2.2 ± 0.1 | 1.4 ± 0.2 | 3.5 ± 1.4 |

**Extended Data Fig. 10 | Mechanisms underlying phosphorylation-dependent KRAS ligandability. a**, Per-residue root-mean-square-fluctuation (RMSF) plots quantitatively illustrate the differential flexibility of SW-I (red) and SW-II (blue) regions for non-phosphorylated form and Y64 phosphorylated form of KRAS$^{G13D}$. Representative structural ensembles extracted from clustering unbiased simulations are shown for each system, highlighting the conformational heterogeneity of these KRAS variants. **b**, Density plots showing the distribution of RMSD values for residues in the BI-2865 binding pocket, which were used to assess the extent to which sampled conformations are binding-competent. **c**, Free Energy Surfaces (FES) for KRAS$^{G13D}$ and the two potential phosphorylated variants, Y32 and Y64, obtained by metadynamics simulations. As a reference, the BI-2865 binding-competent conformation is shown as a white cross. For the phosphorylated variants, a single energy minimum exists and matches the BI-2865 bound conformation. **d**-**g**, Surface plasmon resonance (SPR) analysis of BI-2865 binding to purified KRAS$^{G12C}$ variants. **d**-**f**, Sensorgrams for non-phosphorylated (**d**), mono-phosphorylated (pY64, **e**), and dual-phosphorylated (pY32/pY64, **f**) forms. **g**, Summary of kinetic constants ($k_a$, $k_d$, $K_D$) revealing no significant difference in inhibitor affinity across phosphorylation states. **h**-**m**, Validation of SOS1 interaction with KRAS mutants. **i**, Co-IP of endogenous SOS1 with HA-KRAS$^{G13D}$ WT and phosphorylation-deficient mutants (Y32F, Y64F, Y32/64F) in LX293T cells. **h**, **j**, Quantification of SOS1 binding relative to WT. Mutations blocking phosphorylation significantly enhance SOS1 binding. **l**, Co-IP of SOS1 with HA-KRAS$^{G13D}$ following treatment with vehicle, STR (250 nM), or SHP099 (0.5 µM). **k**, **m**, Quantification of SOS1 binding. **n**, Optimization of the *in vitro* nucleotide exchange assay. Fluorescence-based GDP-to-GTP exchange curves of KRAS in the presence of increasing ratios of SOS1 (1:500 to 1:2). Data derived from two independent biological replicates are presented as the mean with individual data points overlaid.

nature portfolio

Corresponding author(s): Christopher G. Parker

Last updated by author(s): Mar 13, 2026

# Reporting Summary

Nature Portfolio wishes to improve the reproducibility of the work that we publish. This form provides structure for consistency and transparency in reporting. For further information on Nature Portfolio policies, see our Editorial Policies and the Editorial Policy Checklist.

## Statistics

For all statistical analyses, confirm that the following items are present in the figure legend, table legend, main text, or Methods section.

| n/a | Confirmed |
|---|---|
| ☐ | ☒ The exact sample size (*n*) for each experimental group/condition, given as a discrete number and unit of measurement |
| ☐ | ☒ A statement on whether measurements were taken from distinct samples or whether the same sample was measured repeatedly |
| ☐ | ☒ The statistical test(s) used AND whether they are one- or two-sided<br>*Only common tests should be described solely by name; describe more complex techniques in the Methods section.* |
| ☒ | ☐ A description of all covariates tested |
| ☒ | ☐ A description of any assumptions or corrections, such as tests of normality and adjustment for multiple comparisons |
| ☐ | ☒ A full description of the statistical parameters including central tendency (e.g. means) or other basic estimates (e.g. regression coefficient) AND variation (e.g. standard deviation) or associated estimates of uncertainty (e.g. confidence intervals) |
| ☐ | ☒ For null hypothesis testing, the test statistic (e.g. *F*, *t*, *r*) with confidence intervals, effect sizes, degrees of freedom and *P* value noted<br>*Give P values as exact values whenever suitable.* |
| ☒ | ☐ For Bayesian analysis, information on the choice of priors and Markov chain Monte Carlo settings |
| ☒ | ☐ For hierarchical and complex designs, identification of the appropriate level for tests and full reporting of outcomes |
| ☒ | ☐ Estimates of effect sizes (e.g. Cohen's *d*, Pearson's *r*), indicating how they were calculated |

*Our web collection on statistics for biologists contains articles on many of the points above.*

## Software and code

Policy information about availability of computer code

| | |
|---|---|
| Data collection | All software used in this studies are commercial available. A full description of software used in each study is provided in "Methods" section and Supplementary Information. Proteomics data was collected using Xcalibur from Thermo Fisher Scientific. Immunoblotting data were collected from Bio-Rad ChemiDoc Imaging System. |

| | |
|---|---|
| Data analysis | ChemDraw (21.0.0.28) were used for chemical structures. Proteomics data were analyzed using Proteome Discoverer (v3.0), MicroSoft Excel (v2212) and GraphPad Prism (v9.3.0 and v10.4.0), RStudio (v2024.12.1) and Python (v3.8.5). ChimeraX (v1.8), Bio-Rad Image Lab (v6.1.0), ZEN (v2.3), ImageJ (v1.53r17) and Imaris (v10.2) are used for immunoblotting and Immunostaining. For molecular modeling, the tridimensional coordinates of the probes were generated from SMILES using RDKit ETKDGv3 and UFF minimization. Atomic coordinates of the targets were retrieved from the Protein Data Bank (PDB), when available, otherwise, AlphaFold2 models were used. Where possible, x-ray structures were preferred over cryo-EM. Hydrogens were added to the target structures using Reduce, then coordinates of both ligand and targets were processed following the standard AutoDock protocol. KRAS structural models were built using the SwissModel server. Molecular dynamics simulations were performed with OpenMM 8.1.2 using in-house scripts and visualized with VMD 1.9.4. Trajectories were processed and analyzed using MDAnalysis 2.7.0. Feature selection was performed using MoSAIC 0.4.1. Principal Component Analysis was performed with Scikit-Learn 1.5.2. Metadynamics simulations were run using CVPack 0.12.2 and the PLUMED 2.9 plugin for OpenMM. Independent metadynamics simulations were combined using pyMFI package. Plots were generated in Python using Matplotlib 3.9.2 and Seaborn 0.13.2. Images were made using Adobe Illustrator (v26.1). A full description of software used in each study is provided in Supplementary Information. The scripts used to run and analyze the simulations in this study are part of an in-house software package currently under active development by the Forli Lab. Because the complete software suite remains unpublished and is undergoing final development, the specific code necessary to reproduce the reported results is available from the corresponding author upon reasonable request. Upon the official release of the software, the full package will be made publicly accessible through the Forli Lab GitHub repository at https://github.com/forlilab. All rest codes used in this study were adapted from prior published works. |

For manuscripts utilizing custom algorithms or software that are central to the research but not yet described in published literature, software must be made available to editors and reviewers. We strongly encourage code deposition in a community repository (e.g. GitHub). See the Nature Portfolio guidelines for submitting code & software for further information.

## Data

Policy information about availability of data

All manuscripts must include a data availability statement. This statement should provide the following information, where applicable:

- Accession codes, unique identifiers, or web links for publicly available datasets
- A description of any restrictions on data availability
- For clinical datasets or third party data, please ensure that the statement adheres to our policy

Experimental protein structures were batch downloaded from Protein Data Bank using Mac Terminal (v2.12.5 (444)) according to the PDB website (https://www.rcsb.org/docs/programmatic-access/batch-downloads-with-shell-script). Alpha Fold Structures and Uniprot information were downloaded directly from the web sites without additional software.

The Uniprot Homo sapiens proteome database (2018; 42,358 sequences) was used for proteomic searches. The sequence of K-Ras4A was obtained from UniProt (P01116). All data generated or analyzed during this study are available in the main text or the Supplementary Information. Uncropped, full western blot images and gels are provided in Source data and Supplementary Figures. Proteomics data behind all graphs in main Figures and Extended Data Figures are provided as separate Excel files and will be deposited to the PRIDE repository. The simulation input PDB models necessary to reproduce the results in this study have been deposited in the Zenodo public repository.

## Research involving human participants, their data, or biological material

Policy information about studies with human participants or human data. See also policy information about sex, gender (identity/presentation), and sexual orientation and race, ethnicity and racism.

| | |
|---|---|
| Reporting on sex and gender | N/A |
| Reporting on race, ethnicity, or other socially relevant groupings | N/A |
| Population characteristics | N/A |
| Recruitment | N/A |
| Ethics oversight | N/A |

Note that full information on the approval of the study protocol must also be provided in the manuscript.

# Field-specific reporting

Please select the one below that is the best fit for your research. If you are not sure, read the appropriate sections before making your selection.

☒ Life sciences ☐ Behavioural & social sciences ☐ Ecological, evolutionary & environmental sciences

For a reference copy of the document with all sections, see nature.com/documents/nr-reporting-summary-flat.pdf

# Life sciences study design

All studies must disclose on these points even when the disclosure is negative.

| | |
|---|---|
| Sample size | Numbers of sample size were chosen based on the maximum number of replicates that could be simultaneously analyzed with adequate statistics. |
| Data exclusions | Mass spectrometry data not meeting thresholds (intensity threshold, quantification purity, etc.) defined in the Methods section were excluded from analysis. No other data were excluded. |
| Replication | Numbers of replicates are described in the figure legends, where applicable. |
| Randomization | Each experiment included an equal number of replicates for both experimental and control conditions within each study. Data analysis was optimized for accurate comparison. For cell treatments, plates were randomly assigned to conditions. Randomization was not applicable to the design or synthesis of chemical probes. |
| Blinding | Investigators were not blinded to the group allocation during data collection or analysis to allow for processing of the data in a manner that allows for best comparison. Blinding is not applicable to the design and synthesis of chemical probes used in this study. |

# Reporting for specific materials, systems and methods

We require information from authors about some types of materials, experimental systems and methods used in many studies. Here, indicate whether each material, system or method listed is relevant to your study. If you are not sure if a list item applies to your research, read the appropriate section before selecting a response.

## Materials & experimental systems

| n/a | Involved in the study |
|---|---|
| ☐ | ☒ Antibodies |
| ☐ | ☒ Eukaryotic cell lines |
| ☒ | ☐ Palaeontology and archaeology |
| ☒ | ☐ Animals and other organisms |
| ☒ | ☐ Clinical data |
| ☒ | ☐ Dual use research of concern |
| ☒ | ☐ Plants |

## Methods

| n/a | Involved in the study |
|---|---|
| ☒ | ☐ ChIP-seq |
| ☒ | ☐ Flow cytometry |
| ☒ | ☐ MRI-based neuroimaging |

## Antibodies

Antibodies used

Anti-KRAS Polyclonal antibody (12063-1-AP), JAK1 Monoclonal antibody (3H7A8) (66466-1-Ig), ATP6V1E1 Polyclonal antibody (15280-1-AP), EDEM3 Polyclonal antibody (27310-1-AP), CDH2 Polyclonal antibody (22018-1-AP), NPC2 Polyclonal antibody (19888-1-AP), WWP2 Polyclonal antibody (12197-1-AP), MARCKS Polyclonal antibody (10004-2-Ig), CD44 Polyclonal antibody (15675-1-AP), CETN2 Polyclonal antibody (15877-1-AP), AS3MT Polyclonal antibody (27270-1-AP), DDOST Polyclonal antibody (14916-1-AP), HRP-Goat Anti-Rabbit IgG Conformation Specific Recombinant Secondary Antibody (RGAR301) were purchased from Proteintech. Anti-pERK Polyclonal antibody (#4370), ERK Polyclonal antibody (#9102), Phospho-Tyrosine (P-Tyr-1000) (#8954), Phospho-EphA2 (Tyr772) antibody (#8244), LAMTOR2/ROBLD3 (D7C10) Rabbit mAb (#8145), HA-Tag (C29F4) Rabbit mAb (#3724), Phospho-(Ser/Thr) Phe antibody (#9631), PARP1 Polyclonal antibody (#9541), CAPS3 Polyclonal antibody (9662), BiP Rabbit mAb (C50B12) (#3177), DR5 (E9D7D) Rabbit Monoclonal Antibody (69400), TIMP3 (D74B10) Rabbit Monoclonal Antibody (5673), SOS1 Antibody (5890) were from Cell Signaling Technology. Anti-mouse-HRP Goat polyclonal antibody (ab6789) and anti-rabbit-HRP Goat polyclonal antibody (ab6721) were purchased from Abcam. Anti-EPHA2 Polyclonal antibody (AF3035) was from R&D. Anti-monoclonal anti-Flag (M2) antibody (F3165) was from Sigma-Aldrich. Anti-LAMTOR1 Rabbit pAb (A21557) was from Abclonal. Anti-LAMP-1 Monoclonal (H4A3) antibody (328601), DyLight™ 488 Donkey anti-rabbit IgG (minimal x-reactivity) antibody (406404), Alexa Fluor® 647 anti-mouse IgG1 antibody (406617) were from Biolegend. Rhodamine labeled Actin (12004164) hFAB, rhodamine labeled Tublin (12004165) hFAB were obtained from Bio-Rad. Donkey Anti-Goat IgG, HRP (H+L) (705-035-003) was from Jackson ImmunoResearch Laboratories.

Validation

Antibodies were used solely for purposes that were validated by the manufacturer.

KRAS Polyclonal antibody (Reactivity: Human, Mouse, Rat; applications: WB, IHC, IF/ICC, FC (Intra), IP, ELISA) was validated by western blot analysis of HEK-293 cells, A549 cells, human brain tissue, human kidney tissue, mouse kidney tissue, rat kidney tissue, rat liver tissue, HeLa cells, mouse brain tissue, rat brain tissue from Proteintech Group, Inc..
https://www.ptglab.com/products/KRAS-Antibody-12063-1-AP.htm

JAK1 Monoclonal antibody (3H7A8) (Reactivity: Human, Mouse, Rat; applications: WB, IHC, IF, IP, ELISA) was validated by western blot analysis of K-562 cells, Jurkat cells, rat spleen tissue, PC-12 cells, NIH/3T3 cells, RAW 264.7 cells, Ramos cells, Daudi cells from Proteintech Group, Inc..
https://www.ptglab.com/products/JAK1-Antibody-66466-1-Ig.htm

ATP6V1E1 Polyclonal antibody (Reactivity: Human, Mouse, Rat; applications: WB, IHC, IP, ELISA) was validated by western blot

analysis of HeLa cells, human liver tissue, human brain tissue, mouse brain tissue, HEK-293 cells from Proteintech Group, Inc..
https://www.ptglab.com/products/ATP6V1E1-Antibody-15280-1-AP.htm

EDEM3 Polyclonal antibody (Reactivity: Human, Mouse; applications: WB, IHC, IF, IP, ELISA) was validated by western blot analysis of 3T3-L1 cells, HEK-293 cells from Proteintech Group, Inc..
https://www.ptglab.com/products/EDEM3-Antibody-27310-1-AP.htm

CDH2 Polyclonal antibody (Reactivity: Human, Mouse, rat; applications: WB, IHC, IF/ICC, IF-P, IF-Fro, IP, CoIP, ELISA) was validated by western blot analysis of HepG2 cells, HT-1080 cells, mouse lung tissue, mouse kidney tissue from Proteintech Group, Inc..
https://www.ptglab.com/products/N-cadherin-Antibody-22018-1-AP.htm

NPC2 Polyclonal antibody (Reactivity: Human, Mouse; applications: WB, IHC, IF, ELISA) was validated by western blot analysis of mouse brain tissue, A549 cells, C2C12 cells, HEK-293 cells, rat brain tissue, HepG2 cells, NCI-H1299 cells, HeLa cells, C6 cells, PC-3 cells, rat heart tissue from Proteintech Group, Inc..
https://www.ptglab.com/products/NPC2-Antibody-19888-1-AP.htm

WWP2 Polyclonal antibody (Reactivity: Human, Mouse, rat; applications: WB, IHC, IF, IP, CoIP, ELISA) was validated by western blot analysis of HepG2 cells, A549 cells from Proteintech Group, Inc..
https://www.ptglab.com/products/WWP2-Antibody-12197-1-AP.htm

MARCKS Polyclonal antibody (Reactivity: Human, Mouse, rat, bovine; applications: WB, IHC, IF, IP, ELISA) was validated by western blot analysis of mouse brain tissue from Proteintech Group, Inc..
https://www.ptglab.com/products/Marcks-Antibody-10004-2-Ig.htm

DDOST Polyclonal antibody (Reactivity: Human, Mouse, rat; applications: WB, IHC, IF, IP, CoIP, ELISA) was validated by western blot analysis of HeLa cells, A549 cells, mouse pancreas tissue, rat pancreas tissue from Proteintech Group, Inc..
https://www.ptglab.com/products/DDOST-Antibody-14916-1-AP.htm

pERK Polyclonal antibody (Reactivity: Human, Mouse, rat; applications: WB, IHC, IF, IP, F) was validated by western blot analysis of HeLa cells, NIH/3T3 cells, C6 cells, Jurkat cells from Cell Signaling Technology.
https://www.cellsignal.com/products/primary-antibodies/phospho-p44-42-mapk-erk1-2-thr202-tyr204-d13-14-4e-xp-rabbit-mab/4370

ERK Polyclonal antibody (Reactivity: Human, Mouse, rat; applications: WB, IP) was validated by western blot analysis of HeLa, NIH/3T3, C6, COS-7, CHO-K1, BAEC cells from Cell Signaling Technology.
https://www.cellsignal.com/products/primary-antibodies/p44-42-mapk-erk1-2-antibody/9102

Phospho-Tyrosine (P-Tyr-1000) MultiMab® Rabbit mAb (Reactivity: all; applications: WB, IP, IF, F) was validated by western blot analysis of A-431 cells from Cell Signaling Technology.
https://www.cellsignal.com/products/primary-antibodies/phospho-tyrosine-p-tyr-1000-multimab-rabbit-mab-mix/8954

Phospho-EphA2 (Tyr772) Antibody (Reactivity: Human, Mouse, rat; applications: WB, IP) was validated by western blot analysis of SNB19 cells from Cell Signaling Technology.
https://www.cellsignal.com/products/primary-antibodies/phospho-epha2-tyr772-antibody/8244

LAMTOR2/ROBLD3 (D7C10) Rabbit mAb (Reactivity: Human, Mouse, rat; applications: WB, IP) was validated by western blot analysis of HepG2, mIMCD-3, MCF7, LNCaP, KNRK, NBT-II, Raji, AR42J cells from Cell Signaling Technology.
https://www.cellsignal.com/products/primary-antibodies/lamtor2-robld3-d7c10-rabbit-mab/8145

HA-Tag (C29F4) Rabbit mAb (Reactivity: all; applications: WB, IHC, IF, IP, ChIP) was validated by western blot analysis of HA-tagged proteins in HeLa cells from Cell Signaling Technology.
https://www.cellsignal.com/products/primary-antibodies/ha-tag-c29f4-rabbit-mab/3724

Phospho-(Ser/Thr) Phe Antibody (Reactivity: all; applications: WB, IP) was validated by western blot analysis of A431 cells from Cell Signaling Technology.
https://www.cellsignal.com/products/primary-antibodies/phospho-ser-thr-phe-antibody/9631

Caspase-3 Antibody Rabbit pAb (Reactivity: Human; applications: WB, IP) was validated by western blot analysis of HCT116, NIH/3T3 and Jurkat lysates from Cell Signaling Technology.
https://www.cellsignal.com/products/primary-antibodies/caspase-3-antibody/9662

BiP (C50B12) Rabbit mAb (Reactivity: Human; applications: WB, IHC, F) was validated by western blot analysis of A204, L929 and U-87MG cells from Cell Signaling Technology.
https://www.cellsignal.com/products/primary-antibodies/bip-c50b12-rabbit-mab/3177

SOS1 Polyclonal Antibody Rabbit pAb #5890 (Reactivity: Human, Mouse; applications: WB, IP) was validated by western blot analysis of Raji, HCT116, BaF3 and 293 lysates from Cell Signaling Technology.
https://www.cellsignal.com/products/primary-antibodies/sos1-antibody/5890

DR5 (E9D7D) Rabbit Monoclonal Antibody (69400) (Reactivity: Human, applications: WB) was validated by western blot analysis of HT1080, HCT116, A-172, SNU-449, HepG2 and SNU-1 lysates from Cell Signaling Technology.
https://www.cellsignal.com/products/primary-antibodies/dr5-e9d7d-rabbit-monoclonal-antibody/69400

TIMP3 (D74B10) Rabbit Monoclonal Antibody (5673) (Reactivity: Human, Mouse, Rat; applications: WB) was validated by western blot analysis of A-431, NIH/3T3 lysates from Cell Signaling Technology.
https://www.cellsignal.com/products/primary-antibodies/timp3-d74b10-rabbit-monoclonal-antibody/5673

Human EphA2 Antibody (Reactivity: Human; applications: WB, F) was validated by western blot analysis of A431 cells from R&D systems. https://www.rndsystems.com/products/human-epha2-antibody_af3035

Monoclonal ANTI-FLAG® M2 antibody (Reactivity: all; applications: WB, IHC, IF, IP, CoIP, ELISA) was validated by Sigma-Aldrich. https://www.sigmaaldrich.com/US/en/product/sigma/f3165

LAMTOR1 Rabbit pAb (Reactivity: Human; applications: WB, IF) was validated by western blot analysis of B-cell, HeLa, Jurkat, U-87 MG, mouse brain from ABclonal.
https://www.abclonal.com/catalog-antibodies/LAMTOR1RabbitpAb/A21557

Anti-human CD107a (LAMP-1) Antibody (Reactivity: Human; applications: WB, FC, ICC, IHC-P) was validated by western blot analysis of NIH3T3, HeLa, human brain, mouse brain from Biolegend.
https://www.biolegend.com/fr-ch/products/purified-anti-human-cd107a-lamp-1-antibody-4964

DyLight™ 488 Donkey anti-rabbit IgG (minimal x-reactivity) Antibody (Reactivity: Human, Rabbit; applications: FC, ICC) was validated by Biolegend.
https://www.biolegend.com/fr-ch/products/dylight-488-donkey-anti-rabbit-igg-minimal-x-reactivity-5693

Alexa Fluor® 647 anti-mouse IgG1 Antibody (Reactivity: Human, Mouse; applications: FC, IHC) was validated by Biolegend.
https://www.biolegend.com/fr-ch/products/alexa-fluor-647-anti-mouse-igg1-9685

Rhodamine labeled anti-tubulin (Reactivity: Human, Mouse, Rat; applications: WB) was validated by western blot analysis of HeLa, HEK293T, and K562 lysates from Bio-Rad Laboratories, Inc..
https://www.bio-rad.com/en-us/sku/12004165-hfab-rhodamine-anti-tubulin-primary-antibody-200-ul?ID=12004165

Rhodamine labeled anti-actin (Reactivity: Human, Mouse, Rat; applications: WB) was validated by western blot analysis from Bio-Rad Laboratories, Inc.
https://www.bio-rad.com/en-us/sku/12004163-hfab-rhodamine-anti-actin-primary-antibody-200-ul?ID=12004163

Anti-rabbit-HRP Goat pAb (application: WB, IHC) was validated by Abcam.
https://www.abcam.com/en-us/products/secondary-antibodies/goat-rabbit-igg-h-l-hrp-ab6721

Anti-mouse-HRP Goat pAb (application: WB, IHC) was validated by Abcam.
https://www.abcam.com/en-us/products/secondary-antibodies/goat-mouse-igg-h-l-hrp-ab6789

Donkey Anti-Goat IgG (H+L) (application: WB, IHC, ELISA) was validated by Jackson ImmunoResearch Laboratories, Inc.
https://www.jacksonimmuno.com/catalog/products/705-035-003

HRP-Goat Anti-Rabbit IgG Conformation Specific Recombinant Secondary Antibody RGAR301 was validated by ProteinTech.
https://www.ptglab.com/products/HRP-Goat-Anti-Rabbit-IgG-Conformation-Specific-Recombinant-Secondary-Antibody-RGAR301.htm

## Eukaryotic cell lines

Policy information about cell lines and Sex and Gender in Research

| | |
|---|---|
| Cell line source(s) | MDA-MB-231, HEK293T, H460, MIA PaCa2 and H1975 cell lines were procured from ATCC, HCC44 cells were obtained from DSMZ, and Lenti-X 293T (LX293T) cells from Takara Bio. |
| Authentication | MDA-MB-231, HEK293T, H460, MIA PaCa2 and H1975 were authenticated by STR analysis by ATCC. HCC44 cells were authenticated by STR analysis by DSMZ. Lenti-X 293T cells were were authenticated by STR analysis by Takara bio. |
| Mycoplasma contamination | All cells used were tested negative for mycoplasma. |
| Commonly misidentified lines (See ICLAC register) | N/A |

## Plants

| | |
|---|---|
| Seed stocks | N/A |
| Novel plant genotypes | N/A |
| Authentication | N/A |